博士論文

Development of water electrolysis systems

at near-neutral pH

using concentrated phosphate solutions

（中性 pH 濃厚リン酸電解質溶液を用いた

水電解システムの開発）

内藤　剛大

Acknowledgement

First and foremost, I would like to express my most profound appreciation to Professor Kazuhiro Takanabe. He generously dedicated his time supervising me. I learned a wide range of knowledge about research from him. He taught me the global standard of science and how to conduct research on that standard. All the guidance and counsel he provided me brightened my future as a researcher.

I acknowledge Dr. Tatsuya Shinagawa deeply. He taught me the methods of scientific research in detail. His door was always open for a discussion and gave me valuable advice. I would not have been able to continue my research work without his support.

Also, I am grateful for the scientific discussion with my committee members; Professor Masaru Ogura, Professor Ryuji Kikuchi, Professor Toru Wakihara, and Professor Yuki Yamada kindly spent their valuable time with me. Their professional comments deepened the discussion of this dissertation. My deep appreciation also goes to the staff member and colleagues of Takanabe laboratory, Professor Masao Katayama, Dr. Tomohiro Higashi, Dr. Fuminao Kishimoto, Dr. Keisuke Obata, Dr. Bhavin Siritanaratkul, Dr. Xiaofei Lu, Dr. Duanxing Li, Movick William James, Takeshi Nishimoto, Xingyu Qi, Melody Wada, and Hiroki Komiya. Particularly, Takeshi Nishimoto took time frequently for discussions, which deepened my knowledge of electrocatalysis. In addition, I am also grateful to the great lab members at Takanabe lab and all my friends. Their support provided me with fruitful days during my PhD course.

<div align="right">

Takahiro Naito

January, 2022

</div>

Abstract

The transition to a future sustainable society will be achieved if issues associated with renewable energy, such as low energy density and spatiotemporal fluctuation, are overcome. The electrocatalytic systems are compatible with this view because renewable electricity can be converted to chemical products, and specific chemical products can be used as clean energy carriers. Among a variety of energy carriers, hydrogen stands out owing to its high weight energy density. However, industrialized water electrolyzers produce hydrogen only at a cost inferior to those based on fossil fuels. Given the recent decrement in the price of renewable electricity, a decrease in the capital cost of the water electrolyzers would further facilitate the utilization of hydrogen. The prevalent water electrolyzer is mature, and a new viewpoint to develop the electrolyzer would be effective for cost reduction. In this context, near-neutral pH water electrolysis is now gathering attention because its milder environment than the extremely acidic or alkaline pH of the existing electrolyzers can offer cost reduction owing to wide options for materials. However, the lower efficiency of the near-neutral pH electrolysis than the conventional water electrolyzers hampers the utilization in industry, requiring research effort to improve the efficiency. In this dissertation, firstly, a quantitative analysis determined mass-transport fluxes and associated losses, which is considered as a significant problem of near-neutral pH water electrolysis during water electrolysis. The analysis identified electrolyte that minimizes the mass-transport losses at pH 7, i.e., saturated K-phosphate solution. Then, water electrolysis in the determined solutions was examined using IrO_x anode and Pt cathode as model electrodes at elevated temperatures, demonstrating the comparable performance of the electrolysis to the existing electrolyzers with room for further study on the gas separation. Subsequently, a gas separator, which is a significant factor to determine the efficiency of water electrolysis, using for near-neutral pH was investigated. The electrolyte engineering approach could suppress the cross-over of gaseous molecules by regulating their diffusion flux. In addition, hydrophilized mechanically stable glass sheet was found to suppress the permeation of gas bubbles, while its high porosity and small thickness concurrently kept the resistance low. The demonstration of water electrolysis in the thus developed system revealed the performance is comparable to conventional water electrolyzer, exhibiting the potential of the near-neutral pH water electrolysis as a next-generation water electrolyzer.

Table of contents

List of abbreviations

AWE   alkaline water electrolyzer

CEM   cation exchange membrane

CHE   computational hydrogen electrode

CP   Chronopotentiometry

CPET   concerted proton-electron transfer

CV   cyclic voltammogram

ET   electron transfer

FE   Faradaic efficiency

HER   hydrogen evolution reaction

HOR   hydrogen oxidation reaction

IEP   the isoelectric point

LSV   linear sweep voltammogram

OER   oxygen evolution reaction

ORR   oxygen reduction reaction

pds   potential-determining step

PEM   polymer electrolyte membrane

PEMWE   polymer electrolyte membrane water electrolyzer

PT   proton transfer

RDE   rotating disk electrode

RDS   rate determining step

RHE   reversible hydrogen electrode

SCE   saturated calomel electrode

SHE   standard hydrogen electrode

List of symbols

Symbol	Unit	Definition
A	cm^{-2}	electrode surface area
c	$mol\,L^{-1}$	concentration
D_i	$cm^2\,s^{-1}$	diffusion coefficient of species i
d	nm	effective ion diameter
E	V	electrode potential
E_a	$kJ\,mol^{-1}$	activation energy
ε		porosity
V_{eq}	V	equilibrium potential
e	C	elementary charge
F	$C\,mol^{-1}$	Faraday's constant
j	$mA\,cm^{-2}$	current density
i_{lim}	$mA\,cm^{-2}$	diffusion-limited current density
K_{cell}	cm	cell constant
k	$m^2\,kg\,s^{-2}\,K^{-1}$	Boltzmann constant
n		number of electron
ρ	$\Omega\,m$	resistivity
R	$J\,mol^{-1}\,K^{-1}$	gas constant
T	K	absolute temperature
V	V	voltage
z		number of charge
δx	mm	diffusion layer thickness
η	V	overpotential
μ	Pa s	viscosity
ω	s^{-1}	electrode rotation speed
v	$mm^2\,s^{-1}$	kinematic viscosity
ω	$rad\,s^{-1}$	angular rotation rate

List of figures

List of tables

1. Introduction

1.1. Perspective of world energy demand and implementation of renewable energy

The world energy demand has increased with economic growth and reached 55×10^8 EJ year^{-1} in 2015 as shown in **Figure 1.1**.[1] The energy demand has remained unchanged recently in OECD countries because the economic and population growth remain low. Nevertheless, the world energy demand will continuously increase mainly due to the economic and population growths of developing countries, and the future demand in 2050 is predicted to be almost twice that in 2015.[2] Currently, as shown in **Figure 1.1**, 83% of the demand is satisfied by fossil fuel-based energy; oil 32%, natural gas 23%, coal 28%. However, this type of energy would not satisfy the future demand due to the limitation of reserves of fossil fuel. In this context, renewable energy stands as a promising energy source because 60 times larger energy than the demand is reached from the Sun, the representative energy source, to the Earth.[3] Nevertheless, the low energy density and spatiotemporal fluctuation of renewable energy have hampered its widespread use, with only 13% of energy demand in 2015 being met by renewable energy (**Figure 1.1**). Therefore, efficient utilization of this huge amount of energy is a key to achieving the implementation of renewable energy and the resulting future sustainable society.
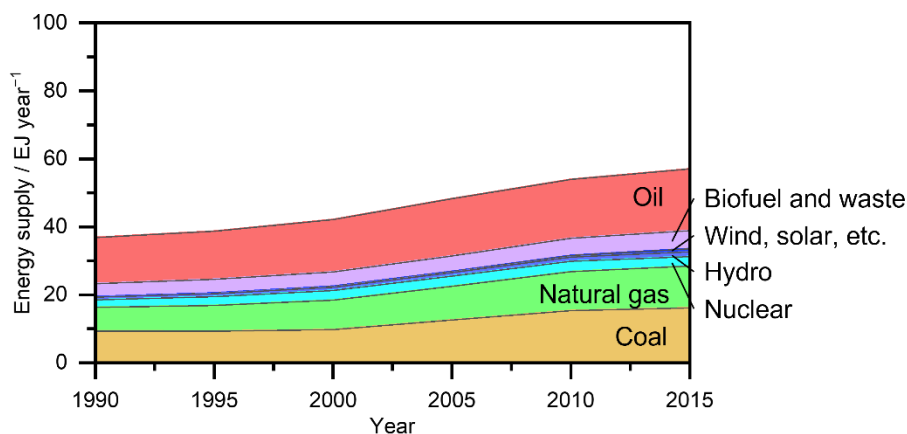
Figure 1.1. World energy supply. The data adopted from reference [1].

Several technologies are considered to solve the issues of renewable energy such as the low energy density and the fluctuation by storing and utilizing the renewably generated electricity. The electricity generated from renewable energy can be stored in the form of chemical energy, mechanical energy, potential energy, and electricity itself. Particularly, among them, hydrogen is often considered as a promising energy carrier, which can solve the issues associated with renewable energy, because of its largest energy density.[4] The hydrogen can be produced by water electrolysis using renewably obtained electricity. The obtained hydrogen is stored and used as a fuel in fuel cells to obtain electricity on demand.[5] Additionally, hydrogen can be converted to other chemical products such as ammonia, synthesis gas, methanol, and so on, depending on the objectives.[6,7] Therefore, hydrogen can play a significant role in a future sustainable society.

1.2.   Conventional water electrolysis

Water electrolysis is often considered a mature technology because the technology has developed since it was first reported in 1789 by Paets van Troostwijik and Deiman.[8] Then, this subsection summarizes the current situation of water electrolysis.

1.2.1.   Water electrolyzers

Prevailing conventional water electrolyzers are the alkaline water electrolyzer (AWE) and polymer electrolyte membrane (PEM) water electrolyzer (PEMWE), which operates at relatively low temperatures (< 120 °C) and has a high affinity to renewable energy. The typical operating conditions are listed in **Table 1.1**. The significant difference between the two electrolyzers is the pH levels of electrolytes. AWE adopts alkaline conditions, i.e., ca. 30 wt% KOH solutions, while PEMWE does acidic conditions, i.e., perflurosulfonated acid (PFSA), causing differences of the electrolyzers such as reaction mechanism and the applicability of materials for the electrolyzers.

Table 1.1. Typical characteristics of electrolyzers. The data were adapted from reference [9-13].

	AWE	PEMWE
Typical electrolyte	20-40 wt% KOH	PFSA*
Typical anode catalyst	NiO_x	IrO_x
Typical cathode catalyst	Ni	Pt
Operating temperature / °C	60-80	50-80
Cell pressure / bar	< 30	30-76
Current density / A cm^{-2}	< 0.45	> 1.6
Cell Voltage / V	1.8-2.4	1.8-2.2
Voltage efficiency (HHV) / %	62-82	67-82
Cell area / m^2	3-3.6	< 0.13
Stack lifetime / kh	55-120	60-100
System lifetime / year	20-30	10-20
Hydrogen purity / %	> 99.8	99.9999
Capital cost / € kW^{-1}	1000-1200	1860-2320

*PFSA: perflurosulfonated acid

For the reaction mechanism, the most significant difference between the conditions is reactants during water electrolysis. Under acidic conditions, H$^+$ and H$_2$O are the reactant for the following half-reactions of hydrogen evolution reaction (HER) and oxygen evolution reaction (OER), respectively:[14]

Under acidic conditions:

$$HER: \ 2H^+ + 2e^- \rightleftharpoons H_2 , \qquad (1\text{-}1)$$
$$OER: \ 2H_2O \rightleftharpoons O_2 + 4H^+ + 4e^- . \qquad (1\text{-}2)$$
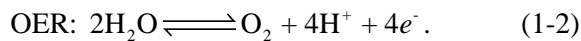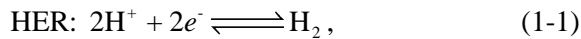
On the other hand, under alkaline conditions, H$_2$O and OH$^-$ are the reactant for the following half-reactions of HER and OER, respectively:[14]

Under alkaline conditions:

$$HER: \ 2H_2O + 2e^- \rightleftharpoons H_2 + 2OH^- , \qquad (1\text{-}3)$$
$$OER: \ 4OH^- \rightleftharpoons O_2 + 2H_2O + 4e^- . \qquad (1\text{-}4)$$
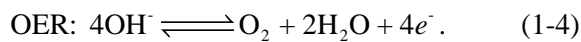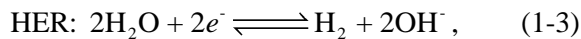
Regarding applicable materials to the electrolyzer components, elements that can be used for catalysts of water electrolysis depend on the pH levels of the electrolyte. Generally, transition metals

from group 7 to 10 of the periodic table are considered suitable metals[15-17] due to the d-band character.[18,19] Under alkaline conditions, earth-abundant and cost-effective metals such as Fe and Ni can be used as a component of active catalysts for the water electrolysis,[20] while the acidic condition is forced to use expensive noble metals such as Ir[20] and Pt[20] as the catalyst due to the low stability of the aforementioned metals under acidic conditions.[21] The same thing can be said to other components of the electrolyzers, resulting in the almost twice higher capital cost of PEMWE than AWEs as in **Table 1.1**. The breakdowns for stack costs are shown in **Figure 1.2** to review the detail of the capital cost of the electrolyzers. In the case of **Figure 1.2a**, the cost breakdown shows that electrodes occupy more than half of the cost, while a membrane, a structural ring, and a bipolar plate each account for around 7-14%. In PEMWE, the fewer options for material than the AWE increases the cost, e.g., expensive Ti, which has corrosion tolerance under the extremely acidic conditions, are used in bipolar plate.[22] Another feature of the cost is MEA manufacturing due to the configuration of PEMWE, and the others are similar to alkaline ones. Among these components, gas separators (denotes as "Membrane" in **Figure 1.2**), which contain electrolyte, and electrocatalysts (denotes as "Anode" and "Cathode" in **Figure 1.2**) are the most fundamental components to determine the efficiency of water electrolysis and will be discussed in the following subsections.
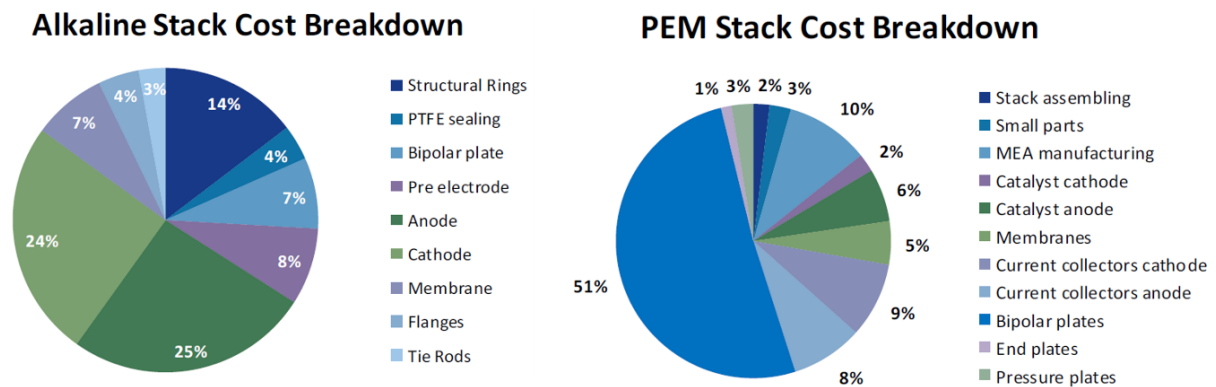
Figure 1.2. Stack cost breakdown for (a) AWE and (b) PEMWE.[23]

1.2.2. Gas separators and electrolytes

In the water electrolyzers, gas separators are essential to produce pure hydrogen and oxygen during the electrolysis. In addition, the resistivity of the separators determines *iR* losses during water electrolysis, which significantly affects the efficiency of water electrolysis. Two types of gas-separators are used now, i.e., PEM and diaphragms. In PEM, ionizable functional groups take up

water and transport protons or hydroxide ions, resulting in sufficient ionic conductivity just with deionized water. In contrast, a diaphragm, a porous medium, needs aqueous electrolyte solution to provide ionic conductivity between the electrodes.[24]

Among the various PEM and diaphragm, the Nafion is used in PEMWE as the most prevailing PEM, while the Zirfon Perl UTP 500 is the most prevalent diaphragm used in AWE.[25,26] The Nafion is a cation exchange membrane (CEM) which exchange protons. Although the Nafion can work with deionized water, sulfonic acid in the Nafion causes an extremely acidic environment. On the other hand, the Zirfon consists of submicron pores to circumvent the crossover of evolved H_2 and O_2. The submicron pores allow electrolyte solutions, i.e., concentrated KOH solutions, to penetrate the diaphragm. Thus, the performance of the AWE such as gas separation and resistivity can depend on electrolyte properties.

For the gas separation, crossover occurs when the dissolved gases or gas bubbles pass through the gas separator, which should be prevented to obtain pure H_2 and O_2. In the case of the dissolved gases, a concentration gradient of evolved gases drives diffusion, leading to the crossover.[27] The diffusion flux is determined by electrolyte properties such as concentrations, temperatures, and viscosities. For the gas bubbles, briefly, smaller pore size and higher hydrophilicity of the separators allows less permeation of the gases (see detailed discussion described in **Chapter 4**). This consideration suggests that investigation of the electrolyte properties and the gas separator properties would play a significant role in the efficiency of the gas separation.
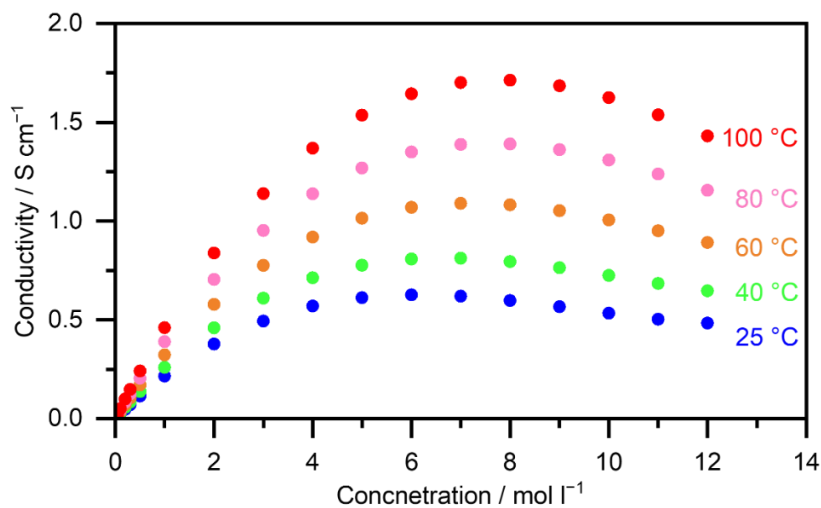
Figure 1.3. Conductivity of KOH solutions as a function of concentration with various temperatures.[30]

Among the properties of electrolytes used in AWE, resistivity, whose reciprocal is conductivity, is a key factor for the efficiency, particularly as *iR* losses, of water electrolysis. *iR* loss during water electrolysis is expressed in the following equation:[29]

$$R = \frac{1}{\sigma} \times \frac{l}{A} = \frac{K_{cell}}{\sigma},$$
(1-5)

in which σ is the solution conductivity, *l* and *A* are the specific length and cross-sectional area of the electrochemical cell, respectively,[29] and *l/A* is called the cell constant K_{cell}. Higher ionic conductivity leads to low *iR* loss during water electrolysis. Hence, the conductivity of the electrolyte solution plays a significant role in *iR* loss. In line with this objective, KOH solutions, which are used as a representative aqueous electrolyte solution for AWE, adopt a condition of 30 wt% at around 80 °C. **Figure 1.3** shows the conductivity of KOH solutions as a function of solution concentration at various temperatures.[28] For all temperatures, the conductivity increases with concentration until interactions between the ions by coulombic force become significant to reduce the conductivity,[30] resulting in the volcano-like shape. Although the conductivity increases with elevating temperatures, the general electrolyzers adopt ca. 80 °C, whose conductivity is ca. 1.4 S cm^{-1}, to prioritize easy handling such as avoidance of electrolyte evaporation and longevity of the equipment.[31]

With a diaphragm-type gas separator, the resistivity increases from that of the electrolyte solutions due to its non-conductive nature. The resistivity of a diaphragm-type gas separator is expressed as following empirical law;[32-34]

$$\rho = \rho_0 \frac{1}{\varepsilon^{1.5}},$$
(1-6)

in which, ρ_0 is the resistivity of the solution, and ε is the porosity of the gas separator. This equation suggests that the higher porosity of the gas separator and lower resistivity of the electrolyte solutions reduce the *iR* loss during water electrolysis. Particularly, regarding the porosity, a porosity of the Zirfon at 55%[35] will increase the resistivity by more than double. In this context, investigating gas separators that have higher porosity than the Zirfon could further reduce the *iR* loss (see detailed discussion for **Chapter 4**).

1.2.3. Electrocatalysts

HER and OER catalysts have been developed over a long period of time to reduce the overpotentials. In the case of HER, in 1935, Horiuti and Polanyi first reported the rationale about the HER kinetics based on the chemisorption energy of the H intermediate against the nature of the electrode metal.[36] After that, in 1977, Trasatti summarized a relationship between log (exchange

current density) and M-H (M denotes a metal) bonding energy, exhibiting a volcano trend as shown in **Figure 1.4a**.[37] This trend suggests that there exists an optimal M-H binding energy to minimize the overpotential for the HER. In **Figure 1.4a**, Pt sits at the top of the volcano, and this element is now known as one of the most active HER catalysts.[20] Currently, to develop active yet cost-effective electrocatalysts, several electrodes composed of earth-abundant elements have been reported, such as NiMo.[20]

Similar to HER catalysts, OER catalysts developed with rationale. The volcano plot for OER was also constructed based on the descriptor of M-OH as shown in **Figure 1.4b**.[38] IrO_x and RuO_x sit at the top of the volcano, and were reported as highly active OER catalysts.[20] Those catalysts are composed of novel metals, and tremendous research efforts were dedicated to developing OER catalysts made of earth-abundant elements such as $NiFeO_x$.[20] A detailed description of OER catalysts can be found in **Chapter 2**.
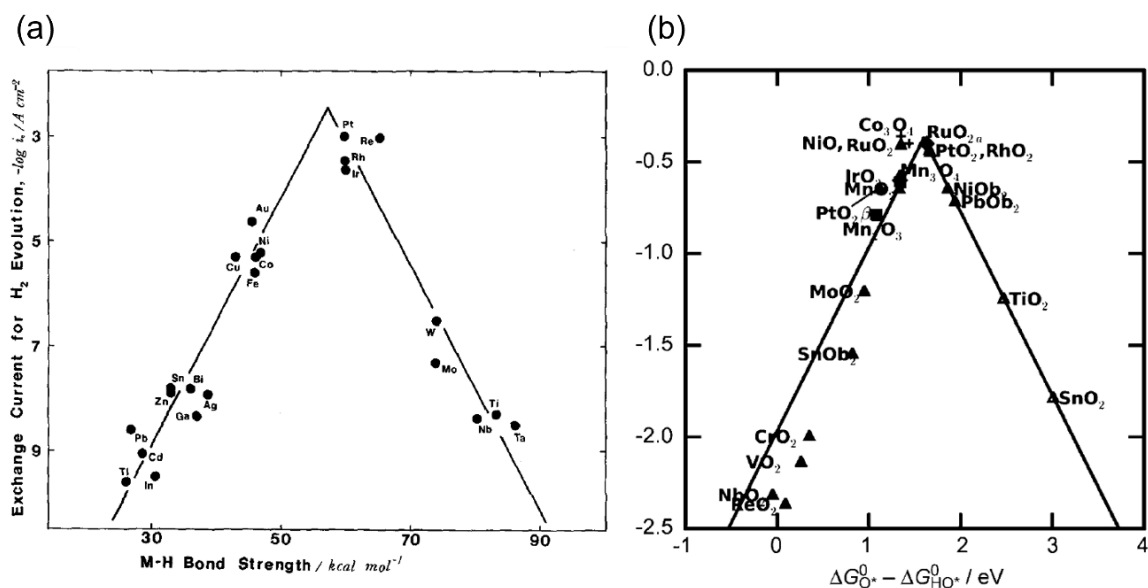
Figure 1.4. Volcano-shaped plots of the catalytic performance as a function of (a)M-H bonding for hydrogen evolution reaction (HER) catalysts,[37] (b) M-OH bonding for oxygen evolution reaction (OER) catalysts.[38]

Notably, the discussion of the catalytic activity of these electrocatalysts has not taken into account the actual environment of the catalyst, such as the electronic structure of the active sites. Furthermore, the reaction mechanism can be different depending on the active site. Therefore, there might exist

cost-effective and highly active catalysts that are off the top of the conventional volcano plot by changing the environment of the active site such as the particle size and pH of the electrolyte.

All in all, detailed reviewing regarding conventional water electrolysis in this subsection showed a possibility of the capital cost reduction even for the AWE, whose capital cost is lower than that of the PEMWE. Particularly, investigation on the electrolyte properties, the gas separator properties, and the environment of the active site would be the key to reducing the cost.

1.3.   Near-neutral pH water electrolysis

As discussed in **Section 1.2**, the technology of the prevalent water electrolyzer is mature, and a new viewpoint to develop the electrolyzer would be effective for the cost reduction. Near-neutral pH water electrolysis is one option because its milder environment than the extremely acidic or alkaline pH of the existing electrolyzers can widen the choice of materials for electrolyzer components and reduce the capital cost of an electrolyzer.

Despite such an advantage of near-neutral pH, the condition has never been industrialized because of the low efficiency due in part to the slow kinetics of both HER[39,40] and OER[41]. More specifically, under unbuffered near-neutral pH conditions, both HER and OER experience two-step cathodic or anodic events originating from the change of reactant, as expressed in **Equation 1-1 to 1-4**, due to diffusion limitation of the ionic reactants. These reactant changes caused kinetic difficulty, i.e., for OER, dissociating the O-H bonding of H_2O could require larger overpotential H_2O oxidation than OH^- oxidation,[42] and the similar can be said for HER.

Electrolyte properties are a critical factor that governs the efficiency at near-neutral pH levels. The improvement of the electrocatalytic performance was observed by introducing buffering substances into electrolytes at near-neutral pH.[43,44] One of the reasons for the improvement is explicated by the prevention of local pH shifts near the surface of the electrode by buffering action.[14,45,46,47]

$$HA \rightleftharpoons H^+ + A^-, \qquad (1\text{-}7)$$
$$HA + OH^- \rightleftharpoons A^- + H_2O, \qquad (1\text{-}8)$$
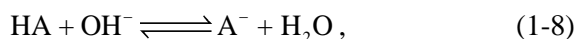
in which A^- denotes the buffering substance such as $H_xPO_4^{x-3}$ or $H_yCO_3^{y-2}$. In addition to this buffering action, previous study presented another significant role of buffering substances that the buffering substances directly participate the reactions,[48] e.g., direct reduction of proton-containing species during HER as following expression;[48]

$$2HA + 2e^- \rightleftharpoons H_2 + 2A^-. \qquad (1\text{-}9)$$
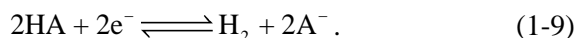
Another key factor for the efficiency of near-neutral pH water electrolysis is the mass transport during the electrolysis. A previous study suggested that the electrocatalytic HER rate was majorly determined by the mass transport of the buffer substance functioning as a proton carrier.[46] Another study reported that optimization of electrolyte properties enlarged the mass-transport flux of the buffer substance and improved electrocatalytic performance (electrolyte engineering).[14] This direction of study would improve the efficiency of water electrolysis at near-neutral pH and exhibit the potential of near-neutral pH electrolysis for the cost reduction. The detailed discussion on the optimization of electrolyte properties focusing on improvement of mass transport in buffered solutions at near-neutral pH can be found in **Chapter 3**.

In order to set a target for the development of near-neutral pH water electrolysis, the current status of the electrolysis needs to be clarified. **Figure 1.5** compares reported performances of industrialized alkaline water electrolyzers and near-neutral pH water electrolysis.[49-59] The critical difference between the two technologies lies in the current and temperature range. Current range for alkaline water electrolyzers is more than 100 mA cm^{-2}, whereas that for near-neutral pH water electrolysis is only 10 mA cm^{-2}. Moreover, a cell voltage of 1.69V is required to reach 10 mA cm^{-2} for a near-neutral one[49], while only 1.51 V is required to reach 100 mA cm^{-2} for an alkaline one.[54] As for the temperature range, alkaline water electrolyzers are operated at 60-80 °C, while near-neutral pH water electrolysis adopts ambient temperatures. In general, temperature significantly influences both the thermodynamics and kinetics of water electrolysis. Therefore, in order to evaluate the potential of near-neutral pH water electrolysis, research efforts at higher current density (> 100 mA cm^{-2}) and elevated temperatures (> 60 °C) are essential.
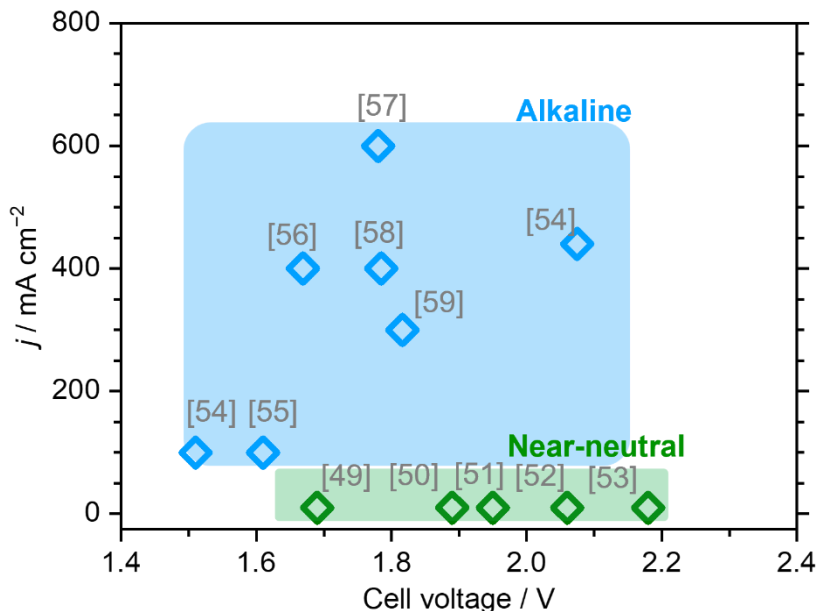
Figure 1.5. Performance comparison of industrialized alkaline water electrolyzer and near-neutral pH water electrolysis.[49-59]

1.4.   Scope of the dissertation

The development of near-neutral pH water electrolysis can be a key to producing cost-effective hydrogen from the electricity generated by renewable energy, leading to the realization of a future sustainable society. Here, this dissertation addresses the fundamental investigation aiming at constructing next-generation water electrolysis at near-neutral pH. The structure of the dissertation is depicted in **Figure 1.6**.

Chapter 2 introduces the mechanistic understanding of highly active OER catalysts, IrOx, as a model OER catalyst. The disclosed descriptions of theoretical kinetics are accordingly referred to in other chapters.

In **Chapter 3**, quantitative analysis of the mass transport flux during water electrolysis was conducted by measuring properties of various phosphate buffer solutions at pH 7.0, and conditions to accelerate the mass transport flux the most were determined to improve the efficiency of water electrolysis. Subsequently, water electrolysis using the determined solutions was performed. The determined condition of the electrolyte was utilized in the following study described in **chapter 4**.

Finally, in **Chapter 4**, a fundamental concept for near-neutral pH was presented on the basis of knowledge obtained in the other chapters. Gas crossovers as dissolve gases and gas bubbles during water electrolysis were investigated. For the crossover of dissolved gases, *electrolyte engineering* approach, which was utilized in **Chapter 3**, was also adopted to regulate the crossover. Then, the crossover of gas bubbles was investigated by using a glass sheet as a gas separator to physically prevent the crossover of the bubbles. Lastly, fundamental cell design utilizing the knowledge obtained in this dissertation was conducted, and water electrolysis using the cell was demonstrated to verify the feasibility of the system.
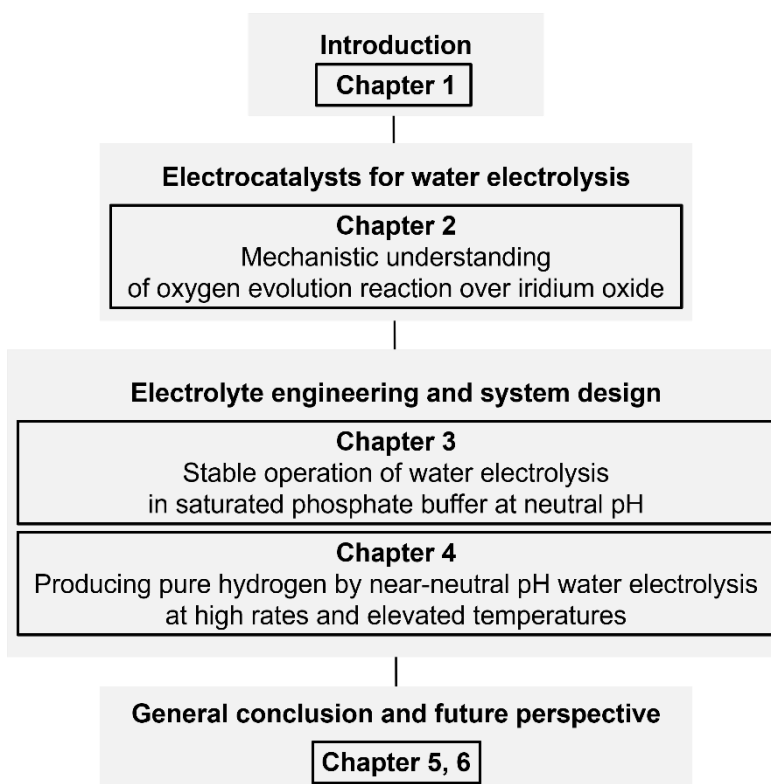
Figure 1.6. Structure of the dissertation

1.5.   References

[1] IEA, *World Energy Balances 2020*, https://www.iea.org/data-and-statistics (2021-10-24)

[2] U.S. Energy Information Administration, *International Energy Outlook 2019*

https://www.eia.gov/outlooks/ieo/ (2021-10-24)

[3] United Nations Development Programme and World Energy Council, *Energy and the challenge of sustainability*, **2000**.

[4] S. Satyapal, J. Petrovic, C. Read, G. Thomas, G. Ordaz, *Catal. Today* **2007**, *120*, 246-256.

[5] S. E. Hosseini, M. A. Wahid, *Int. J. Energy Res.* **2020**, *44*, 4110-4131.

[6] C. Graves, S. D. Ebbesen, M. Mogensen, K. S. Lackner, *Renewable Sustainable Energy Rev.* **2011**, *15*, 1-23.

[7] J. D. Holladay, J. Hu, D. L. King, Y. Wang, *Catal. Today* **2009**, *139*, 244-260

[8] R. de Levie, *J. Electroanal. Chem.* **1999**, *476*, 92-93.

[9] F. M. Sapountzi, J. M. Gracia, C. J. Kees-Jan Weststrate, H. O. A. Fredriksson, J. W. Hans Niemantsverdriey, *Prog. Energy Combust. Sci.* **2017**, *58*, 1-35.

[10] M. F. Lagadec, A. Grimaud, *Nat. Mater.* **2020**, *19*, 1140-1150.

[11] O. Schmidt, A. Gambhir, I. Staffell, A. Hawkes, J. Nelson, S. Few, *Int. J. Hydrogen Energy* **2017**, *42*, 30470-30492.

[12] M. Davida, C. Ocampo-Martínezc, R. Sánchez-Peña, *J. Energy Storage* **2019**, *23*, 392-403.

[13] I. Vincent, D. Bessarabov, *Renew. Sustain. Energy. Rev.* **2018**, *81*, 1690-1704.

[14] T. Shinagawa, K. Takanabe, *ChemSusChem* **2017**, *10*, 1318-1336.

[15] M. M. Jaksic, *J. New Mater. Electrochem. Syst.* **2000**, *3*, 153-168.

[16] J. Greeley, T. F. Jaramillo, J. Bonde, I. B Chorkendorff, J. K. Nørskov, *Nat. Mater.* **2006**, *5*, 909-913.

[17] E. Fabbri, A. Habereder, K. Waltar, R. Kötz, T. J. Schmidt, *Catal. Sci. Technol.* **2014**, *4*, 3800-3821.

[18] B. E. Conway, J. O. M. Bockris, *Nature* **1956**, *178*, 488-489.

[19] B. Hammer, J. K. Nørskov, *Adv. Catal.* **2000**, *45*, 71-129.

[20] C. C. L. McCrory, S. Jung, I. M. Ferrer, S. M. Chatman, J. C. Peters, T. F. Jaramillo, *J. Am. Chem. Soc*. **2015,** *137*, 4347-4357.

[21] M. Schalenbach, G. Tjarks, M. Carmo, W. Lueke, M. Mueller, and D. Stolten, *J. Electrochem. Soc*. **2016**, *163*, F3197-F3208.

[22] H. Wakayama, K. Yamazaki, *ACS Omega* **2021**, *6*, 4161-4166

[23] L. Bartuccioli, A. Chan, D. Hart, F. Lehner, B. Madden, E. Standen, "*Development of water electrolysis in the European Union*", Fuel Cells and Hydrogen Joint Undertaking, **2014**.

[24] M. Schalenbach, A. R. Zeradjanin, O. Kasian, S. Cherevko, K. J. J. Mayrhofer, *Int. J. Electrochem. Sci.* **2018**, *13*, 1173-1226.

[25] R. E. White, J. O'M. Bockris, B. E. Conway, *Modern Aspects of Electrochemistry No. 15*, Prenum Press, New York, **1983**

[26] J. Rodríguez, S. Palmas, M. S.-Molina, E. Amores, L. Mais, R. Campana, *Membranes* **2019**, *9*, 129.

[27] P. Atkins, J. D. Paula, *Atkins' Physical Chemistry, eighth ed.*, W. H. Freeman and Company, New York, **2006**.

[28] R. Gilliam, J. Graydon, D. Kirk, S. Thorpe, *Int. J. Hydrogen Energy*, **2007**, *32*, 359-364.

[29] D. Feakins, W. E. Waghorne, K. G. Lawrence, *J. Chem. Soc., Faraday Trans. 1* **1986**, *82*, 563-568.

[30] R. F. Mann, J. C. Amphlett, B. A. Peppley, C. P. Thurgood, *J. Power Sources* **2006**, *161*, 775.

[31] K Kinoshita, *Electrochemical oxygen technology, 1st ed.*, John Wiley & Sons, New York, **1992**.

[32] M. J. Martínez, S. Shimpalee, J. W. Van Zee, *J. Electrochem. Soc.* **2009**, *156*, B80-B85.

[33] B. Tjaden, S. J. Cooper, D. J. Brett, D. Kramer, P. R. Shearing, *Curr. Opin. Chem. Eng.* **2016**, *12*, 44-51,

[34] M. T. de Groot, A. W. Vreman, *Electrochim. Acta* **2021**, *369*, 137684.

[35] Technical Data Sheet ZIRFON PERL UTP 500 Separator membrane for alkaline electrolysis, GF-16, **2020**.

[36] J. Horiuti, M. Polanyi, *Acta Physicochim. URSS* **1935**, *2*, 505.

[37] S. Trasatti, *J. Electroanal. Chem.* **1977**, *39*, 163-184.

[38] S. Trasatti, *J. Electroanal. Chem.* **1980**, *111*, 125-131.

[39] D. Strmcnik, M. Uchimura, C. Wang, R. Subbaraman, N. Danilovic, D. van der Vliet, A. P. Paulikas, V. R. Stamenkovic, N. M. Markovic, *Nat. Chem.* **2013**, *5*, 300-306.

[40] T. Shinagawa, A. T. Garcia-Esparza, K. Takanabe, *ChemElectroChem* **2014**, *1*, 1497-1507.

[41] T. Takashima, K. Ishikawa, H. Irie, *ACS Catal.* **2019**, *9*, 9212-9215.

[42] B. E. Conway, B. V. Tilak, *Advances in Catalysis, Vol. 38* (Eds.: D. D. Eley, H. Pines, P. B. Weisz), Academic Press, New York, **1992**, pp. 78-98.

[43] W. Sheng, Z. Zhuang, M. Gao, J. Zheng, G. Chen, Y. Yan, *Nat. Commun.* **2015**, *6*, 5848.

[44] T. Shinagawa, M. T-K. Ng, K. Takanabe, *ChemSusChem* **2017**, *10*, 4155-4162.

[45] I. Katsounaros, J. C. Meier, S. O. Klemm, A. A. Topalov, P. U. Biedermann, M. Auinger, K. J. J. Mayrhofer, *Electrochem. Commun.* **2011**, *13*, 634-637.

[46] T. Shinagawa, K. Takanabe, *J. Phys. Chem. C* **2015**, *119*, 20453-20458.

[47] L. D. S. Muñoz, A. Bergel, D. Féron, R. Basséguy, *Int. J. Hydrogen Energy* **2010**, *35*, 8561-8568.

[48] T. Shinagawa, K. Obata, K. Takanabe, *ChemCatChem* **2019**, *11*, 5961-5968.

[49] C. Guan, H. Wu, W. Ren, C. Yang, X. Liu, X. Ouyang, Z. Song, Y. Zhang, S. J. Pennycook, C. Cheng, J. Wang, *J. Mater. Chem. A*, **2018**, *6*, 9009-9018.

[50] R. Wu, B. Xiao, Q. Gao, Y.-R. Zheng, X.-S. Zheng, J.-F. Zhu, M.-R. Gao, S.-H. Yu, *Angew. Chem. Int. Ed.* **2018**, *57*, 15445-15449.

[51] M. Ma, G. Zhu, F. Xie, F. Qu, Z. Liu, G. Du, A. M. Asiri, Y. Yao, X. Sun, *ChemSusChem* **2017**, *10*, 3188-3192.

[52] T. Liu, L. Xie, J. Yang, R. Kong, G. Du, A. M. Asiri, X. Sun, L. Chen, *ChemElectroChem* **2017**, *4*, 1840-1845.

[53] K. Li, J. Zhang, R. Wu, Y. Yu, B. Zhang, *Adv. Sci.* **2016**, *3*, 1500426.

[54] A. Buttler, H. Spliethoff, *Renew. Sustain. Energy Rev.* **2018**, *82*, 2440-2454.

[55] P. Dieguez, A. Ursua, P. Sanchis, C. Sopena, E. Guelbenzu, L. Gandia. *Int. J. Hydrog. Energy* **2008**, *33*, 7338-7354.

[56] P. M. Diéguez, A. Ursúa, P. Sanchis, C. Sopena, E. Guelbenzu, L.M. Gandía, *Int. J. Hydrog. Energy* **2008**, *33*, 7338-7354.

[57] Y. Nakajima, N. Fujimoto, S. Hasegawa, T. Usui, *ECS Trans.* **2017**, *80*, 835-841.

[58] F. J. Pino, L. Valverde, F. Rosa, *J. Power Sources* **2011**, *196*, 4418-4426.

[59] Ø. Ulleberg, *Int. J. Hydrog. Energy* **2003**, *28*, 21-33.

2. Mechanistic understanding of oxygen evolution reaction over iridium oxide

Water electrolysis driven by renewable energy can produce clean hydrogen, but its efficiency remains low, in part because of slow kinetics at the anode for the oxygen evolution reaction (OER). Learning from the most active catalysts for the OER, iridium oxides, would be the key to the development and establishment of design guidelines for active and stable OER catalysts. This article reviews in-situ or operando spectroscopic and advanced computational studies in the past decade concerning the OER over iridium oxide for both the oxidation of water molecules and hydroxide ions. By collectively reviewing the reported findings, I illustrate the plausible OER catalytic cycles including the dissolution of iridium during the reaction, which at the same disclosed discrepancy in the proposed mechanisms. Such discrepancies are thought to originate from variations in the experimental conditions employed in those studies, calling for comprehensive and systematic in-situ or operando studies in the future. Toward the end, I discuss a recent approach for improving the activity and stability of the OER catalysts.[a]

2.1. Introduction

The transition to a sustainable society largely relies upon the utilization of renewable energy on a large scale. However, its low energy density and intermittent availability hamper the widespread implementation of renewable energy, necessitating the development of systems that allow for its conversion to other forms of energy. The electrocatalytic process is a promising candidate for this purpose, which, using the electricity generated from renewable energy, can convert thermodynamically stable substances such as H_2O and CO_2 to energy-dense or value-added chemicals.[1,2] Notwithstanding recent advances, the current technology of electrolysis fails to compete economically with fossil fuel-based counterparts,[1] calling for research efforts on the development of efficient and cost-effective electrolysis systems.

The oxygen evolution reaction (OER) is an anodic half-reaction that can be coupled with various cathodic counterparts, including the hydrogen evolution reaction (HER), the CO_2 reduction reaction, and the N_2 reduction reaction.[3-8] The fundamental study on the OER trace back to 1955, when Rüetschi et al. first attempted to rationalize the OER performance over a variety of electrodes.[9] Their study assessed the approximate bonding strength of M-OH (where M stands for metal) by analyzing the thermochemical and spectroscopic data,[9] which was plotted with respect to the overpotential at $1~A~cm^{-2}$ for the OER reported by Hickling and Hill in 1947.[10] The plot revealed that the OER overpotential linearly scaled with the M-OH bonding energy, suggesting that M−OH bonding energy may serve as a descriptor for the OER activity.[9] Later, this fundamental understanding was put forward by Trasatti in 1980,[9] which revealed a correlation between the OER overpotential and the change of enthalpy from lower to higher oxide transition of transition metal oxides, e.g., from 3+ in Ir_2O_3 to 4+ in IrO_2.[11] The disclosed correlation is volcano-shaped; a metal oxide that requires a too large enthalpic change exhibits substantial overpotential, while another metal oxide that requires a too small enthalpic change also demands a large overpotential. This trend indicates that there exists an optimal enthalpy change that minimizes the overpotential for the OER, which was found for iridium oxide and ruthenium oxide having 79.5 and $83.4~kJ~mol^{-1}$, respectively, for the transition from M_2O_3 to MO_2.[11] In fact, the iridium oxide and the ruthenium oxide are regarded even now as one of the most active OER electrocatalysts.[12-14]

These rationalizations of electrocatalysis rely on and are corroborated by experimental evidence. In the first place, the Tafel analysis might be used to elucidate the reaction mechanism and, in particular, to evaluate the rate-determining step (rds), which is the slowest

step of a multistep chemical reaction,[15] of electrochemical reactions.[16] In the case of OER over iridium oxide, the Tafel slope values under acidic aqueous media were reported to be around 30-45 mV dec^{-1}.[17,18] These values, however, could not solely determine the rds because the multiple steps nature of the OER yields a variety of theoretically anticipated Tafel slope values when the electron transfer coefficient deviates from 0.5.[16,19] This fact indicates the need for direct evidence by observing the catalyst surface via spectroscopic means to elucidate the surface state of the catalysts, the surface adsorbate on the catalysts, and in turn the reaction mechanism. Early reports in this line of study employed ex-situ experiments. Typically, as-made catalysts were characterized by techniques such as X-ray photoelectron spectroscopy (XPS) for the specification of the surface chemical state, electron microscopes for morphologies, and so on. The properties of catalyst elucidated by these characterizations were often attempted to be correlated with the catalytic performance. However, such analyses are not capable of providing a solid idea of catalysis because the catalyst material may undergo chemical and morphological changes by being placed in the actual electrolyte environment or during the catalytic reaction, which cannot be seen by characterizations performed under a vacuum of pre-reaction samples.[20-22] From this viewpoint, it is essential to investigate at least the catalyst of post-reaction. For instance, Kötz et al. studied the OER mechanism over iridium oxide by using ex-situ XPS at excitation around the O 1s and Ir 4f regions to track changes of its oxidic nature using post-reaction materials.[21,23] They firstly placed the iridium sample in 1.0 M H_2SO_4 and applied potentials of 0.0 V, 0.6 V, or 1.25 V vs. saturated calomel electrode (SCE) (corresponding to 0.25 V, 0.85 V, or 1.5 V vs. reversible hydrogen electrode (RHE) at pH 0.14), before recording the XPS spectra. The obtained spectra captured a decrease in OH contribution and an increase in oxide intensity at increasing anodic potentials applied prior to the XPS measurements. These changes were ascribed to the transition from $Ir(OH)_3$ to $IrO(OH)_2$ at 0.35 V vs. RHE that is further oxidized to IrO_3 at 1.0 V vs. RHE,[21] leading to a proposal of a catalytic redox cycle involving $Ir^{4+/5+/6+}$.[21,23] This mechanistic understanding certainly helps digest the catalytic cycles. Nevertheless, nowadays, it is commonly considered that such ex-situ measurements would not be satisfactory to fully rationalize the catalysis; e.g., the catalyst may attain a surface state different from its pristine state only during working conditions.[23-25] This gap between the catalyst states under vacuum and working conditions hampered the establishment of a solid understanding of the electrocatalysis.

From a different perspective, computational studies have advanced my understanding of the OER electrocatalysis at a molecular level. A milestone report was provided by Rossmeisl et al.[5,26,27] Their framework of density functional theory (DFT) calculations considered the concerted proton-electron transfer (CPET) steps, where one H^+ and one e^- are transferred in a single kinetic step:[28]

$$M + OH^- \rightleftharpoons M\text{-}OH + e^-, \qquad (2\text{-}1)$$

$$M\text{-}OH + OH^- \rightleftharpoons M\text{-}O + H_2O + e^-, \qquad (2\text{-}2)$$

$$M\text{-}O + OH^- \rightleftharpoons M\text{-}OOH + e^-, \qquad (2\text{-}3)$$

$$M\text{-}OOH + e^- \rightleftharpoons M + O_2 + H_2O + e^-. \qquad (2\text{-}4)$$
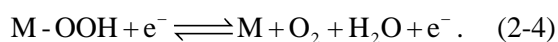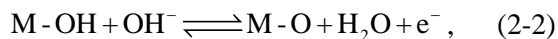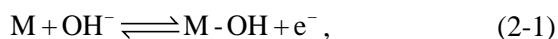
For each step, they computed free energy changes of the reaction, as well as the binding energy to the surface intermediates.[29] Digesting the changes of the free energy allowed for identifying the potential-determining step (pds) that requires the largest theoretical overpotential among steps and thus is the theoretically predicted bottleneck of the OER.[29] In addition, their study disclosed linear relationships among the binding energies of M, M-OH, M-O, and M-OOH; the so-called linear-scaling relationship.[29] Based on these findings, the theoretical OER overpotential was plotted as a function of the binding energy to the surface intermediates, e.g., M-O, which was found to be volcano-shaped.[29] The implication of this figure is that a surface that binds the reaction intermediates neither too strongly nor too weakly possesses the optimal surface, which achieves the highest OER performance.[29] This plot reproduced that the iridium oxide and the ruthenium oxide sit near the top of the volcano trend, thus corroborating the experimental observations.

Notwithstanding the success of the past computational approach, the employed model omitted several considerations for the sake of simplicity and versatility. Firstly, those models did not compute kinetics. Analysis of the free energy of the reaction intermediates to elucidate the bottleneck was justified by the linear scaling relationship between the reaction energy and the activation energy, the so-called Bronsted-Evans-Polanyi (BEP) relationship.[30] However, the BEP relationship is not always valid, and the pds and rds can differ from each other.[31] Further complicating this kinetic aspect is the variation in the OER reactant. Depending on the electrolyte pH levels, the OER can proceed either as the oxidation of the hydroxide ion (OH^-) or the water molecule (H_2O), as shown in **Equation (2-5)** or **Equation (2-6)**, respectively:[32,33]

$$4OH^- \rightleftharpoons O_2 + 2H_2O + 4e^-, \qquad (2\text{-}5)$$

$$2H_2O \rightleftharpoons O_2 + 4H^+ + 4e^-. \qquad (2\text{-}6)$$
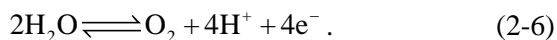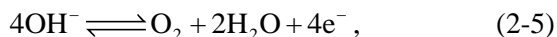
Dissociating the O-H bonding of H_2O molecules is kinetically more difficult than that of the OH^- reactant, which would lead to the reactant-switching from H_2O to OH^- when shifting the pH from near-neutral to alkaline values.[34,35] In fact, such reactant-switching was experimentally observed at around pH10-11.[19,36] Secondly, the surface state of the catalyst can vary depending on the reaction environment, which was also not considered in the simplified model. For instance, due to the acid-base equilibria at the catalyst surface in the reaction condition, the surface is deprotonated [protonated] when the pH of the electrolyte solution is larger [smaller] than the pK_a.[37] Likewise, the surface is positively [negatively] charged when the pH of the electrolyte solution is smaller [larger] than the isoelectric point (IEP) of the oxide. These changes in the surface state of catalysts can lead to subsequent changes in the reaction mechanism.[38] Thirdly, while the introduction of the computational hydrogen electrode (CHE) has simplified the treatment of potential, which makes this DFT-based approach quite versatile,[5,26,27] the model cannot consider the decoupled pathways. More specifically, although the reaction-scheme of **Equation (2-1)** – **Equation (2-4)** merely contains CPET, the reactions possibly proceed by a sequence of decoupled proton transfer (PT) or electron transfer (ET), which is the transference of only H^+ or only e^-, respectively:[28,39]

$$M + H^+ \rightleftharpoons M\text{-}H^+, \qquad (2\text{-}7)$$

$$M + e^- \rightleftharpoons M^-. \qquad (2\text{-}8)$$

All in all, while the model without these considerations has been successful in rationalizing the general trend for electrocatalysis, the further detailed understanding and development of active electrode materials require sophistication and complication of the framework.

In this context, the recent decade has witnessed the development of spectroscopic techniques that enable the direct observation of the surface state in-situ or operand[14,40] and the advancement of computational calculations that can simulate and map the catalytic cycles in more detail.[41] This review herein discusses the recent progress in understanding the OER mechanism based on in-situ or operando experimental evidence as well as computational results. I focus on iridium oxide, one of the most active OER electrocatalysts. Readers interested in other catalysts are referred to other published studies.[42-44] I illustrate plausible OER cycles via H_2O oxidation in **Section 2** and review its spectroscopic and computational support, while **Section 3** deals with those for OH^- oxidation.

Section 4 discusses the dissolution mechanisms of iridium during the OER mechanism, corroborating the catalytic cycle.

2.2. OER mechanism via H_2O oxidation over iridium oxide

The iridium oxide sits at or near the top of the volcano-shaped trend for the OER,[11,29] and has been employed in the commercial polymer electrolyte membrane (PEM) electrolyzer despite its high cost and scarcity.[45] Developing active OER catalysts composed of earth-abundant and cost-effective elements is a key to the cost-reduction and thus the penetration of hydrogen via electrolysis in the market. The rational design of such catalysts would require identification of the reaction mechanism and the working state of the best-performing iridium oxide catalysts. Accordingly, the recent decade has witnessed significant advancements in the understanding of OER electrocatalysis. Herein, this section collectively reviews the proposed mechanisms of H_2O oxidation over the iridium oxide based on spectroscopic evidence and advanced theoretical calculations. I firstly introduce an overall picture of plausible OER catalytic cycles, and subsequently review the spectroscopic and computational data supporting the scenarios in the later subsections.

2.2.1. Proposed mechanism of H_2O oxidation over iridium oxide

The existing literatures allow for the elucidation of OER catalytic cycles over the iridium oxide, illustrated in **Figure 2.1**. There have been four cycles claimed; (1) a cycle involving surface adsorbate driven by redox of iridium centre (red-colored in **Figure 2.1a**), (2) a cycle involving surface adsorbate driven by redox of the adsorbed O species (blue-colored in **Figure 2.1b**), (3) a cycle involving redox of Ir=O state (green-colored in **Figure 2.1c**), and (4) the one that involves lattice oxygen (orange-colored in **Figure 2.1d**). Below I describe each cycle in more detail.

The scenario of the red-colored cycle in **Figure 2.1a** starts with the oxidation of the initial state, Ir^{3+} (**1** in the figure), with the H_2O reactant, forming Ir^{4+}-$O^{2-}H$ surface species (**2**) and H^+ via CPET. This species is oxidized to Ir^{5+}=O^{2-} state (**3**) via a CPET step, which upon further oxidation is converted into Ir^{4+}-$O^{2-}OH$ (**4**). By releasing O_2, this state relaxes to Ir^{3+} (**1**). This cycle is consistent with the single-site mechanism commonly adopted for DFT calculations.[16,50,54]

31
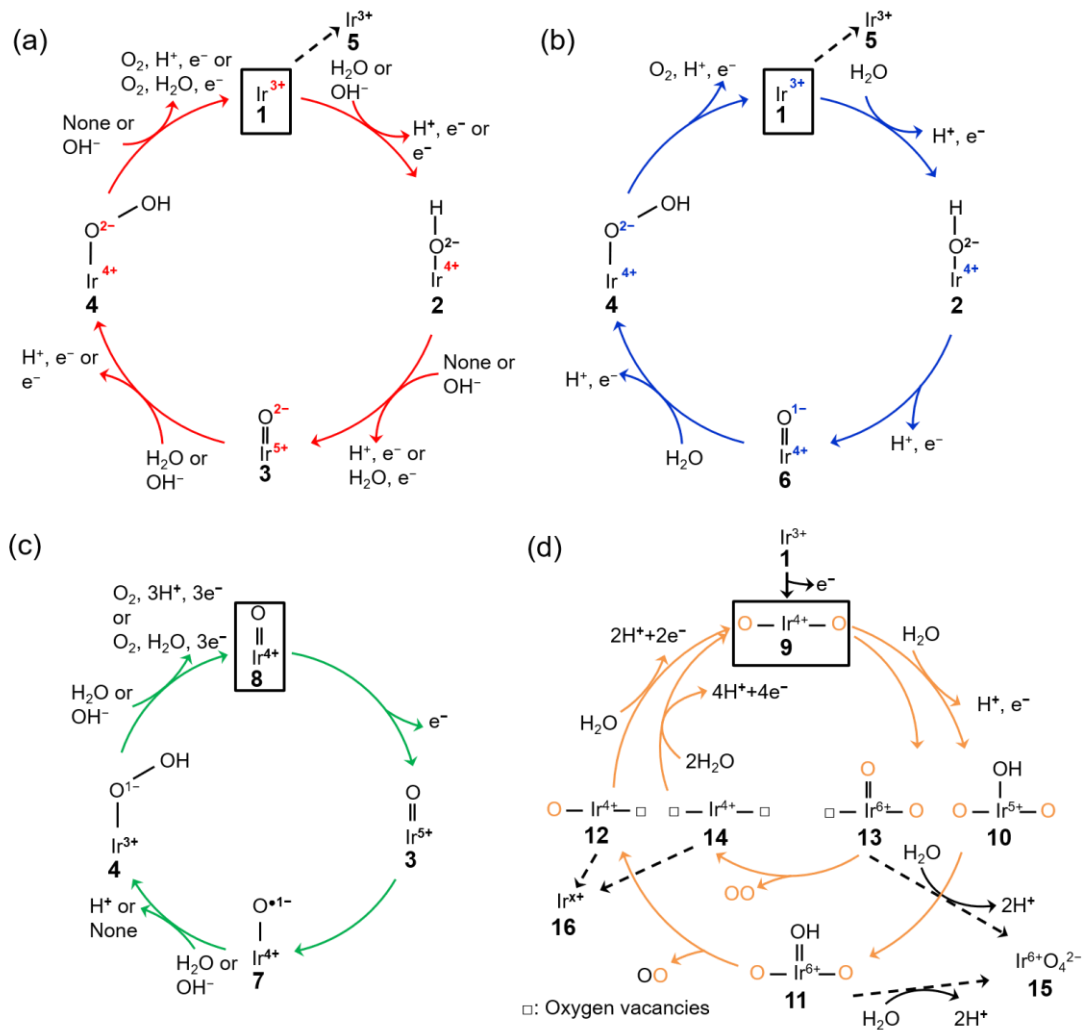
Figure 2.1. Proposed mechanism of the oxygen evolution reaction (OER) over iridium oxide. Four different colors (red, blue, green, and orange) were used to illustrate four catalytic cycles. (a) The red-colored cycle is driven by the redox of iridium centre.[17,29,46,47,66-68,95] (b) The blue-colored one proceeds via the redox of the adsorbed O species.[17,29,46-51,68,95] (c) The green-colored cycle is characterized by the redox of the Ir=O state.[17,67,68,69,58] (d) The orange-colored cycle involves the lattice oxygen, where the orange and black O represents the lattice oxygen and adsorbed oxygen species, respectively.[63,65,71-74] The squares represent the initial state of each cycle, and the dashed lines indicate the dissolution path of iridium species. The (a) red, (b) blue, (c) green, and (d) orange cycles were reported for the H_2O oxidation, while the (a) red and (c) green cycles were also reported for OH^- oxidation as depicted in the figures.

The second scenario (blue-colored in **Figure 2.1b**) is similar to the first one except that the surface redox species is not only the iridium but also the oxygen. Firstly, the Ir^{3+} (**1**) is attacked by the H_2O reactant, and forms Ir^{4+}-O^{2-}H surface species (**2**) with releasing H^+ via CPET. This species is oxidized via a CPET step into $Ir^{4+}=O^{1-}$ state (**6**), which contains the electrophilic oxygen species (O^{1-}) as a reactive intermediate.[48-51] The $Ir^{4+}=O^{1-}$ experiences further oxidation with a H_2O molecule to form Ir^{4+}-O^{2-}OH (**4**) via a CPET step. This state relaxes to Ir^{3+} (**1**) with releasing O_2 via CPET.

In contrast to the first two scenarios that involve the redox of either iridium or oxygen, the green-colored cycle in **Figure 2.1c** proceeds by the redox of Ir=O states. The initial $Ir^{4+}=O$ (**8**) changed oxidation state to $Ir^{5+}=O$ (**3**) via ET. This $Ir^{5+}=O$ species (**3**) is the precursor to the reactive oxyl species[31,52-57] of Ir^{4+}-$O^{\bullet1-}$ (**7**) that reacts to form Ir^{3+}-O^{1-}OH (**4**) via PT. The formed Ir^{3+}-O^{1-}OH (**4**) release O_2 with H_2O reactant and relaxes to $Ir^{4+}=O$ (**8**) via CPET. This route likely appears at high overpotential (e.g., > 2.4 V vs. RHE),[58] where the accumulation of charge is considered to occur.[59]

The last cycle in orange-colored in **Figure 2.1d** proceeds via the releasing and filling of an oxygen vacancy at the iridium oxide surface, which was named the lattice oxygen evolving reaction (LOER) mechanism or lattice oxygen participated mechanism (LOM).[60,61] This route likely appears at highly anodic potentials (e.g., > 1.6 V vs. RHE for electrochemically prepared oxide from metallic iridium).[62,63] In this scenario, two pathways are considered depending on the number of lattice oxygen atoms participating in the reaction. The first one depicted in the outer circle starts with the oxidation of the $Ir^{3+}=O$ (**1**) to form O-Ir^{4+}-O (**9**) via ET. Lattice O bridging iridium sites of this O-Ir^{4+}-O (**9**) is attacked by the H_2O molecule to form O-Ir^{5+}(-OH)-O (**10**) via PCET, which transforms into O-Ir^{6+}(=O)-O (**11**) via CPET. This species releases oxygen to form O-Ir^{4+}-□ species (**12**) where □ represents a vacant site, and this formed vacancy is subsequently filled by the attack of H_2O to form O-Ir^{4+}-O (**9**) via PCET. In the second pathway depicted in the orange-colored inner circle of **Figure 2.1d**, evolved O_2 consists of two lattice oxygen.[64] In detail, the lattice O bridging the iridium sites (**9**) leaches out from the lattice to form □-Ir^{6+}(=O)-O (**13**). Subsequently, this □-Ir^{6+}(=O)-O state (**13**) releases O_2 to form □-Ir^{4+}-□ (**14**), where the two oxygen vacancies are filled by the attack of H_2O to form O-Ir^{4+}-O (**9**) via CPET.

2.2.2. Spectroscopic evidence to support the claimed catalytic cycle for H_2O oxidation over iridium oxide

The OER catalytic cycles detailed in the previous section were drawn based on the recent in-situ and operando characterizations, which allowed for determining the working states of catalysts.[65] The employed techniques include X-ray absorption near-edge structure (XANES), near-edge X-ray absorption fine structure (NEXAFS), X-ray absorption (XAS), XPS, and Raman spectroscopy. The key observations in the literature are highlighted and summarized in **Figure 2.2** that elucidated the OER electrocatalysis over iridium oxide.

Initially, the spectroscopic evidence supporting the catalytic cycle in **Figure 2.1a** was provided by an in-situ XPS study in 2014.[66] The group of Nilsson conducted in-situ XPS measurements using IrO_2 nanoparticles with the applied potential of 1.75 V vs. RHE in the presence of 10 Torr of H_2O, i.e., neither acidic nor alkaline.[66] By analysing the XPS spectra in the Ir 4f region, they found that the IrO_2 sample at open-circuit potential (OCP) retained Ir^{4+} state upon exposure to H_2O. Interestingly, the spectra exhibited a shoulder when an anodic potential of 1.75 V vs. RHE was applied, ascribed to the appearance of Ir^{+5}. In the same study, they also examined the excitation around the O 1s region, and found that when the potential was switched from OCP to 1.75 V vs. RHE, the relative intensity of the peak ascribable to hydroxide species decreased while that of oxide increased.[66] Taken together, their observation pointed to the deprotonation reaction during the course of OER accompanying the oxidation of Ir^{4+} into Ir^{5+} states. This observation elucidates the change in the oxidation state of iridium during the catalytic cycle, corresponding to the transformation of Ir^{4+}-$O^{2-}H^+$ (**2**) into $Ir^{5+}=O^{2-}$ (**3**) in the red-colored cycle in **Figure 2.1a**.

In 2014 and 2015, Rondinini and co-workers reported in-situ Ir-L_{III} XANES that also supports the red-colored catalytic cycle in **Figure 2.1a**.[67,68] The group investigated the XANES spectra over hydrous iridium oxide catalyst in the acidic solution of 0.5 M H_2SO_4 at varying potentials from 0.2 to 1.6 V vs. RHE, and their key result is shown in **Figure 2.2a**.[67] The **panel I** of the figure displays white lines of the absorption in the Ir-L_{III} region at various potentials. When increasing the potential from 0.2 to 0.7 V vs. RHE, the white line position remained identical, being similar to that of $IrCl_3$ reference (the **panel ii**), which indicates the presence of the Ir^{3+} state. When the potential was further anodically shifted to 1.0 V vs. RHE, the white line position shifted toward higher energies. Because the resulting position at 1.0 V

vs. RHE was identical to the IrO_2 reference (the **panel ii**), the shift indicates the oxidation of Ir^{3+} into Ir^{4+} states. They further analysed the second derivatives of the spectra as shown in the **panel iii** of **Figure 2.2a**. The figures displays double peak structures at 0.7 V and 1.3 V vs. RHE, which were ascribable to the transition from the Ir 2p levels to the split ($t_{2g}+e_g$) 5d states, indicating the presence of Ir^{4+} and Ir^{5+} at 0.7 V and 1.3 V vs. RHE, respectively.[67] Collectively, their study proposed that iridium oxide changes its oxidation state from Ir^{3+} to Ir^{4+} at around 1.0 V vs. RHE and further to Ir^{5+} above 1.3 V vs. RHE (from **1** to **3** or **1** to **6** in **Figure 2.1**), thus supporting the red- and green-colored cycle displayed in **Figure 2.1a and 2.1c**.

In contrast, a study was reported in 2016 by Schlögl and co-workers that supports, based on NEXAFS, the anion redox mechanism discussed as the blue-colored second scenario of **Figure 2.1b**.[48-51] The group recorded in-situ NEXAFS spectra in the O K-edge region using a sputtered iridium catalyst at varying potentials of OCP, 1.6, 1.8, and 2.0 V vs. standard hydrogen electrode (SHE) in 0.1 M H_2SO_4 solution at 0.3 Pa as shown in **Figure 2.2b**.[48] The spectra exhibited a broad peak, which was deconvoluted into two; one at the smaller energy was thought to originate from the electron-deficient oxygen species, and another one at the larger energy represents O^{2-} species. The study labelled the former one as O^{1-}, although it is still under debate whether the electron-deficient oxygen is electrophilic oxygen (O^{1-}) or an oxyl radical ($O^{\bullet 1-}$).[31,52-57] At more positive potentials, a hump appeared at the peak shoulder, indicating an increased contribution from the O^{1-} state. In correlating to the OER activity, they found that the OER performance linearly scaled with the fraction of not O^{2-} but O^{1-}, and thus concluded that the electrophilic O^{1-} species (**6** in **Figure 2.1b**) is the active species in catalysing the OER on the iridium oxide.[48] I note that these species were observed at potentials above 1.6 V in **Figure 2.2c** higher than the potentials employed in other cases, implying that this route may become likely apparent at higher overpotential regions. This view is compatible with a recent study claiming the charging up of iridium species at highly anodic conditions.[59]
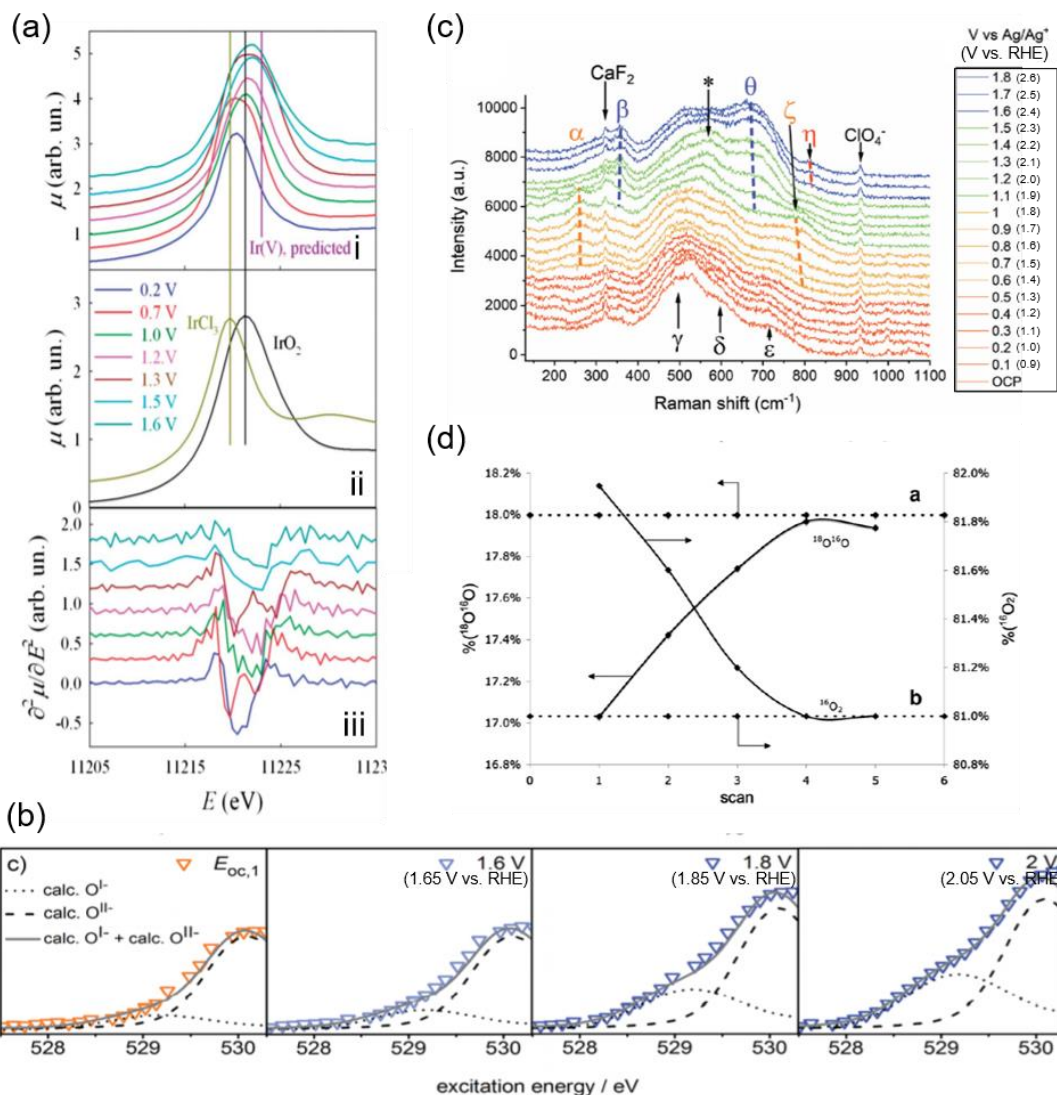
Figure 2.2. Spectroscopic data for H$_2$O oxidation over iridium oxide. (a) In-situ Ir-L$_{III}$ X-ray absorption near-edge structure (XANES) spectra using hydrous iridium oxide with the applied potential from 0.2 to 1.6 V vs. reversible hydrogen electrode (RHE) in 0.5 M H$_2$SO$_4$ solutions. White lines of the absorption in the Ir-L$_{III}$ region are shown for the iridium oxide at various potentials in the panel (i), and over the reference IrCl$_3$ and IrO$_2$ in the panel (ii), and the second derivatives of the spectra shown in the panel (i) is plotted in the panel (iii). Reproduced from ref. 67 with permission from the Royal Society of Chemistry. (b) In-situ near-edge X-ray absorption fine structure (NEXAFS) spectra in the O K-edge region in 0.1 M H$_2$SO$_4$ at 0.3 Pa at open circuit potential (OCP), 1.6, 1.8, and 2.0 V vs. standard hydrogen electrode (SHE) (corresponding to 1.66 V, 1.86 V, or 2.05 V vs. RHE at

pH 0.97) using a sputtered iridium catalyst. Reproduced from ref. 48 with permission from the Royal Society of Chemistry. (c) In-situ shell-isolated nanoparticle-enhanced Raman spectroscopy (SHINERS) spectra using electrochemically deposited iridium oxide in 0.1 M NaClO$_4$ solutions at pH 10 at varying potentials from OCP to 1.8 V vs. Ag/Ag$^+$ (corresponding to 2.6 V vs. RHE at pH 10). Reproduced from ref. 58 with permission from the Royal Society of Chemistry. (d) Differential electrochemical mass spectrometry (DEMS) results during cyclic voltammogram in a potential window from ca. 0.05 V to 1.6 V vs. SHE (corresponding to ca. 0.05 V to 1.6 V vs. RHE at pH 0) in a 1 M HClO$_4$ solution containing 10 wt. % H$_2$^{18}O over thermally prepared Ir^{16}O$_2$/Ti catalyst. Reprinted with permission from ref. 65. Copyright (2018) Elsevier.

The experimental evidence supporting the green-colored third scenario depicted in **Figure 2.1c** was provided using Raman spectroscopy.[58,69] In 2020, Saeed et al. conducted in-situ shell-isolated nanoparticle-enhanced Raman spectroscopy (SHINERS)[58] using electrochemically deposited iridium oxide in 0.1 M NaClO$_4$ solutions at pH 10 at varying potentials from OCP to 1.8 V vs. Ag/Ag$^+$ (corresponding to 2.6 V vs. RHE at pH 10).[58] The measured spectra shown in **Figure 2.2c** were divided into four distinct regions depending on the spectra features, (I) OCP to 0.5 V vs. Ag/Ag$^+$ (corresponding to 1.3 V vs. RHE at pH 10), (II) 0.6 to 1.0 V vs. Ag/Ag$^+$ (corresponding to 1.4 V to 1.8 V vs. RHE at pH 10), (III) 1.1 to 1.5 V vs. Ag/Ag$^+$ (corresponding to 1.9 V to 2.3 V vs. RHE at pH 10), and (IV)1.6 to 1.8 V vs. Ag/Ag$^+$ (corresponding to 2.4 V to 2.6 V vs. RHE at pH 10), which are respectively red-, orange-, green-, and blue-colored in the figure. The spectra exhibited multiple peaks, ascribed to Ir-O-Ir twist, Ir-O-Ir stretch, or Ir=O stretch based on the previous Raman studies.[69,70] More specifically, the peaks labelled as α (252 cm^{-1}) and β (357 cm^{-1}) were both assigned to Ir-O-Ir twist at different iridium oxidation states; the former contains Ir$^{4+,}$ and the latter contains Ir$^{>4+}$.[69,70] The five peaks of γ (504 cm^{-1}), δ (608 cm^{-1}), ε (719 cm^{-1}), ζ (773 cm^{-1}), and θ (672 cm^{-1}) were all ascribed to the Ir-O-Ir stretch; δ was observed at the iridium oxidation state of +3, and γ, ε, and ζ were apparent for Ir^{+4}, while θ indicates the higher oxidation state of Ir$^{>+4}$.[69,70] The one at η (813 cm^{-1}) was thought to originate from Ir=O stretch at Ir$^{>4+}$.[69,70] Regarding the assignment of this peak η in detail, previously the group of Schögel investigated the influences of isotopes on the peak, and observed that this peak η was insensitive to the isotope H and D, indicative of the absence H species in the vibration.[69] In addition, in an experiment using solution containing 50:50 (H$_2$O^{16}:H$_2$O^{18}), only two peaks of

nearly equal intensity were observed as η, which suggests that this vibration contains single O atom, or the absence of O-O.[69] Furthermore, although the peak-shift of single bonding Ir-O due to the substitution of O^{16} for O^{18} was calculated to be 45 cm^{-1}, the observed shift was 59 cm^{-1}. These observations led to a conclusion in the study that the peak η originated from Ir=O.[69]

In the region (I) of **Figure 2.2c**, the γ, δ, and ε peaks were apparent, indicative of the presence of the Ir^{4+} state. When entering the region (II), an additional feature was observed in the spectra at α and ζ, which suggests that iridium species were still mostly composed of 4+ states. In the region (III), the spectra exhibited contributions from β and θ, which implies the formation of >4+ states. These β and θ states persisted also in the region (IV), where additionally the peak η appeared. Importantly, subsequent SHINERS spectroscopy combining the isotope labelling testing using D_2O-based solutions (1 M $NaClO_4$ at pD 10) demonstrated almost no change in the peak position of η from 813 cm^{-1} (in H_2O) to 817 cm^{-1} (in D_2O). Thus, they concluded that all peaks do not contain H elements such as hydroxides, peroxides, or the oxyl radical species, which are considered as the precursor for the O-O bond formation.[69] This study proposed that the OER catalytic cycle contains three intermediates, which all have an Ir-O bond, before rate-determining OOH formation, as shown in **Figure 2.1c**.

The orange-colored last scenario of LOER in **Figure 2.1d** was supported by studies using mass spectroscopy in conjunction with an isotope labelling.[65,71-74] In 2007, Fierro et al. conducted differential electrochemical mass spectrometry (DEMS) measurements during cyclic voltammogram (CV) in a potential window from ca. 0.05 V to ca. 1.6 V vs. SHE (corresponding to ca. 0.05 V to ca. 1.6 V vs. RHE at pH 0) in a 1 M $HClO_4$ solution containing 10 wt. % $H_2^{18}O$ using thermally prepared $Ir^{16}O_2/Ti$ catalyst, and their results are shown in **Figure 2.2d**.[65] Their study tracked the identity of evolved O_2 (either $^{16}O_2$ or $^{18}O^{16}O$) while recording the CVs. **Figure 2.2d** shows the composition of $^{18}O^{16}O$ and $^{16}O_2$ at each CV scan, disclosing that the composition of $^{16}O_2$ decreased with the cycle number while that of $^{16}O^{18}O$ increased from 17% to 18% until reaching a steady-state after the third cycle. To corroborate this observation, they performed additional CV-DEMS experiment using $Ir^{18}O_x$ in a 1 M $HClO_4$ containing ca. 10% $H_2^{18}O$. Their results showed that the evolved O_2 gas was initially composed of $^{18}O^{16}O$ at 0.9% in the first scan and was < 0.5% after the fifth scan with a concomitant increase of $^{16}O_2$ composition. These results allowed them to reason the

exchanging of lattice O of iridium oxide with O in the solution during the OER at steady-state, and thus the participation of lattice oxygen in the OER mechanism as depicted in the orange-colored cycle in **Figure 2.1d**.

In addition to the spectroscopic study, morphological observations such as electron microscopy[75-77] also shed light on the catalysis of iridium oxide. For instance, in 2017, Willinger et al. reported the key structural feature of the active iridium oxide by comparing the structural features of the more active, which was hydrothermally prepared and denoted as IrO_x-(FHI), and the less active, which was commercially available and denoted as IrO_x-commercial, iridium oxide samples.[75] By analysing the observed images of high-angle annular dark field scanning transmission electron microscopy (HAADF STEM), they found larger amount of the tunnel-like motifs of hollandite structure in the IrO_x-FHI than that in the IrO_x-commercial,[75] which was considered to be an active motif for the OER.[78] Their subsequent electron pair distribution function (ePDF) analysis suggested that the IrO_x-FHI consisted of the hollandite structure, whereas the IrO_x-commercial consisted of 60% hollandite and 40% rutile unit cell.[75] This observations allowed for proposing that the hollandite structure is the key for the highly active OER catalyst of iridium oxide.[75] These studies demonstrate the significance of morphological aspect on the OER activity.

Being one pillar of catalysts, metal single-site catalysts have attracted increasing interests in recent years.[79-82] In 2020, in-situ XAS study observing oxidation state of atomically dispersed iridium oxide on indium tin oxide (ITO) in 0.1 M $HClO_4$ during OER was reported by Lebedev et al.[79] They measured in-situ XANES at Ir L_{III}-edge at 1.46 V vs. RHE and assigned Ir-O distance of 1.83 ±0.02 Å as $Ir^{+5}=O$ intermediate, which was predominant species under OER conditions.[79] Subsequently, the same authors further investigated the reaction mechanism by DFT calculation and suggested the formation of Ir^{+6} dioxo intermediate after the formation of $Ir^{+5}=O$ intermediate.[79] This result of the formation of $Ir^{+5}=O$ is consistent with the observations on the heterogeneous solid states as discussed in this review.[67] This type of study would deepen the understanding of the OER catalysis from a comprehensive perspective, and furthermore would eventually could bridge the gap between the heterogeneous and homogeneous catalysis.[83-85]

As described above, recent in-situ and operando characterizations captured the oxidation state of the active site and surface intermediate during the OER. The experimental evidence

in **Figure 2.2** helps in reasoning the catalytic cycles, shaping the ones in **Figure 2.1**. Notwithstanding the successful applications of these techniques to the electrocatalytic OER, there remains a discrepancy among studies about the oxidation state of iridium and oxygen as well as the surface intermediate, and thus the reaction mechanism. This discrepancy likely arises because of the non-unified catalyst and experimental conditions among reported studies, calling for further systematic investigations of OER over iridium oxide with these sophisticated techniques.

2.2.3. Theoretical study corroborating the mechanism of H_2O oxidation over iridium oxide

Theoretical studies help elucidate the reaction mechanism at molecular levels, and thus corroborate the experimental observations. Here in this subsection, I review selected theoretical studies on the OER over iridium oxide considering kinetics[46,47,86] that were omitted in the previously established DFT models.[5,26,27]

Ping et al. considered possible reaction pathways over IrO_2(110) surface, and computed reaction rates based on the microkinetic models at the constant potential of 1.36 V vs. normal hydrogen electrode (NHE) at pH 0 (corresponding to 1.36 V vs. RHE at pH 0).[46] **Figure 2.3a** and **2.3b** show the reaction intermediates and transition state (TS) structures as well as their free energy profile. In **Figure 2.3a**, their considered model proceeds as follows: the initial state having Ir(OH)-O-Ir(OH) species (**1"**) is partially deprotonated to form Ir(OH)-O-Ir(O) (**1'**). Then, two scenarios were considered after the formation of this species (**1'**). In the first scenario, the species (**1'**) experiences deprotonation to form Ir(O)-O-Ir(O) (**1**) that is then attacked by H_2O (**TS1**) and forms Ir(OH)-O-Ir(OOH) (**2**). Alternatively, Ir(OH)-O-Ir(O) (**1'**) is attacked by H_2O (**TS1'**) and is transformed into Ir(OH$_2$)-O-Ir(OOH) (**2'**), which is then deprotonated to form Ir(OH)-O-Ir(OOH) (**2**). The thus formed species (**2**) is deprotonated to form Ir(OH)-O-Ir(OO) (**3**) and subsequently Ir(O)-O-Ir(OO) (**4**). The species (**4**) releases O_2 (**TS2**) and is protonated to Ir(O)-O-Ir(OH$_2$) (**5**), which via internal PT transforms back to the initial state (**1"**). To assess the feasibility of the pathways, they computed the reaction barrier at **TS1** and **TS1'**, which amounted to 0.6 and 0.5 eV, respectively, as compiled in **Figure 2.3b**. Notably, they thus proposed that a thermodynamically less favourable pathway (**1'** → **TS1'** → **2'** → **2**) could be kinetically more favourable.[46] This rationalization deepens the catalyst cycle in **Figure 2.1** with the proposal of rds being the formation of OOH (**4** in **Figure 2.1a-1c**).
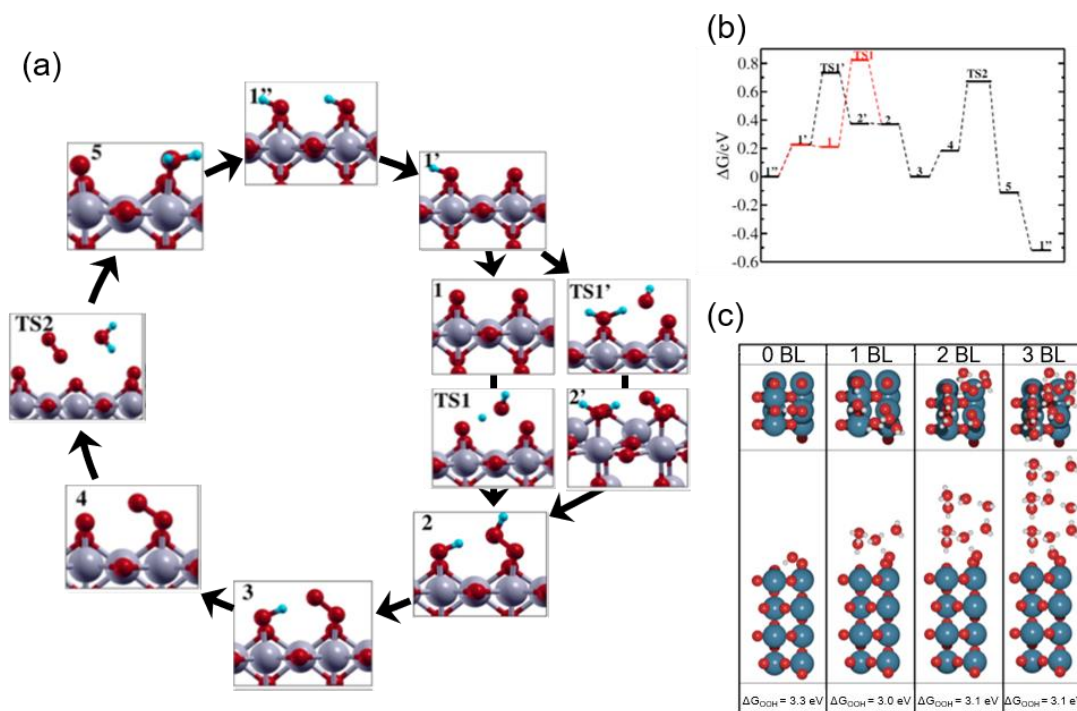
Figure 2.3. Theoretical studies for H₂O oxidation over iridium oxide. (a) Considered reaction pathways for the OER over IrO₂(110) surface; red balls are O; blue balls are H; silver balls are Ir. (b) Computed reaction free energy diagram at the constant potential of 1.36 V vs. normalized hydrogen electrode (NHE) at pH 0 (corresponding to 1.36 V vs. RHE at pH 0) corresponding to mechanism shown in the panel (a). Reprinted with permission from ref. 46. Copyright (2017) American Chemical Society. (c) The most stable structure for IrO₂(110) surface with adsorbed *OOH at the coordinatively unsaturated metal sites (CUS), *O on the neighboring CUS, and *O at bridge, together with varying numbers of water bilayers (BL); blue balls are Ir; red balls are O; white balls are H. Reprinted with permission from ref. 47. Copyright (2017) American Chemical Society.

To investigate the influence of solvent on the conformation of reaction intermediate during the OER, Gauthier et al. studied the interface between rutile IrO₂(110) and H₂O.[47] **Figure 2.3c** shows the most stable structures found for the IrO₂(110) surface with adsorbed *OOH at the coordinatively unsaturated metal sites (CUS), *O on the neighbouring CUS, and *O at the bridge, together with varying numbers of water bilayers (BL).[47] In the absence of explicit solvent (0 BL), the geometry of adsorbed intermediates was determined by interaction among the surface species; the hydrogen of the *OOH species was the most stable when *OOH was

directed to the bridging O with hydrogen bond as illustrated in **Figure 2.3c** (0 BL). The presence of explicit solvent (1-3 BL) changed the dominant interaction of the H element in the adsorbed *OOH species from that with the surface to that with the BL. **Figure 2.3c** (1-3 BL) illustrates the conformation in the presence of solvent: A more stable structure was found when a hydrogen bond was formed between the H of *OOH and the explicit solvent. Notably, as long as BL was taken into account, the number of BL had little influence on the calculation results. Thus, the bond structure of the active adsorbate was likely determined by the explicit solvent rather than the neighbouring adsorbate. Although by the subsequent thermodynamic calculation with the solvent, they observed that the reaction pathway was relatively unchanged by the inclusion of explicit solvent, the solvent was found to stabilize the OOH adsorbate by about 0.3 eV. This study was consistent with the reaction intermediates shown in **Figure 2.1a-2.1c**, and provided new insights into the conformation of surface species by considering the effect of the solvent that shall impact the kinetics.

These advanced theoretical calculations demonstrated quantitatively the significance of kinetic barrier and solvent on the OER electrocatalysis. The insights provided in those studies help in picturing the transition state in the ideal scenario and would shed light on the rational design of active catalysts. In addition, theoretical studies may be able to assess the feasibility of catalytic cycles proposed by experiments (the four scenarios in **Figure 2.1**) and may refine my view into electrocatalysis in the coming future.

2.3. OER mechanism via OH$^-$ oxidation over iridium oxide

There have been a limited number of studies on the OER over iridium oxide at alkaline pH levels, plausibly because of its lower OER stability than in the acidic condition[13,87] and the existence of alternative catalyst active toward the OER such as NiFeO$_x$.[13,87] Nonetheless, the investigation and elucidation of the OER over iridium oxide under the alkaline pH condition are of great significance because of two reasons. Firstly, the OER reactant varies with pH levels; H$_2$O and OH$^-$ at acidic and alkaline pH levels, respectively, which corresponds to variation in the transition state and thus kinetics at different pH levels over the iridium oxide. Understanding OER kinetics over the iridium oxide in distinct conditions forms a generalized view into its catalysis, which would help rationally design OER catalysts. Secondly, increasing attention has recently been given to the OER at the near-neutral pH levels in

buffered conditions,[42,88-90] where the OER can proceed also as the oxidation of OH^-. Insights into the OER at alkaline pH thus certainly help advance the electrocatalysis at the near-neutral pH conditions. I in this section describe firstly the mechanism of OH^- oxidation, before detailing spectroscopic evidence and theoretical calculations supporting the mechanism.

2.3.1.　Proposed mechanism of OH^- oxidation over iridium oxide

There are two proposed OER mechanisms via OH^- oxidation over iridium oxide that are essentially shared with those for the oxidation of H_2O, depicted in **Figure 2.1**: (1) a cycle involving surface adsorbate driven by redox of iridium centre (the red-colored cycle in **Figure 2.1a**), and (2) a cycle involving redox of the Ir=O state (the green-colored cycle in **Figure 2.1c**). Notably, the difference between those cycles and the corresponding ones at acidic pH levels is that instead of the involvement of H_2O, the cycles at alkaline pH consume OH^- reactant. In the next sections, I review reported studies supporting those scenarios.

2.3.2.　Spectroscopic evidence to support the claimed catalytic cycle for OH^- oxidation over iridium oxide

In 2017, Ooka et al. reported the presence of Ir^{5+} at the rds using ultraviolet-visible light (UV-Vis) spectroscopy.[17,91] They employed in-situ evanescent wave (EW) spectroscopy at 1.2, 1.4, and 1.5 V vs. RHE in solutions at various pH levels from 2 to 12 over anodically deposited iridium oxide.[17] **Figure 2.4a** shows the EW spectra measured at pH 12, in which two absorption peaks were apparent at approximately 410 and 580 nm at 1.2 V vs. RHE, assigned to Ir^{5+} and Ir^{4+}, respectively, based on the previous UV-vis study.[38] Interestingly, the former peak continuously shifted toward higher wavelengths at more positive potentials, ending at 456 nm at 1.5 V vs. RHE. Based on their previous time-dependent DFT (TDDFT) calculation result that theoretically elucidated spin-states,[91] they considered that this shift from 410 to 456 nm with the potential was due to the change of the spin of two adjacent oxygen ligands from symmetric to asymmetric ones, which they proposed as a state of iridium centre at the rds. Their study also examined the absorption at different pH levels, and the potential at which these absorptions appeared on the RHE scale is compiled as a function of pH in **Figure 2.4b**. In the figure, the absorptions at 410, 450 nm (as an approximate representative of 456 nm), and 580 nm are denoted as Abs 410 nm, Abs 450 nm, and Abs 580 nm, respectively, and $U_{onset,j}$ stands for the onset potential of the OER. Interestingly, the

potentials for Abs 580 nm and Abs 410 nm shifted as the pH value with a slope of 30 mV pH^{-1} on the RHE scale, implying that the redox reaction proceeds with transferring more than one proton per electron.[92] In contrast, the potential for Abs 450 nm and OER onset were mostly insensitive to the pH values in **Figure 2.4b**. This consistent insensitivity implies that the rds of the OER over iridium oxide was not the valence change of iridium centre, but the activation of the oxygen ligand, such as the activation of O^{2-} to form O^{-}.[17,48,50] Overall, this study considered oxidation states consistent with the transition from $\mathbf{Ir^{4+}\text{-}O^{2-}H^{+}}$ **(2)** to $\mathbf{Ir^{5+}\text{=}O^{2-}}$ **(3)** in the red-colored cycle of **Figure 2.1a**, and proposed that the activation of the oxygen ligand would take place over $\mathbf{Ir^{4+}\text{=}O^{1-}}$ **(6) as the rds**.
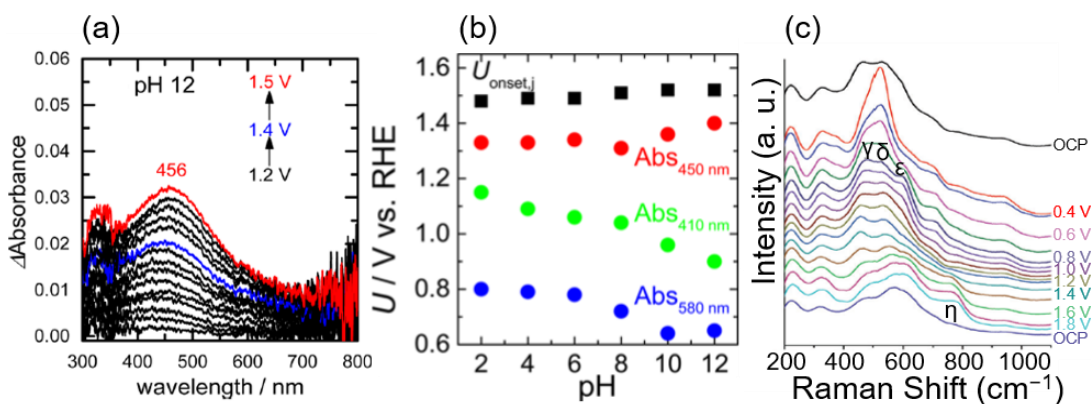
Figure 2.4. Spectroscopic data for OH^{-} oxidation over iridium oxide. (a) In-situ evanescent wave (EW) spectra in a mixed solution (NaOH, Britton-Robinson buffer and Na_2SO_4) at pH 12 over anodically deposited iridium oxide with varying potential from 1.2 to 1.5 V vs. RHE. (b) Potentials for the OER onset (black), absorption at 450 nm (red), 410 nm, (green), and 580 nm (blue) on the RHE scale compiled as a function of pH, recorded in mixed solutions (NaOH, Britton-Robinson buffer and Na_2SO_4) from pH 2 to 12 over anodically deposited iridium oxide. Reprinted with permission from ref. 17. Copyright (2017) American Chemical Society. (c) In-situ surface-enhanced Raman spectroscopy (SERS) at varying potentials from OCP to 1.8 V vs. RHE in 0.1 M NaOH using iridium oxide on an Au substrate. Reproduced from ref. 69 with permission from the Royal Society of Chemistry.

In 2017, Pavlovic et al. reported a result of in-situ Raman spectroscopy that supports the green-colored catalytic cycle in **Figure 2.1**.[69] The group conducted in-situ surface-enhanced

Raman spectroscopy (SERS) at varying potentials from OCP to 1.8 V vs. RHE in 0.1 M NaOH using iridium oxide on an Au substrate, and the obtained spectra are shown in **Figure 2.4c**.[69] At OCP, they observed peaks at 465, 527, 600, 702 cm^{-1}, which were attributed to the Ir-O-Ir stretch vibrations of μ-oxo type oxygen linkages.[70] As increasing the potential to 0.4 V, new peaks δ, ε, and γ appeared at 520, 595, and 476 cm^{-1}, ascribable to Ir-O stretch.[70] The spectra remained unchanged until reaching > 1.4 V, where an additional peak was observed at 771 cm^{-1} labelled as η. Their additional experiments employing isotope D revealed that this peak η was insensitive to the isotope H and D. In contrast, isotope labelling with ^{18}O led to a shift of 59 cm^{-1}, which differed from the expected shift of 45 cm^{-1} for the surface species containing single bonding of Ir-O. Based on these observations, they hypothesized that the peak η originated from Ir=O vibration as opposed to any other species that contained O–O, or OH vibration,[69] which would serve as a precursor to the reactive oxyl species.[93,94] This Ir=O corresponds the species **3** in **Figure 2.1 a** and **1c**, and species **6** in **Figure 2.1b**. The species **3** in **Figure 2.1c** would transform into the reactive oxyl species **7** in **Figure 2.1c**.

2.3.3. Theoretical study corroborating the mechanism of OH$^-$ oxidation over iridium oxide

A rigorous analysis for the OER mechanism concerning both the kinetics and thermodynamics was provided in 2019 by the group of Exner.[95] Their approach relied on (1) DFT calculations to determine the free energy of the reaction intermediate and construct ab initio Pourbaix diagram,[96-100] and (2) Tafel plots[46,47,96,101,102] to determine the electron transfer coefficient and free energies of rate-determining transition state,[95,103] under the assumption of the Ir, Ir-OH, Ir=O and Ir-OOH intermediates. These considerations can be combined to construct a free energy diagram at a given overpotential, which allowed for pinning-down the variation in the rds with applied overpotentials. Their ab initio Pourbaix diagram for IrO$_2$(110) is shown in **Figure 2.5a**, and a representative free energy diagram over IrO$_2$(110) at an OER overpotential (η_{OER}) of 0.47 V in alkaline solution at pH 12.9 is presented in **Figure 2.5b**. Interestingly, their analysis disclosed that at η_{OER} > 0.3 V, Ir-OOH is the thermodynamically most stable surface, and its conversion into Ir with releasing O$_2$ is the rds at η_{OER} > 0.34 V,[95] contrasting to the common understanding of the rds being the formation of O-O bonding.[29,46,47,96,101,102] This study corroborated the cycle in **Figure 2.1a-2.1c**, with a new insight that the not the formation but the decomposition of OOH determines the rate.
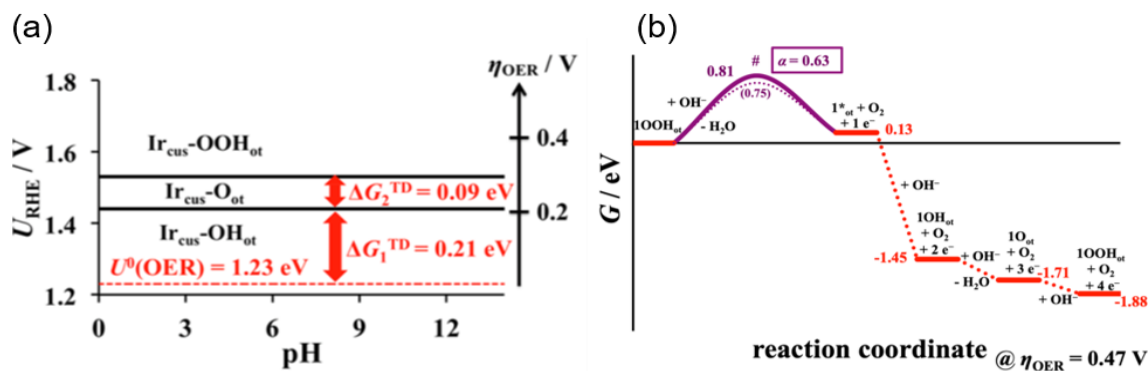
Figure 2.5. Theoretical studies for OH⁻ oxidation over iridium oxide. (a) The ab-initio Pourbaix diagram for a single-crystalline $IrO_2(110)$. (b) The free energy diagram over $IrO_2(110)$ in alkaline media (pH = 12.9) at an OER overpotential of 0.47 V. Reprinted with permission from ref. 95. Copyright (2019) American Chemical Society.

2.4. Dissolution of iridium oxide during OER

Although the degradation of OER activity over iridium oxide was observed in both acidic and alkaline solutions,[13,101] mechanistic studies on the dissolution of iridium have been reported only in acidic solutions.[62,71,72,104] Two types of dissolution pathways were proposed; (1) dissolving via redox of iridium centre as Ir^{3+} (**5**) in **Figure 2.1a** and **2.1b**, (2) dissolving with releasing oxygen atom in iridium oxide as Ir^{6+} (**15**) or Ir^{x+} (**16**) during LOER in **Figure 2.1d**. The measurements were basically performed by electrochemical testing using scanning flow cell (SFC) with mass spectroscopy such as inductively coupled plasma mass spectrometry (ICP-MS) or with online electrochemical mass spectrometry (OLEMS),[62,71,72] and key results are shown in **Figure 2.6**.

In 2018, Kasian et al. reported the dissolution reaction of iridium oxide in acidic conditions using SFC coupled with OLEMS or ICP-MS.[62] Their measurements were conducted in 0.1 M $HClO_4$ solutions at a constant current density of 5, 10, 15, or 20 mA cm⁻² for 30 s, using three types of iridium oxide; namely, electrochemically prepared oxide from metallic iridium (denoted as metallic Ir), reactively sputtered IrO_2, and thermally prepared iridium oxide. **Figure 2.6a** shows, as a function of the applied current density, the amount of dissolved iridium species in **panel i**, integrated signals of mass spectra at mass-to-charge ratios (m/z) of 240 as the representative of dissolved IrO_3 in **panel ii**, and corresponding potential on the scale of RHE (**panel iii**). The reactively sputtered IrO_2 exhibited a lower dissolution rate than the metallic iridium similarly to thermal oxide according to **panel i**, and

46

highest activity as in **panel iii**. Its superior activity with a slower dissolution rate was consistent with the previous study,[105] and the lower dissolution rate of the thermal one likely originated from its thermodynamic stability.[106] Notably, the metallic Ir exhibited the largest amount of dissolved iridium as shown in **panel i**, and its dissolution rate as IrO_3 exponentially increased with the current density unlike the other iridium oxides (**panel ii**). They proposed that this increase was due to two dissolution-pathways prevailing at distinct potentials: Below 1.6 V vs. RHE, the iridium species likely formed $HIr^{3+}O_2$ and dissolved as Ir^{3+} via the OER catalytic cycles involving $Ir^{3+/4+/5+}$ as previously reported,[72] and above 1.6 V vs. RHE, the IrO_3 species react with water and are dissolved in the form of $Ir^{6+}O_4^{2-}$, which would not be able to be re-deposited on the catalyst surface, via the $Ir^{4+/5+/6+}$ pathway.[63] This reasoning is reflected in **Figure 2.1**; (1) dissolution of Ir^{3+} (**5** in **Figure 2.1a** and **1b**) for the pathway of **1** → **2** → **3** (or **6**) → **4** → **5**, and (2) dissolution of Ir^{6+} (**15** in **Figure 2.1d**) for the pathway through **9** → **10** → **11** → **15** or **9** → **13** → **15**).
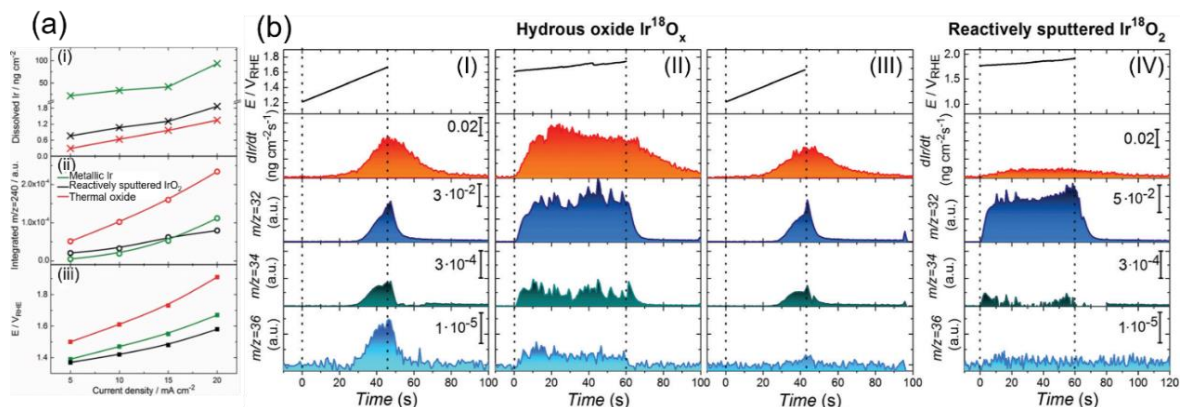
Figure 2.6. Experimental data on the dissolution of iridium oxides. (a) Results of scanning flow cell (SFC) coupled with online electrochemical mass spectrometry (OLEMS) or inductively coupled plasma mass spectrometry (ICP-MS) in 0.1 M HClO$_4$ solutions at constant current densities of 5, 10, 15, or 20 mA cm^{-2} for 30 s using three types of iridium oxide; electrochemically prepared oxide from metallic iridium (denoted as metallic Ir, green), reactively sputtered IrO$_2$ (black), and thermally prepared iridium oxide (red). (i) The amount of dissolved Ir, (ii) the amount of dissolved IrO$_3$ (m/z = 240), (iii) potential at the end of polarization on the current density. Reprinted with permission from ref. 62. Copyright (2018) Wiley-VCH. (b) Results for dissolution amount of iridium species and evolved O$_2$ gas (^{16}O^{16}O, ^{16}O^{18}O, and ^{18}O^{18}O at m/z = 32, 34, and 36, respectively) using SFC coupled with OLEMS and ICP-MS in 0.1 M HCl^{16}O$_4$ solutions; (I) using hydrous Ir^{18}O$_x$ with sweeping the potential from 1.2 V vs. RHE to the potential where the current density reached a value of 20 mA cm^{-2}; (II) using hydrous Ir^{18}O$_x$ at potentials where the current density reached 15 mA cm^{-2} for 60 s after the experiment in the panel (I); (III) using hydrous Ir^{18}O$_x$ with sweeping the potential from 1.2 V vs. RHE to the potential where the current density reached a value of 20 mA cm^{-2} after the experiment in the panel (II); and (IV) Using reactively sputtered Ir^{18}O$_2$ at potentials where the current density reached 15 mA cm^{-2} for 60 s. Reproduced from ref. 71 with permission from the Royal Society of Chemistry.

Recently, the dissolution of iridium oxide is thought to be related to the LOER mechanism[71,73] based on previous observations over various oxide surfaces.[64,107,108] Kasian et al. investigated degradation mechanism using SFC coupled with OLEMS and ICP-MS in 0.1 M HCl^{16}O$_4$ solutions.[71] They used two types of iridium oxide; electrochemically formed hydrous Ir^{18}O$_2$ catalysts, and reactively sputtered Ir^{18}O$_2$. The detected signals of evolved O$_2$ gas were composed of three distinct

species; $^{16}O^{16}O$, $^{16}O^{18}O$, and $^{18}O^{18}O$ at m/z = 32, 34, and 36, respectively.[71] **Figure 2.6b** shows the detected concentration of dissolved iridium species and evolved oxygen gas. Their experimental protocol for hydrous $Ir^{18}O_2$ was (1) sweeping the potential from 1.2 V vs. RHE to the potential where the current density reached a value of 20 mA cm^{-2} in **panel I**, then (2) applying potential where the current density reached 15 mA cm^{-2} for 60 s in **panel II**, and finally (3) sweeping the potential again from 1.2 V vs. RHE to the potential reaching 20 mA cm^{-2} in **panel III**. Critically, the dissolution of iridium species was observed in every scan. The concentration of dissolved iridium species increased with raising applied potential in the protocol (1) and (3), and the concentration almost remained constant throughout the protocol (2). Furthermore, comparison of the step (1) shown in **panel I** with the step (3) shown in **panel III** revealed that the signals of both $^{16}O^{18}O$ and $^{18}O^{18}O$ in **pane lIII** were smaller than those in **panel I**, implying that oxygen atoms in the IrO_2 participated in the OER. In contrast, their experiment using the sputtered IrO_2 provided a distinct picture. Their experimental protocol was to apply potential reaching 15 mA cm^{-2} for 60 s, the same as the step (2) of the protocol for the hydrous ones, and the obtained result is provided in **panel IV**. Interestingly, the figure disclosed a lesser signal of iridium dissolution than the hydrous one, and negligible signals of $^{16}O^{18}O$ and $^{18}O^{18}O$.[71]

In their study, Kasian et al. detailed the dissolution mechanism and lattice oxygen participation during the OER.[71] Digesting the data in **Figure 2.6b** disclosed that the ratio of the iridium dissolution rate and the $^{18}O^{18}O$ formation rate was the same for both hydrous and sputtered IrO_2, suggesting a link between the participation of lattice oxygen and the dissolution of the iridium. They subsequently studied the surface species and morphology of both samples by XPS and atom probe tomography (ATP) in conjunction with reported near ambient pressure XPS (NAP-XPS).[24,49,109] It was observed that hydrous iridium oxide possessed nanopores and -$Ir^{3+}OOH$- species, while the reactively sputtered one did not. They reasoned that the opened spaces provided by the nanopores would allow for frequent attacks by H_2O molecules, facilitating the dissolution of iridium species as Ir^{x+} (**16**) with the leaching of lattice oxygen atoms. Additionally, the Ir^{3+}-OOH species would form $HIr^{3+}O_2$ that dissolves into the solutions as Ir^{3+}.[62,72] Taken together, the dissolution was faster for the hydrous one due to its morphological and chemical state, which accompanies the removal of lattice oxygen detected as the formation of $^{16}O^{18}O$ and $^{18}O_2$, while such an event was less pronounced for the sputtered one due to the distinct surface state. These findings are reflected in the catalytic cycles described in the orange-colored cycle in **Figure 2.1d**.

2.5. Summary and Future Outlook

This chapter reviewed the recent reports on the in-situ or operando spectroscopic studies as well as advanced computational work for the OER over one of the most active catalysts, the iridium oxide. By collectively summarizing the literatures, I illustrated the OER catalytic cycles on the iridium oxide for the oxidation of both H_2O and OH^- occurring mainly at acidic and alkaline pH levels, respectively. In-situ or operando spectroscopic studies such as XPS and XANES captured the oxidation state and chemical environment of the catalysts at work, while the studies employing IR and Raman have elucidated the surface binding species in-operando. The advanced calculations addressed the kinetic aspects of the OER catalysis, refining my view at the molecular level. Notably, while shaping the scheme of the catalytic cycles, I noticed that there exists some discrepancy regarding the active site, oxidation states, surface intermediates and rds. The discrepancy likely arose from distinct experimental condition in literatures, e.g., the synthesis protocol for the iridium sample, electrolyte, applied potential, and so on. Therefore, it would be critical in the future study to comprehensively and systematically perform spectroscopic studies that can provide us with a more solid understanding of the OER catalysis. In addition, a recent study claimed that the amount of accumulated oxidative charge of electrocatalysts dictates the activation energy of the reaction, which has not been taken into account in the previous studies on the mechanism.[58] This novel concept may link the studies, which can further refine my view into the OER catalysis.

The stablished view into the reaction mechanism helps develop design principle of active and stable OER catalysts. The spectroscopic observation of Ir^{5+} state in-situ or operando[49,66,67] implies that the rds occurs on this Ir^{5+} site, plausibly Ir=O, which is thought to convert into Ir-OOH in one of the cycles.[29,46,47,69,110] This rationale suggests that stabilizing the Ir-OOH state by introducing a second component as a proton acceptor would accelerate this rds.[111] Such an approach was theoretically supported by recent DFT calculations by Busch[112] and has recently been demonstrated experimentally in the case of Mn-based catalysts.[113]

Another rational approach for improving the OER performance based on the rational understanding is the stabilization of high-valence state of iridium by introducing a second component. Furthermore, it was reviewed in this article that iridium oxide dissolves into the solutions with oxidation states of 3+ or 6+.[62,72] This finding suggests that stabilizing these oxidation states of iridium by introducing a second component would prevent the dissolution, which can prolong the lifetime of catalysts. In fact, the improved stability was reported for

IrO$_x$/SrIrO$_3$ in 2016,[114] and IrO$_x$-TiO$_2$ in 2017.[115] Thus, the rational design of catalysts based on the understanding of the reaction mechanisms would be an effective approach to improve the performance of iridium-based OER catalysts. Moreover, in such discussions of introducing additional components, the OER activity also improved by leaching the second or third component from the complex such as Sr from perovskite of SrIrO$_3$,[114] Y from pyrochlore of Y$_2$Ir$_2$O$_7$,[116] Ba and Ln from double perovskite of Ba$_2$PrIrO$_6$,[117] N and Co from Ir-based nanowire,[118] and Ni from IrNiO$_x$ core-shell structure.[119] The thus derived surface would contribute to the improvement of the OER activity by constructing highly active iridium centres such as iridium hydroxide-dominant surface.[51] This review provides the community with a generalized view into the state-of-the-art understanding of the OER mechanism over iridium, stimulating for further understanding and development of OER catalysts in the future.

2.6.   References

[1]   S. Satyapal, J. Petrovic, C. Read, G. Thomas, G. Ordaz, *Catal. Today* **2007**, *120*, 246-256.

[2]   J. Yang, A. Sudik, C. Wolverton, D. J. Siegel, *Chem. Soc. Rev*. **2010**, *39*, 656-675.

[3]   Y. Chen, C. W. Li, M. W. Kanan, *J. Am. Chem. Soc.* **2012**, *134*, 19969-19972.

[4]   K. P. Kuhl, T. Hatsukade, E. R. Cave, D. N. Abram, J. Kibsgaard, T. F. Jaramillo, *J. Am. Chem. Soc.* **2014**, *136*, 14107-14113.

[5]   K. P. Kuhl, E. R. Cave, D. N. Abram, T. F. Jaramillo, *Energy Environ. Sci*. **2012**, *5*, 7050-7059.

[6]   T. Li, Y. Cao, J. He, C. P. Berlinguette, *ACS Cent. Sci*. **2017**, *3*, 778-783.

[7]   Y. Wang, S. Gonell, U. R. Mathiyazhagan, Y. Liu, D. Wang, A. J. M. Miller, T. J. Meyer, *ACS Appl. Energy Mater.* **2019**, *2*, 97-101.

[8]   S. Garg, M. Li, A. Z. Weber, L. Ge, L. Li, V. Rudolph, G. Wang, T. E. Rufford, *J. Mater. Chem. A* **2020**, *8*, 1511-1544.

[9]   P. Rüetschi, P. Delahay, *J. Chem. Phys*. **1955**, *23*, 556-560.

[10]   A. Hickling, S. Hill, *Disc. Faraday Soc*. **1947**, *1*, 236-246.

[11]   S. Trasatti, *J. Electroanal. Chem.* **1980**, *111*, 125-131.

[12]   Y. Lee, J. Suntivich, K. J. May, E. E. Perry, Y. Shao-Horn, *J. Phys Chem Lett.* **2012**, *3*, 399-404.

[13]   C. C. L. McCrory, S. Jung, J. C. Peters, T. F. Jaramillo, *J. Am. Chem. Soc*. **2013**, *135*, 16977-16987.

[14]   S. Jung, C. C. L. McCrory, I. M. Ferrer, J. C. Peters, T. F. Jaramillo, *J. Mater. Chem. A* **2016**, *4*, 3068-3076.

[15]   J. R. Murdoch, *J. Chem. Educ*. **1981**, *58*, 32-36.

[16]   T. Shinagawa, A. T. Garcia-Esparza, K. Takanabe, *Sci. Rep*. **2015**, *5*, 13801.

[17]   H. Ooka, A. Yamaguchi, T. Takashima, K. Hashimoto, R. Nakamura, *J. Phys. Chem. C* **2017**, *121*, 17873-17881.

[18]   D. F. Abbott, D. Lebedev, K. Waltar, M. Povia, M. Nachtegaal, E. Fabbri, C. Copéret, T. J. Schmidt, *Chem. Mater*. **2016**, *28*, 6591-6604.

[19]   T. Nishimoto, T. Shinagawa, T. Naito, K. Takanabe, *J. Catal.* **2020**, *391*, 435-445.

[20]   Y. H. Hall, P. M. A. Sherwood, *J. Chem. Soc., Faraday Trans. 1* **1984**, *80*, 135-152.

[21]   R. Kötz, H. Neff, S. Stucki, *J. Electrochem. Soc*. **1984**, *131*, 72-77.

[22]   S. E. Castillo-Blum, D. T. Richens, A. G. Sykes, *Inorg. Chem*. **1989**, *28*, 954-960.

[23]   R. Kötz, H. Neff, *Surf. Sci.* **1985**, *160*, 517-530.

[24]   T. Reier, D. Teschner, T. Lunkenbein, A. Bergmann, S. Selve, R. Kraehnert, R. Schlögl, P. Strasser, *J. Electrochem. Soc*. **2014**, *161*, F876-F882.

[25]   T. Reier, Z. Pawolek, S. Cherevko, M. Bruns, T. Jones, D. Teschner, S. Selve, A. Bergmann, H. N. Nong, R. Schlögl, K. J. J. Mayrhofer, P. Strasser, *J. Am. Chem. Soc*. **2015**, *137*, 13031-13040.

[26]   I. C. Man, H.-Y. Su, F. Calle-Vallejo, H. A. Hansen, J. I. Martínez, N. G. Inoglu, J. Kitchin, T. F. Jaramillo, J. K. Nørskov, J. Rossmeisl, Universality in Oxygen Evolution Electrocatalysis on Oxide Surfaces, *ChemCatChem* **2011**, *3*, 1159-1165.

[27]   J. Rossmeisl, A. Logadottir, J. K. Nørskov, *Chem. Phys.* **2005**, *319*, 178-184.

[28]   J. J. Warren, T. A. Tronic, J. M. Mayer, *Chem. Rev.* **2010**, *110*, 6961-7001.

[29]   J. Rossmeisl, Z.-W. Qu, H. Zhu, G.-J. Kroes, J. K. Nørskov, *J. Electroanal. Chem.* **2007**, *607*, 83-89.

[30]   J. K. Norskov, T. Bligaard, B. Hvolbæk, F. Abild-Pedersen, I. Chorkendorff, C.H. Christensen, *Chem. Soc. Rev*. **2008**, *37*, 2163-2171.

[31]   M. T. M. Koper, *J. Solid State Electrochem.* **2013**, *17*, 339-344.

[32]   M. Auinger, I. Katsounaros, J. C. Meier, S. O. Klemm, P. U. Biedermann, A. A. Topalov, M. Rohwerder, K. J. J. Mayrhofer, *Phys. Chem. Chem. Phys.* **2011**, *13*, 16384-16394.

[33]   B. E. Conway, B. V. Tilak, *Electrochim. Acta* **2002**, *47*, 3571-3594.

[34]   R. Subbaraman, D. Tripkovic, K.-C. Chang, D. Strmcnik, A. P. Paulikas, P. Hirunsit, M. Chan, J. Greeley, V. Stamenkovic, N. M. Markovic, *Nat. Mater*. **2012**, *11*, 550-557.

[35]   B. E. Conway, B. V. Tilak, *Adv. Catal*. **1992**, *38*, 1-147.

[36]   T. Shinagawa, M. T.-K. Ng, K. Takanabe, *ChemSusChem* **2017**, *10*, 4155-4162.

[37]   L. Giordano, B. Han, M. Risch, W. T. Hong, R. R. Rao, K. A. Stoerzinger, Y. Shao-Horn, *Catal. Today* **2016**, *262*, 2-10.

[38]   S. Trasatti, *Electrochim. Acta* **1984**, *29*, 1503-1512.

[39]   M. T. M. Koper, *Chem. Sci*. **2013**, *4*, 2710-2723.

[40]   B. Lassalle-Kaiser, S. Gul, J. Kern, V. K. Yachandra, J. Yano, *J. Electron Spectros. Relat. Phenomena* **2017**, *221*, 18-27.

[41]   Q. Li, Y. Ouyang, S. Lu, X. Bai, Y. Zhang, L. Shi, C. Ling, J. Wang, *Chem. Commun.* **2020**, *56*, 9937-9949**.**

[42]   S. Park, Y. H. Lee, S. Choi, H. Seo, M. Y. Lee, M. Balamurugan, K. T. Nam, *Energy Environ. Sci*. **2020**, *13*, 2310-2340.

[43]   F. Dionigi, P. Strasser, *Adv. Energy Mater*. **2016**, *6*, 1600621.

[44]   J. Yu, Q. He, G. Yang, W. Zhou, Z. Shao, M. Ni, *ACS Catal.* **2019**, *9*, 9973-10011.

[45]   U. Babic, M. Suermann, F. N. Büchi, L. Gubler, T. J. Schmidt, *J. Electrochem. Soc.* **2017**, *164*, F387-F399.

[46]   Y. Ping, R. J. Nielsen, W. A. Goddard III, *J. Am. Chem. Soc.* **2017**, *139*, 149-155.

[47]   J. A. Gauthier, C. F. Dickens, L. D. Chen, A. D. Doyle, J. K. Nørskov, *J. Phys. Chem. C* **2017**, *121*, 11455-11463.

[48]   V. Pfeifer; T. E. Jones, J. J. Velasco Vélez, R. Arrigo, S. Piccinin, M, Hävecker, A. Knop-Gericke, R. Schlögl, *Chem. Sci*. **2017**, *8*, 2143-2149.

[49]   V. A. Saveleva, L. Wang, D. Teschner, T. Jones, A. S. Gago, K. A. Friedrich, S. Zafeiratos, R. Schlögl, E. R. Savinova, *J. Phys. Chem. Lett*. **2018**, *9*, 3154-3160.

[50]   V. Pfeifer, T. E. Jones, S. Wrabetz, C. Massué, J. J. V. Vélez, R. Arrigo, M. Scherzer, S. Piccinin, M. Hävecker, A. Knop-Gericke, R. Schlögl, *Chem. Sci*. **2016**, *7*, 6791-6795.

[51]   V. Pfeifer, T. E. Jones, J. J. Velasco Vélez, C. Massúe, R. Arrigo, D. Teschner, F. Girgsdies, M. Scherzer, M. T. Greiner, J. Allan, M. Hashagen, G. Weinberg, S. Piccinin, M. Hävecker, A. Knop-Gericke, R. Schlögl, *Surf. Interface Anal*. **2016**, *48*, 261-273.

[52] N. Cox, M. Retegan, F. Neese, D. A. Pantazis, A. Boussac, W. Lubitz, *Science* **2014**, *345*, 804-808.

[53] P. E. Siegbahn, *Biochim. Biophys. Acta* **2013**, *1827*, 1003-1019.

[54] W. Lubitz, E. J. Reijerse, J. Messinger, *Energy Environ. Sci.* **2008**, *1*, 15-31.

[55] J. Messinger, *Phys. Chem. Chem. Phys.* **2004**, *6*, 4764-4771.

[56] Y. Gao, T. Åkermark, J. Liu, L. Sun, B. Åkermark, *J. Am. Chem. Soc.* **2009**, *131*, 8726-8727.

[57] J. Limburg, V. A. Szalai, G. W. Brudvig, *J. Chem. Soc., Dalton Trans.* **1999**, 1353-1362.

[58] K. H. Saeed, M. Forster, J.-F. Li, L. J. Hardwick, A. J. Cowan, *Chem. Commun.* **2020**, *56*, 1129-1132.

[59] H. N. Nong, L. J. Falling, A. Bergmann, M. Klingenhof, H. P. Tran, C. Spöri, R. Mom, J. Timoshenko, G. Zichittella, A. Knop-Gericke, S. Piccinin, J. Pérez-Ramírez, B. R. Cuenya, R. Schlögl, P. Strasser, D. Teschner, T. E. Jones, *Nature* **2020**, *587*, 408-413.

[60] T. Binninger, R. Mohamed, K. Waltar, E. Fabbri, P. Levecque, R. Kotz, T. J. Schmidt, *Sci. Rep.* **2015**, *5*, 12167.

[61] X. Rong, J. Parolin, A. M. Kolpak, *ACS Catal.* **2016**, *6*, 1153-1158.

[62] O. Kasian, J.-P. Grote, S. Geiger, S. Cherevko, K. J. J. Mayrhofer, *Angew. Chem. Int. Ed.* **2018**, *57*, 2488-2491.

[63] A. Grimaud, A. DemortiHre, M. SaubanHre, W. Dachraoui, M. Duchamp, M.-L. Doublet, J.-M. Tarascon, *Nat. Energy* **2016**, *2*, 16189.

[64] A. Grimaud, O. Diaz-Morales, B. Han, W. T. Hong, Y.-L. Lee, L. Giordano, K. A. Stoerzinger, M. T. M. Koper, Y. Shao-Horn, *Nat. Chem.* **2017**, *9*, 457-465.

[65] S. Fierro, T. Nagel, H. Baltruschat, C. Comninellis, *Electrochem. Commun.* **2007**, *9*, 1969-1974.

[66] H. G. Sanchez Casalongue, M. L. Ng, S. Kaya, D. Friebel, H. Ogasawara, A. Nilsson, *Angew. Chem., Int. Ed.* **2014**, *53*, 7169-7172.

[67] A. Minguzzi, O. Lugaresi, E. Achilli, C. Locatelli, A. Vertova, P. Ghigna, S. Rondinini, *Chem. Sci.* **2014**, *5*, 3591-3597.

[68] A. Minguzzi, C. Locatelli, O. Lugaresi, E. Achilli, G. Cappelletti, M. Scavini, M. Coduri, P. Masala, B. Sacchi, A. Vertova, P. Ghigna, S. Rondinini, *ACS Catal.* **2015**, *5*, 5104-5115.

[69]   Z. Pavlovic, C. Ranjan, M. Van Gastel, R. Schlögl, *Chem. Commun.* **2017**, *53*, 12414-12417.

[70]   Z. Pavlovic, C. Ranjan, Q. Gao, M. van Gastel, R. Schlögl, *ACS Catal*. **2016**, *6*, 8098-8105.

[71]   O. Kasian, S. Geiger, T. Li, J.-P. Grote, K. Schweinar, S. Zhang, C. Scheu, D. Raabe, S. Cherevko, B. Gault, K. J. J. Mayrhofer, *Energy Environ. Sci*. **2019**, *12*, 3548-3555.

[72]   S. Cherevko, S. Geiger, O. Kasian, A. Mingers, K. J. J. Mayrhofer, *J. Electroanal. Chem*. **2016**, *774*, 102-110.

[73]   S. Geiger, O. Kasian, M. Ledendecker, E. Pizzutilo, A. M. Mingers, W. T. Fu, O. Diaz-Morales, Z. Li, T. Oellers, L. Fruchter, A. Ludwig, K. J. J. Mayrhofer, M. T. M. Koper, S. Cherevko, *Nat. Catal*. **2018**, *1*, 508-515.

[74]   K. Schweinar, B. Gault, I. Mouton, O. Kasian, *J. Phys. Chem. Lett*. **2020**, *11*, 5008-5014.

[75]   E. Willinger, C. Massué, R. Schlögl, M. G. Willinger, *J. Am. Chem. Soc.* **2017**, *139*, 12093-12101.

[76]   J. Gao, C.-Q. Xu, S.-F. Hung, W. Liu, W. Cai, Z. Zeng, C. Jia, H. M. Chen, H. Xiao, J. Li, Y. Huang, B. Liu, *J. Am. Chem. Soc.* **2019**, *141*, 3014-3023.

[77]   T. Li, O. Kasian, S. Cherevko, S. Zhang, S. Geiger, C. Scheu, P. Felfer, D. Raabe, B. Gault, K. J. J. Mayrhofer, *Nat. Catal*. **2018**, *1*, 300-305.

[78]   W. Sun, Y. Song, X. Q. Gong, L. M. Cao, J. Yang, *ACS Appl. Mater. Interfaces* **2016**, *8*, 820-826.

[79]   D. Lebedev, R. Ezhov, J. Heras-Domingo, A. Comas-Vives, N. Kaeffer, M. Willinger, X. Solans-Monfort, X. Huang, Y. Pushkar, C. Copéret, *ACS Cent. Sci*. **2020**, *6*, 1189-1198.

[80]   K. Jiang, M. Luo, M. Peng, Y. Yu, Y.-R. Lu, T.-S. Chan, P. Liu, F. M. F. de Groot, Y. Tan, *Nat. Commun.* **2020**, *11*, 2701.

[81]   Y. Zhang, C. Wu, H. Jiang, Y. Lin, H. Liu, Q. He, S. Chen, T. Duan, L. Song, *Adv. Mater*. **2018**, *30*, 1707522.

[82]   Y. Zhao, K. R. Yang, Z. Wang, X. Yan, S. Cao, Y. Ye, Q. Dong, X. Zhang, J. E. Thorne, L. Jin, K. L. Materna, A. Trimpalis, H. Bai, S. C. Fakra, X. Zhong, P. Wang, X. Pan, J. Guo, M. Flytzani-Stephanopoulos, G. W. Brudvig, V. S. Batist, D. Wang, *Proc. Natl. Acad. Sci*. **2018**, *115*, 2902-2907.

[83] S. K. Kaiser, Z. Chen, D. F. Akl, S. Mitchell, J. Pérez-Ramírez, *Chem. Rev.* **2020**, *120*, 11703-11809.

[84] S. Mitchell, J. Pérez-Ramírez, *Nat. Commun*. **2020**, *11*, 4302.

[85] W.-H. Lai, L.-F. Zhang, W.-B. Hua, S. Indris, Z.-C. Yan, Z. Hu, B. Zhang, Y. Liu, L. Wang, M. Liu, R. Liu, Y.-X. Wang, J.-Z. Wang, Z. Hu, H.-K. Liu, S.-L. Chou, S.-X. Dou, *Angew. Chem. Int. Ed*. **2019**, *58*, 11868-11873.

[86] C. F. Dickens, C. Kirk, J. K. Nørskov, *J. Phys. Chem. C* **2019**, *123*, 18960-18977.

[87] C. C. L. McCrory, S. Jung, I. M. Ferrer, S. M. Chatman, J. C. Peters, T. F. Jaramillo, *J. Am. Chem. Soc.* **2015**, *137*, 4347-4357.

[88] M. W. Kanan, D. G. Nocera, *Science* **2008**, *321*, 1072-1075.

[89] C. Costentin, D. G. Nocera, *Proc. Natl. Acad. Sci*. **2017**, *114*, 13380-13384.

[90] T. Naito, T. Shinagawa, T. Nishimoto, K. Takanabe, *ChemSusChem* **2020**, *13*, 5921-5933.

[91] H. Ooka, Y. Wang, A. Yamaguchi, M. Hatakeyama, S. Nakamura, K. Hashimoto, R. Nakamura, *Phys. Chem. Chem. Phys*. **2016**, *18*, 15199-15204.

[92] P. Steegstra, E. Ahlberg, *Electrochim. Acta* **2012**, *76*, 26-33.

[93] B. K. Mai, Y. Kim, *Inorg. Chem*. **2016**, *55*, 3844-3852.

[94] X. Yang, M.-H. Baik, *J. Am. Chem. Soc*. **2006**, *128*, 7476-7485.

[95] K. S. Exner, H. Over, *ACS Catal*. **2019**, *9*, 6755-6765.

[96] H. A. Hansen, I. C. Man, F. Studt, F. Abild-Pedersen, T. Bligaard, J. Rossmeisl, *Phys. Chem. Chem. Phys.* **2010**, *12*, 283-290.

[97] D.-Y. Kuo, J. K. Kawasaki, J. N. Nelson, J. Kloppenburg, G. Hautier, K. M. Shen, D. G. Schlom, J. Suntivich, *J. Am. Chem. Soc.* **2017**, *139*, 3473-3479.

[98] H. A. Hansen, J. Rossmeisl, J. K. Nørskov, *Phys. Chem. Chem. Phys.* **2008**, *10*, 3722-3730.

[99] K. S. Exner, J. Anton, T. Jacob, H. Over, *Electrochim. Acta* **2014**, *120*, 460-466.

[100] K. S. Exner, J. Anton, T. Jacob, H. Over, *Angew. Chem. Int. Ed*. **2014**, *53*, 11032-11035.

[101] L. G. V. Briquet, M. Sarwar, J. Mugo, G. Jones, F. Calle-Vallejo, *ChemCatChem* **2017**, *9*, 1261-1268.

[102] V. Sumaria, D. Krishnamurthy, V. Viswanathan, *ACS Catal*. **2018**, *8*, 9034-9042.

[103] K. S. Exner, I. Sohrabnejad-Eskan, H. Over, *ACS Catal*. **2018**, *8*, 1864-1879.

[104] A. Damjanovic, A. Dey, J. O. M. Bockris, *J. Electrochem. Soc.* **1966**, *113*, 739-746.

[105] G. Beni, L. M. Schiavone, J. L. Shay, W. C. Dautremont-Smith, B. S. Schneider, *Nature* **1979**, *282*, 281-283.

[106] S. Cherevko, S. Geiger, O. Kasian, N. Kulyk, J.-P. Grote, A. Savan, B. R. Shrestha, S. Merzlikin, B. Breitbach, A. Ludwig, K. J. J. Mayrhofer, *Catal. Today* **2016**, *262*, 170-180.

[107] J. Willsau, O. Wolter, J. Heitbaum, *J. Electroanal. Chem.* **1985**, *195*, 299-306.

[108] M. Wohlfahrt-Mehrens, J. Heitbaum, *J. Electroanal. Chem.* **1987**, *237*, 251-260.

[109] V. Pfeifer, T. E. Jones, J. J. Velasco Vélez, C. Massúe, M. T. Greiner, R. Arrigo, D. Teschner, F. Girgsdies, M. Scherzer, J. Allan, M. Hashagen, G. Weinberg, S. Piccinin, M. Hävecker, A. Knop-Gericke, R. Schlögl, *Phys. Chem. Chem. Phys.* **2016**, *18*, 2292-2296.

[110] J. F. Li, Y. F. Huang, Y. Ding, Z. L. Yang, S. B. Li, X. S. Zhou, F. R. Fan, W. Zhang, Z. Y. Zhou, D. Y. Wu, B. Ren, Z. L. Wang, Z. Q. Tian, *Nature* **2010**, *464*, 392-395.

[111] N. B. Halck, V. Petrykin, P. Krtil, J. Rossmeisl, *Phys. Chem. Chem. Phys.* **2014**, *16*, 13682-13688.

[112] M. Busch, *Curr. Opin. Electrochem.* **2018**, *9*, 278-284.

[113] Y. Gorlin, C.-J. Chung, J. D. Benck, D. Nordlund, L. Seitz, T.-C. Weng, D. Sokaras, B. M. Clemens, T. F. Jaramillo, *J. Am. Chem. Soc.* **2014**, *136*, 4920-4926.

[114] L. C. Seitz, C. F. Dickens, K. Nishio, Y. Hikita, J. Montoya, A. Doyle, C. Kirk, A. Vojvodic, H. Y. Hwang, J. K. Norskov, T. F. Jaramillo, *Science* **2016**, *353*, 1011-1014.

[115] E. Oakton, D. Lebedev, M. Povia, D. F. Abbott, E. Fabbri, A. Fedorov, M. Nachtegaal, C. Copéret, T. J. Schmidt, *ACS Catal.* **2017**, *7*, 2346-2352.

[116] D. Lebedev, M. Povia, K. Waltar, P. M. Abdala, I. E. Castelli, E. Fabbri, M. V. Blanco, A. Fedorov, C. Copéret, N. Marzari, T. J. Schmidt, *Chem. Mater.* **2017**, *29*, 5182-5191.

[117] O. Diaz-Morales, S. Raaijman, R. Kortlever, P. J. Kooyman, T. Wezendonk, J. Gascon, W.T. Fu, M. T. M. Koper, *Nat. Commun.* **2016**, *7*, 12363.

[118] S. M. Alia, S. Shulda, C. Ngo, S. Pylypenko, B. S. Pivovar, *ACS Catal.* **2018**, *8*, 2111-2120.

[119] H. N. Nong, T. Reier, H.-S. Oh, M. Gliech, P. Paciok, T. H. T. Vu, D. Teschner, M. Heggen, V. Petkov, R. Schlögl, T. Jones, P. Strasser, *Nat. Catal.* **2018**, *1*, 841-851.

3. Stable operation of water electrolysis in saturated phosphate buffer at neutral pH

Hydrogen production from renewable energy and ubiquitous water has a potential to achieve sustainability, although current water electrolyzers cannot compete economically with the fossil fuel-based technology. Here, I evaluate water electrolysis at pH 7 that is milder than acidic and alkaline pH counterparts and may overcome this issue. The physicochemical properties of concentrated buffer electrolytes were assessed at various temperatures and molalities for quantitative determination of losses associated with mass-transport during the water electrolysis. Subsequently, in saturated K-phosphate solutions at 80 °C and 100 °C that were found to be optimal to minimize the losses originating from mass-transport at the neutral pH, the water electrolysis performance over model electrodes of IrO_x and Pt as an anode and a cathode, respectively, was reasonably comparable with those of the extreme pH. Remarkably, this concentrated buffer solution also achieved enhanced stability, adding another merit of this electrolyte for water electrolysis.[b]

3.1. Introduction

Our future sustainable society would largely rely on the renewable energy, although the low energy density and spatiotemporal fluctuation hamper widespread implementation. The renewable energy can be converted into electricity, which then can be stored in chemical bonds via an electrocatalytic process for subsequent transport to the site of consumption.[1,2] Hydrogen has a high energy density and is a promising substance as the energy carrier.[1,3] By using water as a reactant, the electrocatalytic water splitting, i.e., water electrolysis process, yields hydrogen in a renewable way if driven by the electric power generated in a renewable manner. However, the hydrogen produced via water electrolysis in current technology fails to compete economically with fossil fuel-based counterparts,[1] which necessitates the development of a cost-effective and robust water electrolysis system.

Conventional industrial-scale water electrolyzers operates in the extremely acidic or alkaline pH conditions to maximize the overall cell efficiency by minimizing the kinetic overpotential and ohmic losses under such extreme pH conditions. The available data on the cost-breakdown of water electrolyzers indicate that the cell stack accounts for half of the capital cost of the alkaline and proton exchange membrane (PEM) water electrolyzers.[4] In more details, the half of the stack cost for the alkaline and PEM electrolyzers comprise electrocatalysts and bipolar plates, respectively.[4] I remark here that the corrosiveness of the extreme pH conditions requires the use of corrosion-tolerant materials, e.g., titanium, as the plate in the acidic media, which further increases cost. In this context, near-neutral pH aqueous medium has emerged as an alternative choice for water electrolyzers,[5-9] which is less corrosive, and offers a safer operation and broader options for materials. Such a condition is compatible with renewable energy driven systems for home use, e.g., a system that connects photovoltaic cells with an electrolyzer to store excess electricity as hydrogen that functions as a fuel for fuel cells.[5]

Significant research efforts have been dedicated to developing electrocatalysts for the half-reactions of water electrolysis, i.e., the hydrogen evolution reaction (HER) and oxygen evolution reaction (OER). In acidic and alkaline solutions, noble metals such as Pt for the HER and IrO_x and RuO_x for the OER were reported to exhibit the highest activity of water electrolysis, which sit at the top of the "volcano" trend.[10-12] To develop active yet cost-effective electrocatalysts, several electrodes composed of earth-abundant elements have been reported such as NiMo for the HER and $NiFeO_x$ for the OER.[11,13-15] When used in near-neutral pH conditions, however, these electrodes fail to catalyze the reaction at decent overpotential.[16] Previous studies using the Pt electrocatalyst

reported a HER overpotential as large as >250 mV at −4 mA cm^{-2} in solutions of 0.1 M Na$_2$SO$_4$[17] and 0.1 M NaClO$_4$.[18] at pH 7.0, which is substantially larger than 30 mV at pH 13 in the solutions of 0.1 M NaOH[17] and 0.1 M KOH.[18] Similarly, the OER overpotential at 0.1 mA cm^{-2} of α-Fe$_2$O$_3$ in 0.1 M Na$_2$SO$_4$ at pH 7.0 was >700 mV, while that in 0.1 M NaOH at pH13 was below 450 mV.[19] This poor performance reported at the near-neutral pH to those under extreme pH conditions called for research activity in this direction.

The addition of buffering species such as phosphate was found to be effective in improving the electrocatalytic performance at near-neutral pH levels.[6,21] The enhancement was accounted for by the prevention of local pH shift at the surface.[22,23] In the absence of the buffering species, the OER under the near-neutral pH conditions consumes hydroxide ions at a lower reaction rate (**Equation 3-1**), whereby the reaction switches to the oxidation of the water molecules (**Equation 3-2**), leading to a substantial acid-shift of the local pH values:[24]

$$4OH^- \rightleftharpoons O_2 + 2H_2O + 4e^-, \qquad (3\text{-}1)$$

$$2H_2O \rightleftharpoons O_2 + 4H^+ + 4e^-. \qquad (3\text{-}2)$$
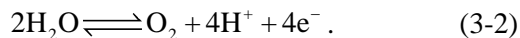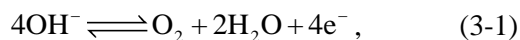
Similarly, the HER experiences reactant-switching from the proton (**Equation 3-3**) to the water molecule (**Equation 3-4**),[16,17] resulting in an alkali-shift in the proximity of the electrode surface:[23]

$$2H^+ + 2e^- \rightleftharpoons H_2, \qquad (3\text{-}3)$$

$$2H_2O + 2e^- \rightleftharpoons H_2 + 2OH^-. \qquad (3\text{-}4)$$
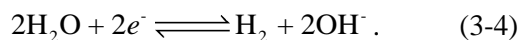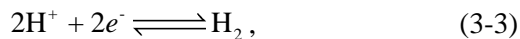
In stark contrast, when the buffering species is present, the species maintains the local pH at the electrode surface due to the buffering action:[25]

$$HA \rightleftharpoons H^+ + A^-. \qquad (3\text{-}5)$$

In other words, the presence of the buffering species prevents the formation of a concentration gradient and thus reduces the concentration overpotentials,[6] which leads to higher performance than in unbuffered conditions. Fundamentally, such buffering actions become most effective when the pH of a solution is closer to the pK$_a$ of the buffer species, where protonated and deprotonated buffer ions equally coexist, setting a primary guideline for the use of the buffer for aqueous electrocatalytic reactions.[26]

Notably, further studies on the HER and OER in buffered conditions pointed to another role of buffering species.[6,22] Targeting a reaction rate on the order of 10 mA cm^{-2}, our group previously investigated the electrocatalytic HER and OER in buffered solutions at concentrations greater than

the typical electrolyte (>0.1 M; hereafter, I use the term "concentrated" for solution more concentrated than 0.1 M).[6] Our simulation found that the proton generated via the buffering action quantitatively fails to account for the experimentally achievable HER rate depending on the pK_a of the buffering species and pH of the reaction condition.[27] Rather, we found that the buffering species most likely functions as the proton carrier and directly participates in the surface reactions.[27] Furthermore, a combined experimental and theoretical investigation in this line of study elucidated that the electrocatalytic HER rate was majorly determined by the mass-transport of the buffering species that functions as a proton carrier.[22] The optimization of electrolyte properties to maximize the mass-transport of the buffering species thus improved the electrocatalytic performance, highlighting the concept of "electrolyte engineering."[6] Further improvement in the performance, however, is retarded by the lack of a comprehensive dataset of physicochemical properties of the aqueous solutions more concentrated than 0.1 mol kg^{-1}.[28] In addition, the quantitative rationalization of such concentrated solutions still remains elusive, especially at elevated temperatures compatible with industrially relevant electrolyzer plants that would improve the mass-transport and kinetics. This gap between the available and the target hampers rational development of water electrolysis in concentrated buffer conditions. Altogether, adding buffer species to solutions at neutral pH and carefully tuning their physicochemical properties at elevating temperatures would increase the system efficiency of water electrolysis in a less corrosive environment, which would pave the way for CO_2-free hydrogen in a sustainable society.

This study herein addresses the physicochemical properties of concentrated buffer solutions to rationally pin down the optimal electrolyte for water electrolysis at neutral pH. I began with experimental measurement of the solubility, viscosity, and conductivity of concentrated phosphate solutions at various temperatures and then quantitatively analyzed losses associated with diffusion and migration events during water electrolysis. Subsequently, I investigated the water electrolysis at elevated temperatures in optimal electrolytes that minimize the losses at the neutral pH. Using a model Pt-IrO$_x$ system, my catalytic testing revealed that the concentrated buffer solution achieved performance not only comparable to—but also more stable than—extreme pH conditions. This work demonstrates the concentrated buffer solutions as a promising electrolyte for water electrolysis under neutral pH conditions.

3.2.   Experimental method

The following chemicals were used: $H_2Cl_6Pt_6 \cdot H_2O$ (99.9%, FUJIFILM Wako Pure Chemical Corporation), KOH (99.99%), H_3PO_4 (99.99%, Sigma-Aldrich), $HClO_4$ (assay 70%, Sigma-Aldrich), $Na_3IrCl_6 \cdot xH_2O$, $H_2C_2O_4$ ($\geq$ 99%, Sigma-Aldrich), $Na_2CO_3 \cdot H_2O$ ($\geq$ 99.5%, Sigma-Aldrich), H_2PtCl_6 ($\geq$ 99%, Sigma-Aldrich), HCl (37 wt% in H_2O, ACS reagent, Sigma-Aldrich), HNO_3 (69-70 wt% in H_2O, SAJ first grade, Sigma-Aldrich), KCl (99.999%, Sigma-Aldrich), $Ni(NO_3)_2 \cdot 6H_2O$ (97.0+%, FUJIFILM Wako Pure Chemical Corporation), $Fe(NO_3)_3 \cdot 9H_2O$ (99.0+%, FUJIFILM Wako Pure Chemical Corporation), and 5 mM of urea (ACS reagent, 99.0-100.5%, Sigma-Aldrich).

A variety of M-phosphate solutions (M=Li, Na, K, Cs) were employed as the electrolyte. For the preparation of 500 g of various molality of M-phosphate solutions at pH 7, 8 mol kg^{-1} H_3PO_4 solution was firstly diluted with ultrapure water (18.2 MΩ cm) under vigorous stirring to obtain approximately 300 g of the target molality of the solution. The molality in my study was determined to represent that of phosphate ions (the sum of $H_2PO_4^-$ and HPO_4^{2-}). Upon adding 7 mol kg^{-1} NaOH, KOH, CsOH, or 3 mol kg^{-1} LiOH, the pH value of the solution was adjusted to 7 by simultaneously measuring the pH using a pH meter (D-71 and 9625, HORIBA). Finally, the total weight was adjusted to 500 g by pouring ultrapure water, and the pH of the resulting solution is referenced throughout this study.

The solubility of M-phosphate was determined by observing the dissolution of salts at varying temperatures. More specifically, a sample vial was first filled to 5 ml with 4 ml of the saturated solution with a known total amount of salt. This vial was then placed in an oil-bath at the target temperature for 30 min. If the precipitates remained after 30 min, then the temperature was raised by 1 °C, and solution was left for another 30 min. This process was repeated until the precipitate disappeared. The concentration was denoted as the solubility at the final temperature.

The conductivity was accessed by measuring the solution resistance of M-phosphate solutions by electrochemical impedance spectroscopy using a 16-channel research-grade potentiostat system (VMP3, BioLogic Science Instruments) at varying molalities and temperatures. The measurement was performed in a two-electrode system with two Pt wires separated by 2.0 cm. The cell constant of my system was determined by measuring the impedance in 1.0 mol kg^{-1} KCl solution as a reference. The viscosity of M-phosphate solutions was measured with a viscometer (SVM3001, Anton Paar) at varying concentrations and temperatures.

The IrO_x electrodes were fabricated by electrochemical deposition following a reported protocol[29] with a titanium mesh substrate. The pH level of the deposition bath containing 0.4 mM of $Na_3IrCl_6 \cdot xH_2O$ and 2 mM of $H_2C_2O_4$ was adjusted to 10 by adding $Na_2CO_3 \cdot H_2O$, which was kept at 35 °C for 4 days prior to the deposition. A Ti mesh (Fuel Cell Store) with a geometric size of 1×1

cm^2 was washed by immersing in 0.1 mol kg^{-1} HCl, ultrapure water and ethanol sequentially for 5 min each. The electrochemical deposition was conducted using a three-electrode configuration with Pt mesh (Nilaco) and Hg/Hg_2Cl_2 (saturated with KCl) as the counter and reference electrodes, respectively. IrO_x was deposited onto the titanium mesh as a working electrode by immersing the mesh in the prepared deposition bath and applying a constant current density of 140 μA cm^{-2} for 14 ks. The catalytic activity of the fabricated electrodes was assessed by CV in 0.1 mol kg^{-1} $HClO_4$ to confirm the identical properties of the electrodes before catalytic testing.

In addition to IrO_x, a platinized platinum (Pt/Pt mesh) electrode was fabricated by electrochemical deposition following a reported recipe[30,31] with a Pt mesh (Nilaco) as the substrate. Prior to electrochemical deposition, the Pt mesh was washed by immersion in aqua regia for 1 min. The aqua regia was prepared by mixing HCl and HNO_3 at a volume ratio of 3:1. The mesh was then continuously washed with copious amount of ultrapure water. Subsequently, the electrochemical deposition was conducted using a three-electrode configuration with Pt mesh (Nilaco) and Hg/Hg_2Cl_2 (saturated with KCl) as the counter and reference electrodes, respectively. Platinum was deposited onto the platinum mesh as a working electrode by immersing the mesh in the prepared deposition bath and applying a constant potential of −0.1 V vs. Hg/Hg_2Cl_2 for 15 min. The catalytic activity of the fabricated electrode was assessed by CV in 0.1 mol kg^{-1} $HClO_4$ to confirm the identical properties of the electrodes before catalytic testing.

For the fabrication of the $NiFeO_x$ electrode, the hydrothermal synthesis was conducted following a reported procedure.[32] Prior to the synthesis, a Ni foam was washed as mentioned earlier by immersing the foam in 0.1 mol kg^{-1} HCl, ultrapure water, and ethanol sequentially for 5 min each. The Ni foam was then transferred together with 80 mL of solution containing 1 mM of $Ni(NO_3)_2 \cdot 6H_2O$, 1 mM of $Fe(NO_3)_3 \cdot 9H_2O$, and 5 mM of urea to a 100 mL Teflon-lined stainless-steel autoclave and heat-treated at 120 °C for 12 h. The autoclave was then naturally cooled to room temperature.

Electrocatalytic measurements were conducted using the thus fabricated IrO_x/Ti mesh anode and Pt/Pt mesh cathode in two- and three-electrode systems. Hg/Hg_2Cl_2 (saturated with KCl) was employed as a reference electrode for the measurements in the three-electrode setup. Before and during all measurements, Ar (99.9999%) or O_2 (99.9995%) gas was continuously supplied to the cell. To define the diffusion layer thickness, I did not apply stirring throughout this study. A cell with a diameter of 25 mm and a height of 50 mm (total volume of 24.5 cm^3) was employed for our testing, which was filled with electrolyte solution of 12 cm^3. In the solution, electrodes with the geometric

surface area of 10 mm × 10 mm were immersed. To minimize the evaporation of the liquid electrolyte, I introduced 550 mm long glass tubes connected to the cell, which function to reflux. The CV, chronoamperometry (CA), CP and potentiostatic electrochemical impedance spectroscopy measurements were performed at room temperature (25 °C) using the potentiostat system. The cell used in this study at elevated temperatures up to 80 °C was equipped with a jacket (Water-Jacketed glass cell; BAS Inc.), and its temperature was controlled by an external equipment (NCB-1210, Eyela). For testing above 80 °C, the temperature was controlled by placing the cell in the oil bath. All current densities are expressed in terms of the geometric electrode surface area unless otherwise noted.

The morphology of the electrode surface was characterized by scanning electron microscope (Hitachi, S-4700) at accelerating voltages of 20 kV equipped with energy dispersive x-ray spectroscopy (EDS, Horiba).

3.3.   Results and discussion

3.3.1.   Experimental determination of physicochemical properties of concentrated buffer electrolyte

Knowing that the existing PEM and alkaline electrolyzers make use of elevated temperatures of ~80 °C to optimize their efficiency,[4] I anticipate an optimum performance of near-neutral pH water electrolyzers also at elevated temperatures due to the improved kinetics[33] and mass-transport.[34] Nevertheless, limited available dataset on the physicochemical properties of buffered solutions hampers the rational optimization with respect to the temperature at near-neutral pH. This lack of data motivated me to determine the physicochemical properties of various concentrated buffer solutions in a quantitative manner.

In the present study, I limited myself to electrolyte pH conditions at neutral, i.e. pH 7 at 25 °C. I considered four criteria when choosing the buffer species: electrochemical stability, pK_a, temperature-tolerance, and solubility. As to the electrochemical stability, a buffer used as an electrolyte for water electrolysis should not irreversibly decompose. In this regard, organic substances such as citrate buffer cannot be used because they are electrochemically oxidized.[6] This criterion basically narrows the option of the buffer species suitable for my purpose to inorganic ones.[35-37] Regarding the pK_a, the buffering ions need to be in an environment in which the protonation-deprotonation reaction of the buffer is fast enough to catch up with the formation of local pH gradient. Such an ability, called the buffering capacity, becomes larger when the pH of the solution is closer to the pK_a of the buffer. Among representative inorganic buffers, the pK_a value of borate (9.2) and carbonate (10.3 for HCO_3^-/CO_3^{2-}) deviates from the benchmarking pH 7 by more than 2.2 and 3.3, respectively, while

that of phosphate is 7.2. Thirdly, although the bicarbonate solution with H_2CO_3 and HCO_3^- pair possesses a pK_a value of 6.5, the bicarbonate solutions could not be employed in an open environment employed in this study because CO_2 is released from the solution at elevated temperatures and thus the pH of the solution alkali-shifts (~pH 10). Lastly, the solubility of phosphate at 25 °C is larger than that of carbonate and borate,[28] which would allow for the more concentrated environment with high conductivity than the other buffers. These considerations pinned down phosphate as a suitable electrolyte to investigate water electrolysis at the neutral pH. I hereafter use the term M-phosphate (M=Li, Na, K, Cs) to denote the phosphate solution at pH 7 for the sake of simplicity. The anionic species in the M-phosphate solution is $H_2PO_4^-$ and HPO_4^{2-} according to the pK_a of phosphate.[28]
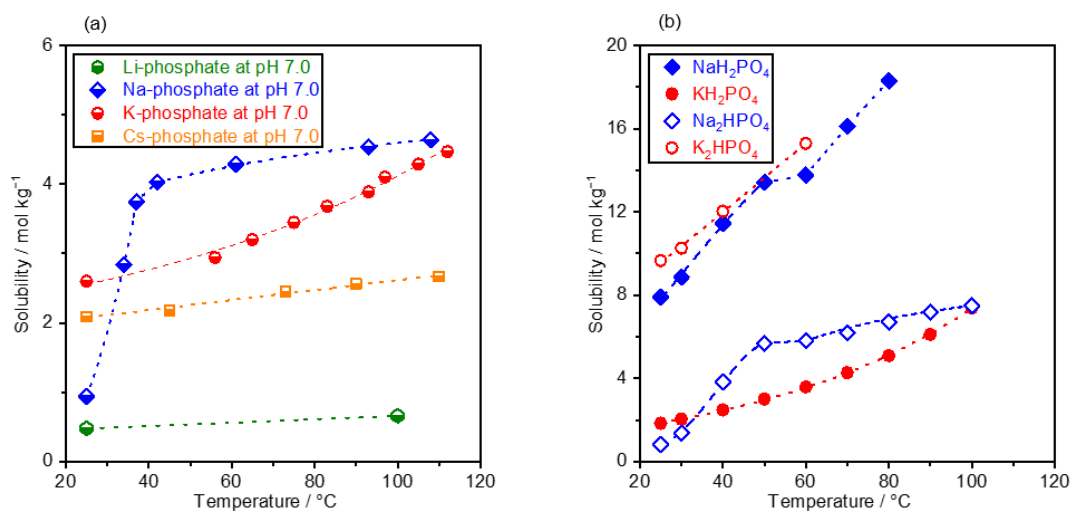
Figure 3.1. Solubility curves of phosphate solutions. (a) The solubility of M-phosphate (M=Li, Na, K, Cs) was measured at various temperatures. (b) The solubility of NaH_2PO_4, KH_2PO_4, Na_2HPO_4, and K_2HPO_4 was plotted as a function of the temperature, adopted from available dataset.[28] pH levels of solutions were adjusted to 7.0 at 25 °C prior to the measurements.

Figure 3.1a plots the measured solubilities of M-phosphate as a function of the temperature, whose pH levels were adjusted to 7 at 25 °C prior to the elevation of temperature. The boiling point elevation in the concentrated solution made possible the determination of solubility at temperatures greater than the boiling point of H_2O, and the highest achievable temperature varied with M-phosphate. Although the solubility increased with the temperature in all solutions, its sensitivity to the temperature differed depending on the identity of the cation. The Li-phosphate solution exhibited

the lowest solubility of 0.5 mol kg^{-1} at 25 °C, which slightly increased with temperature and reached 0.7 mol kg^{-1} at 100 °C. The Cs- and K-phosphate solutions showed greater solubilities of 2.1 and 2.6 mol kg^{-1} at 25 °C, respectively, which increased monotonically to 4.6 mol kg^{-1} at 108 °C and 2.7 mol kg^{-1} at 110 °C. On the other hand, the solubility of Na-phosphate solution was merely 0.9 mol kg^{-1} at 25 °C, which sharply increased to 4.0 mol kg^{-1} at 40 °C, and a further increase in temperature led to only a slight increase to the value of 4.5 mol kg^{-1} at 112 °C. This unique behavior of the Na-phosphate solution was likely due to changes in the number of hydrations with temperature:[38] e.g., the hydration number for NaH_2PO_4 was 1 below ca. 40-60 °C above which it became zero, while that of KH_2PO_4 remained zero from 0 to 100 °C.[38]

Digesting the available data on the solubility of phosphate at different pH levels helped rationalize the solubility curve observed in **Figure 3.1a**. The solubility of monobasic phosphate (NaH_2PO_4 and KH_2PO_4) and dibasic phosphate (Na_2HPO_4 and K_2HPO_4) were adopted from the literature[28] and are plotted as a function of the temperature in **Figure 3.1b**. The monobasic and dibasic phosphate are the predominant phosphate species at the weakly acidic pH of ca. pH 5 and the weakly alkaline pH of ca. 10, respectively.[28] Interestingly, Na-phosphate dissolves more than K-phosphate when monobasic, while Na-phosphate dissolves less than K-phosphate for dibasic ones. Unfortunately, there is a lack of scientific theory to fully describe the solution more concentrated than 0.1 mol kg^{-1}, which prevents rationalization of this varying solubility with identity of phosphate anions.[39] Nonetheless, I postulate that this behavior would at least in part originate from the difference of the water affinity of ions.[39-42] Generally, ions fall in categories of kosmotropes or chaotropes; kosmotropes dictate the strongly hydrated ions with smaller size and higher surface charge density while chaotropes are the weakly hydrated species.[42] The following order was obtained as Hofmeister series in which species on the left and right possess more kosmotropic and chaotropic character, respectively:[41]

$$H_2PO_4^- < HPO_4^{2-}, \qquad (3\text{-}6)$$

$$K^+ < Na^+. \qquad (3\text{-}7)$$

Oppositely charged ions with similar water affinity tend to associate with each other, leading to a smaller mean activity coefficient and fewer dissolved ions, while the opposite is true for ion pairs with dissimilar water affinities.[42] According to this rule, K^+ interacts with $H_2PO_4^-$ more strongly than Na^+ likely indicating lower solubility of KH_2PO_4 than NaH_2PO_4. Likewise, Na^+ would associate more with HPO_4^{2-} than K^+, possibly resulting in higher solubility of K_2HPO_4 than Na_2HPO_4. Interestingly, this order of predicted solubilities of both monobasic and dibasic phosphate solutions agrees with **Figure 3.1b**, likely validating the view from water affinity in rationalizing the solubility of

concentrated buffer solutions. In terms of phosphate solutions at pH 7, in which both $H_2PO_4^-$ and HPO_4^{2-} coexist, interactions among M^+, $H_2PO_4^-$, and HPO_4^{2-} are all at play. The complexity might have resulted in the non-straightforward order of $Li^+ < Cs^+ < K^+ < Na^+$ at neutral pH in **Figure 3.1a**. The hard and soft acids and bases (HSAB) theory[43] would be another rationale for the solubility behavior. Hard acids bind strongly to hard bases, and soft acids bind strongly to soft bases.[43,44] Generally, harder acids tend to have a small positive charge, be large in size, have several easily excited outer electrons, and are polarizable.[43,44] In addition, harder bases tend to have high electronegativity, be hard to reduce, be associated with empty orbitals of high energy, and have low polarizability. The order of hard base (or hard acid) is the same as the order of chaotropic character dictated in **Equation 3-6** (or **Equation 3-7**)[45], suggesting the same conclusion discussed above in Hofmeister series. Knowing that K-, Na-, and Cs-phosphate solutions have higher solubility than Li-phosphate by one order of magnitude, I focus hereafter on these three phosphate solutions that allow for the investigation of a wide range of the molality values.

Before describing the diffusion event, I first address the theoretical description of mass-transport to elucidate the key parameter governing the phenomena in the solution. In general, mass-transport comprises the diffusion, the migration, and the convection,[6] which are theoretically expressed by the Nernst-Planck equation:

$$J_i(x) = -D_i \frac{\partial c(x)}{\partial x} - \frac{z_i F}{RT} D_i c \frac{\partial f(x)}{\partial x} - cv(x), \qquad (3\text{-}8)$$

in which J is the flux, D is the diffusion coefficient, c is the concentration of the solution, z is the charge number, F is the Faraday constant, and v is the velocity of the forces in the solution.[27] The first, second, and third terms on the right side of **Equation 3-8** denote the diffusion, migration, and convection, respectively. This expression clearly shows that both the diffusion and migration are a function of the diffusion coefficient, which largely determines the overall mass-transport flux.

With this formula in mind, I subsequently studied the diffusion coefficient. The diffusion coefficient of each ion D_i is theoretically described by the following equation in the framework of the Stokes-Einstein model,[6] without considering the solute-solvent and solute-solute interactions:[46]

$$D_i = \frac{kT}{3\pi d_i \mu_i}, \qquad (3\text{-}9)$$

in which, k is the Boltzmann constant, d denotes the Stokes diameter (effective diameter of the hydrated ion), and μ represents the viscosity of the solution. The diffusion coefficient in part governs the conductivity σ of the electrolyte:[47]

$$\sigma = \frac{F^2 z^2}{RT} \sum c_i D_i \ .$$
(3-10)

Based on these relationships, below the viscosity and the conductivity of Na-, K-, and Cs-phosphate solutions were measured and discussed.

Figure 3.2 summarizes the measured viscosity of Na-, K-, and Cs-phosphate solutions at various temperatures. Because excessively large molalities make the difference in the viscosity among various M-phosphate solutions visibly smaller, I tentatively chose the molality of 2.0 mol kg^{-1} as the representative (see Table 3.1 for full dataset of viscosity at various molalities and temperatures). Viscosity of the 2.0 mol kg^{-1} Na-phosphate solution below 40 °C could not be measured because of its solubility. Regardless of the identity of the cations, the viscosity decreased with elevating temperatures, consistent with the previously reported empirical law.[34,48] Comparing the viscosity of M-phosphate solutions revealed that the viscosity of K-phosphate was the smallest, followed by Cs$^+$ and Na$^+$ at 60 °C and lower:

$\qquad$ K$^+$ < Cs$^+$ < Na$^+$. $\qquad\qquad\qquad$ (3-11)

Table 3.1. Viscosity of phosphate solutions at the neutral pH. Viscosity of Na-, K-, and Cs-phosphate solutions was measured at various temperatures using a viscometer, and pH levels of solutions were adjusted to 7.0 at 25 °C prior to the measurements.

		Viscosity / mPa s								
	Molality / mol kg^{-1}	25 °C	30 °C	40 °C	50 °C	60 °C	70 °C	80 °C	90 °C	100 °C
	0.05	0.87								
	0.10	0.91	0.81	0.66	0.55	0.47				
	0.20	0.90								
Na-phos.	0.30	1.01								
	0.40	1.06								
	0.50	1.10								
	0.60	1.24								
	0.75	1.36								

	0.90	1.60	1.43	1.15	0.95	0.80				
	1.80		2.90	2.22	1.78	1.46				
	2.00			3.62	2.71	2.13	1.75	1.57	1.31	1.14
	2.50			4.69	3.52	2.74	2.21			
	4.60									7.92
K-phos.	0.10	0.91								
	0.20	1.04								
	0.50	0.95	0.86	0.69	0.56	0.49				
	0.75	1.14								
	0.90	1.27	1.14	0.94	0.79	0.67				
	1.25	1.64								
	1.50	1.87	1.67	1.37	1.14	0.98				
	1.70	1.98	1.78	1.46	1.22	1.04				
	2.00	2.52	2.27	1.89	1.52	1.28	1.09	0.99	0.85	0.8
	2.80	3.84	3.42	2.72	2.24	1.87				
	3.70				4.98	4.06	3.39	2.88	2.46	2.14
	4.10									2.88
Cs-phos.	0.1	0.95								
	0.25	0.92								
	0.33	1.02								
	0.50	0.93	0.83	0.68	0.67	0.55				
	0.75	1.14								
	1.00	1.32								
	1.40	1.86	1.68	1.40	1.18	1.02				
	1.70	2.45	2.14	1.84	1.53	1.31				

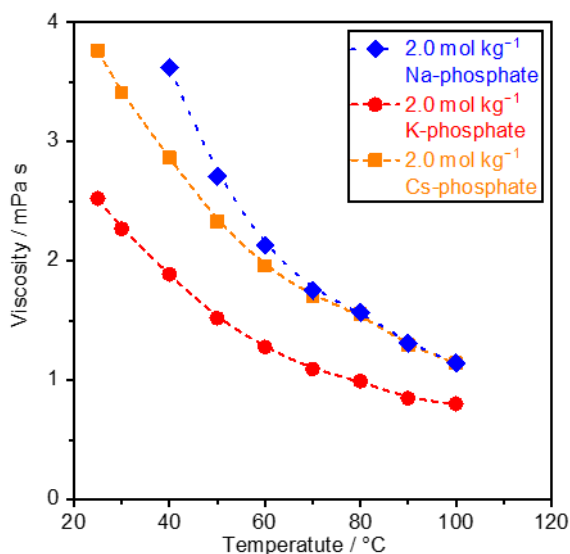|									
2.00	3.76	3.41	2.86	2.33	1.96	1.70	1.55	1.29	1.14
2.20	4.39	3.96	3.23	2.70	2.26				

Figure 3.2. Viscosity of phosphate solutions at the neutral pH. The viscosity of Na-, K-, and Cs-phosphate solutions was measured at various temperatures using a viscometer, and pH levels of solutions were adjusted to 7.0 at 25 °C prior to the measurements. The dotted lines are provided as a visual aid. See **Table 3.1** for the complete data at different molalities and temperatures.

However, the viscosities of Na- and Cs-phosphate solutions became identical above 60 °C. To shed light on this transition, the logarithm of viscosity was plotted as a function of reciprocal of the temperature in **Figure 3.3**, [34,48] as in the Arrhenius expression. The Na-phosphate solution at >60 °C as well as the K- and Cs-phosphate solutions across the entire temperature regime exhibited identical slopes. In contrast, the slope value for the Na-phosphate solution below 60 °C was greater than these values, consistent with the transition in the viscosity-temperature relationship for the Na-phosphate solutions. The origin of this unique behavior for Na-phosphate remains unclear at this stage; however, I may postulate that it might have originated from the change of the hydration number for Na-phosphate solution at varying temperatures as discussed in **Figure 3.1**. The hydration number of both NaH_2PO_4 and Na_2HPO_4 decreases at higher temperatures,[38] and thus the hydrated size of Na-phosphate becomes smaller with increasing temperature. The larger phosphate sizes at lower

temperatures would hinder the motion of the species, which anticipates a higher sensitivity to the temperature in the lower temperature regime. All in all, since **Equation 3-9** states that the diffusion coefficient is proportional to the reciprocal of the viscosity, the observed lower viscosity of K-phosphate indicated a larger diffusion flux of phosphate species in the K-phosphate solution than that in the Na- and Cs-phosphate solutions. Nevertheless, the viscosity of K-phosphate solution at this molality was found to be substantially larger than 2.2 mPa s of industrially relevant solutions of 7.0 mol kg^{-1} KOH solution at 25 °C.[28]
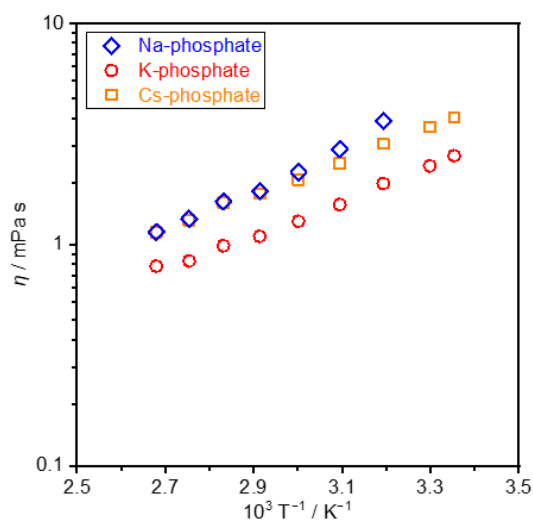
Figure 3.3. The Arrhenius type plot of viscosity in 2.0 mol kg^{-1} M-phosphate (M=Na, K and Cs) solutions. Viscosity of the Na-, K-, and Cs-phosphate solutions was measured using a viscometer, and is plotted as a function of the reciprocal of the temperature. pH levels of the phosphate solutions were adjusted to 7.0 at 25 °C prior to the measurements.

With increasing molality, the viscosity increased in all phosphate solutions at neutral pH (see **Table 3.1** and **Figures 3.4a** and **3.5**). This viscosity-molality relationship was consistent with the expression below that is applicable at lower molalities (<0.1 mol kg^{-1}):[49-51]

$$\eta_r = \frac{\eta}{\eta_0} = 1 + Am^{1/2} + Bm + Dm^2, \qquad (3\text{-}12)$$

in which, η_r is relative viscosity, η is viscosity of solution, η_0 is viscosity of solvent, and m is molality. The A-coefficient is determined by ion-ion electrostatic interaction,[50] the B-coefficient is an

adjustable parameter which is related to the size of the ions, and the D-coefficient is likely related to solute–solute association effects.[49] Applying this equation to the concentrated buffer sheds lights on their properties. The A-coefficient was calculated from the ionic attraction theory by the Falkenhagen-Vernon equation;[49,51]

$$A = 0.7536 \left[\frac{\lambda_1^0 + \lambda_2^0}{4\lambda_1^0 \lambda_2^0} - \frac{(\lambda_1^0 - \lambda_2^0)^2}{4.41\lambda_1^0 + \lambda_2^0(\lambda_1^0 + \lambda_2^0)} \right], \qquad (3\text{-}13)$$

In which λ is limiting equivalent conductance. The A-coefficient value is obtainable only at 25 °C because of limited availability of the dataset.[28] By fitting the experimental data with **Equation 3-12** using the thus determined A-coefficient, the B and D-coefficients at 25 °C were determined[49] and listed in **Table 3.2**. At 25 °C, all values of A, B and C in Na-phosphate were larger than that of K and Cs-phosphate, presumably reflecting the strong electrostatic interaction of ions in the Na-phosphate solution, the larger hydrated radius of the Na^+ ion of 3.58 Å versus 3.31 Å of the K^+ ion and 3.29 Å of the Cs^+ ion,[52] and stronger solute-solute association effects. These properties of the Na-phosphate solution anticipate its larger viscosities than the K- and Cs-phosphate solutions, consistent with the measured results in **Figure 3.2** and **Table 3.1** at 25 °C.
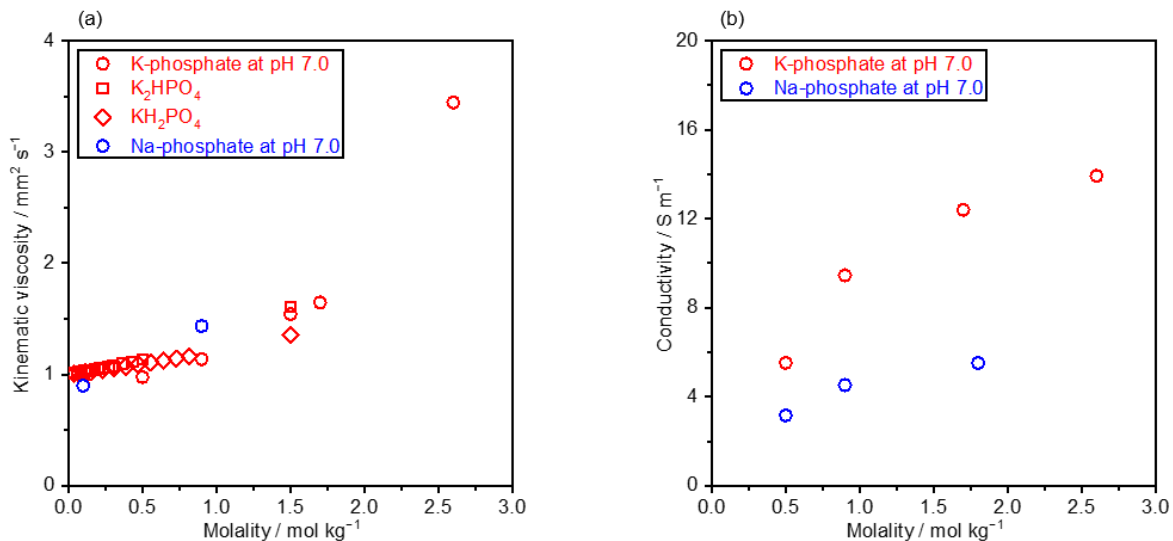
Figure 3.4. Physicochemical properties of K- and Na-phosphate as a function of concentration. (a) Viscosity of the K- and Na-phosphate solutions was measured at 25 °C using a viscometer. Viscosity of KH_2PO_4 and K_2HPO_4 solutions were adopted from the literature.[28] (b) Conductivity of the K-phosphate solutions at 25 °C and Na-phosphate solutions at 30 °C were plotted as a function of molality and assessed by impedance conducted in the 2-electrode system using two Pt wires while keeping the distance between Pt wires at 2.0 cm (cell constant, K_{cell} = 0.6 cm^{-1}). In both panels, the pH levels of solutions were adjusted to 7.0 at 25 °C prior to the measurements.

Figure 3.5. The parameter η_r $(= \eta / \eta_0)$ as a function of molality of Na-, K-, and Cs-phosphate solutions at 25 °C. Viscosity of the Na-, K-, and Cs-phosphate solutions was measured at 25 °C using a viscometer. pH levels of the phosphate solutions were adjusted to 7.0 at 25 °C prior to the measurements.
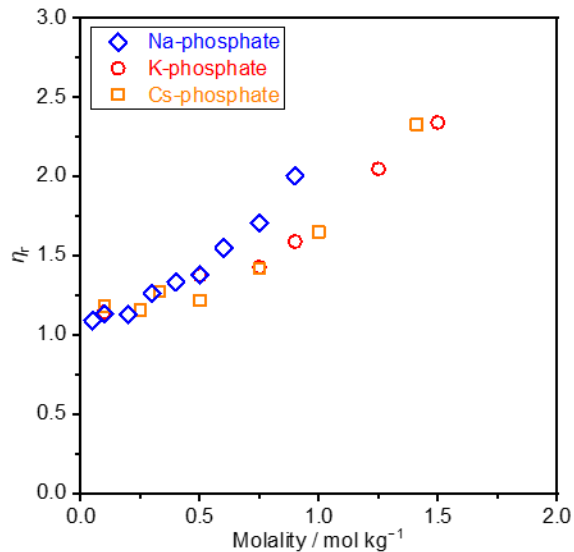
Table 3.2. The values of A-, B-, and D-coefficient at 25 °C. A-coefficient calculated with **Equation 3-13**.[28,49] B- and D- coefficient obtained by fitting the experimental data with **Equation 3-12**.

	A-coefficient / 10^4 m^{-2} S^{-1} mol	B-coefficient / mol^{-1} kg	D-coefficient / mol^{-2} kg^2
Na-	7.8	0.21	0.80
K-	6.3	0.17	0.37
Cs	6.1	0.18	0.70

The measured conductivity of the K-phosphate solutions at various molalities was plotted as a function of the temperature in **Figure 3.6** together with experimentally determined values of saturated Na-phosphate as well as the reported values of KOH[53] as a reference. The figure revealed that the conductivity increased with temperature and molality. The following expression obtained from **Equations 3-9** and **3-10** helped rationalize the dependence of the conductivity on the temperature:

$$\sigma = \frac{z^2 ec F}{3\pi d\mu},$$ (3-14)

in which e denotes the elementary charge. Primarily, the conductivity was proportional to the inverse of the viscosity. Since **Figure 3.2** showed a decreasing viscosity with temperature, the increase in conductivity with temperature shown in **Figure 3.6** agrees with **Equation 3-14**.

With increasing molality, the conductivity of both K-phosphate (**Figure 3.6**) and Na-phosphate (**Figure 3.4a**) solutions monotonically increased, which is consistent with the previous report on K_2HPO_4.[54] However, one may wonder about the absence of conductivity maxima in the conductivity-molality relationship, which was previously observed for KH_2PO_4[54] and KOH.[53] This apparent dissimilarity was accounted for by the viscosity-molality relationship. More precisely, **Equation 3-14** predicts that at a given temperature, the conductivity is a function of the molality and the kinematic viscosity as variables in the present condition. The dynamic viscosity of solutions increased with molality as discussed (**Figure 3.4b**); however, the extent of the increase differed depending on the identity of ions. At a given molality, K_2HPO_4 exhibited a higher viscosity than KH_2PO_4. Interestingly, the K-phosphate possessed a viscosity value in-between K_2HPO_4 and KH_2PO_4 at the molality of my interest, e.g., 1.5 mol kg^{-1}. Such a larger increase of the viscosity for the K_2HPO_4 would lower its conductivity at higher molality, leading to the appearance of a conductivity maximum at a lower molality in the conductivity-molality relationship. In contrast, the relatively smaller increase in the viscosity for KH_2PO_4 and K-phosphate solutions shifted their conductivity maximum to appear at higher molalities, which was likely greater than their solubility, resulting in an apparently monotonic increase in the conductivity with molality in experiments.
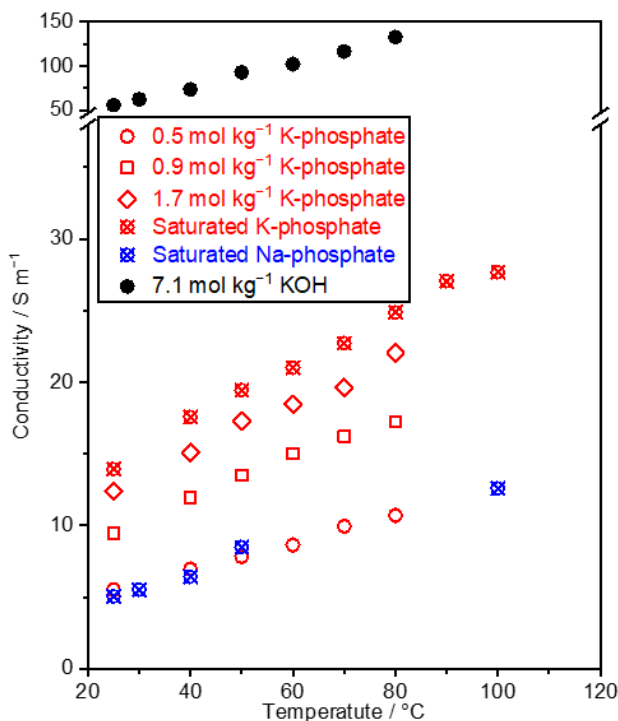
Figure 3.6. Conductivity of K-phosphate solutions. Conductivity of the phosphate solutions was assessed by measuring impedance, which was conducted in the 2-electrode system using two Pt wires, while keeping the distance between Pt wires at 2.0 cm (cell constant, K_{cell} = 0.6 cm^{-1}). The concentration of saturated K-phosphate was 2.6, 2.8, 2.9, 3.1, 3.3, 3.6, 3.8, and 4.1 mol kg^{-1} at 25, 40, 50, 60, 70, 80, 90, and 100 °C, respectively, and that of saturated Na-phosphate was 0.9, 1.8, 3.9, 4.1, 4.6 mol kg^{-1}, respectively, at 25, 30, 40, 50, and 100 °C. The values of KOH were adopted from the literature.[53] The pH levels of the phosphate solutions were adjusted to 7.0 at 25 °C prior to the measurements.

These variations of the viscosity, and in turn those of the conductivity, with different types of phosphate anions would be rationalized by their distinct sizes. A previous study suggested that the smaller ions would interact more strongly with water molecules and ionic species.[55] Accordingly, the mobility of the solution containing smaller ions is lower, making its viscosity large.[55] The ionic size of HPO_4^{2-} is 2.30 Å, which is smaller than 2.38 Å for $H_2PO_4^-$.[56] Thus, the viscosity of solution with HPO_4^{2-} is anticipated to be larger than that with $H_2PO_4^-$ solutions, consistent with the experimental observation (**Figure 3.4b**). The fact that the viscosity of K-phosphate appeared to be

between the value of KH_2PO_4 and K_2HPO_4 indicates the absence of complex interactions between the anionic species impacting the viscosity.

The variation in the viscosity and the conductivity for different cations likely arose also because of distinct effective ion sizes in the hydrated form. Specifically, previous studies suggested that the alkali metal ion interacts more with the surrounding ion as the hydrated ion size along alkali metal increases, which results in the increase of the viscosity.[42,57] Given that the Na^+ ion has a larger hydrated radius of 3.58 Å than 3.31 Å of the K^+ ion and 3.29 Å of the Cs^+ ion,[52] this suggestion is consistent with the larger viscosity of the Na-phosphate than the K- and Cs-phosphate solutions in **Figure 3.2**. In addition, the larger effective size and the viscosity of Na^+ would likely lead to smaller conductivity according to **Equation 3-14**, which agrees with the conductivity shown in **Figure 3.6** measured in solutions more concentrated than 0.1 mol kg^{-1}.

Finally, I remark on the applicability of existing theory for the dilute solution to solutions more concentrated than 0.1 mol kg^{-1} in this current work. The concentration described in **Equations 3-9**, **3-10**, and **3-14** is a nominal one and might deviate from the effective concentrations when the molality is greater than 0.1 mol kg^{-1} because of the decrease in the mean activity coefficient.[34,39] In addition, the effective ion size is a direct function of the hydration number, which would vary with the molality as well.[52,58] Nevertheless, among the phosphate solutions investigated in **Figure 3.2** and **Figure 3.6**, a higher conductivity was observed for solutions with smaller viscosities, indicating that the variation in the mean activity coefficient and the number of hydration were quantitatively smaller than that of viscosity, which makes viscosity be a primary parameter impacting mass-transport. In fact, the conductivity calculated with **Equation 3-14** using the measured viscosity quantitatively agrees with the experimentally obtained values (**Figure 3.7**), which demonstrate the validity and applicability of the employed equation and model in the conditions considered in the present study. Overall, I focused on K-phosphate solution from this point on as a representative solute that demonstrated higher solubility, smaller viscosity, and larger conductivity among *M*-phosphates at pH 7, which all would anticipate a greater mass-transport flux and in turn improved catalytic performance for water electrolysis.
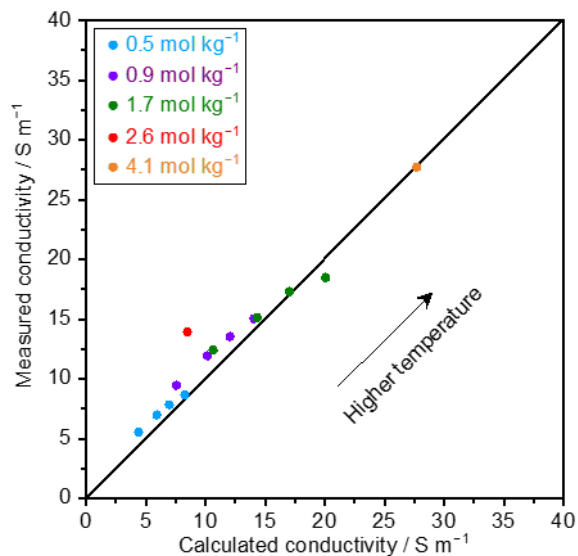
Figure 3.7. Comparison of experimentally obtained and calculated conductivity. The experimentally observed conductivity was compared with the value derived from calculations for various K-phosphate solutions at molalities of 0.5, 0.9, and 1.7 mol kg^{-1} at varying temperatures of 25, 40, 50 and 60 °C as well as 2.6 mol kg^{-1} and 4.1 mol kg^{-1} K-phosphate at temperatures of 25 and 100 °C. Conductivity was experimentally measured by impedance spectroscopy, which was conducted in the two-electrode system using two Pt wires while keeping the distance between Pt wires at 2.0 cm (cell constant, K$_{cell}$ =0.6 cm^{-1}). The calculated conductivity was obtained by using Stokes-Einstein equation.

3.3.2. Quantitative analysis of losses due to the mass-transport during water electrolysis

Here, I address the mass-transport flux of phosphate species in the K-phosphate solutions using the measured quantities in the previous section. I determine the ohmic loss and concentration overpotential originating from the flux of migration and diffusion, respectively. In the analysis below, calculations were performed at an electrode distance of 0.5 mm, which is the same as that in the alkaline electrolyzer of zero-gap configuration,[59,60] and on the same order as the thickness of typical membrane used in conventional PEM electrolyzer (0.1 mm).[61]

By definition, the ohmic loss, or iR loss, is described by the following equation:

$$R = \frac{1}{\sigma} \times \frac{l}{A} = \frac{K_{cell}}{\sigma}, \qquad (3\text{-}15)$$

in which l and A are the specific length and cross-sectional area of the electrochemical cell, respectively,[47] and l/A is called the cell constant K_{cell}. Together with **Equation 3-14**, I obtain:

$$iR_{loss} = i \times R = i \times K_{cell} \frac{3\pi d\mu}{z^2 ec F}, \qquad (3\text{-}16)$$

in which i is the electric current. The quantitative determination of the iR-loss thus requires a quantity of K_{cell}, which was set to be 0.2 cm^{-1} as determined by the previously reported relationship between K_{cell} and electrode-gap.[62]

Regarding the diffusion contribution, I consider a hypothetical extreme condition, in which the diffusion of phosphate species governs the reaction rate and directly participates in the surface reactions[6,22,27] as the diffusion-limited condition. The diffusion flux is converted to the concentration overpotential[63] that represents an overpotential originating from a concentration gradient. Therefore, the obtained concentration overpotential is the theoretically attainable maximum. In an equation, the concentration overpotential is derived by:[63]

$$\eta_{Concentration} = \frac{RT}{nF} \ln \frac{C_b}{C_s}, \qquad (3\text{-}17)$$

in which n is the number of electrons transferred per unit overall reaction, C_b is the concentration in the bulk of electrolyte, and C_s is the concentration at the surface of electrode. The diffusion-limited current density is described as follows:

$$j = nF J_{diffusion} = -nFD \frac{C_b - C_s}{\partial x}. \qquad (3\text{-}18)$$

Combing **Equations 3-17** and **3-18** yields the following formulate:

$$\eta_{\text{Concentration}} = \frac{\text{R}T}{n\text{F}} \ln \frac{C_b}{C_b + \frac{j}{n\text{F}D}\partial x} .\qquad (3\text{-}19)$$
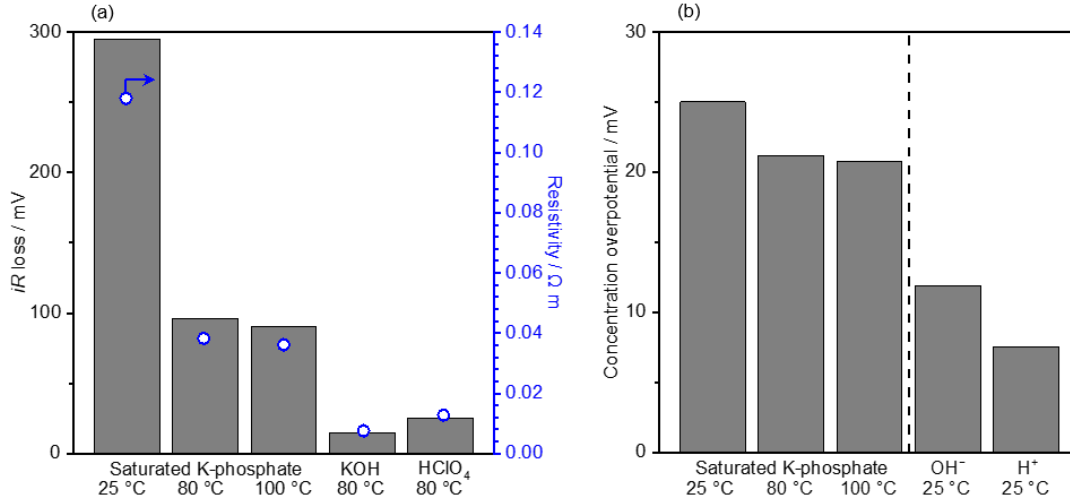

Figure 3.8. Analysis of voltage losses due to the mass-transport at 100 mA cm^{-2}. (a) *iR* loss was obtained by multiplying the resistivity of the solution by the cell constants. The resistivity was accessed by impedance spectroscopy, which was conducted in the 2-electrode system using two Pt wires while keeping the distance between Pt wires at 2.0 cm (cell constant, K_{cell} = 0.6 cm^{-1}) in K-phosphate (pH 7.0) of 2.6 mol kg^{-1} at 25 °C, 3.5 mol kg^{-1} at 80 °C and 4.1 mol kg^{-1} at 100 °C as well as 7.0 mol kg^{-1} HClO$_4$ at 80 °C. The value of 7.1 mol kg^{-1} KOH was adopted from literature.[53] The cell constant at a distance of 0.5 mm between electrodes were extrapolated from the previously reported values,[62] which corresponded to 0.2 cm^{-1}. The surface area of the electrode was 1.0 cm^2. (b) Concentration overpotential, or Nernstian loss, was calculated in a condition of complete depletion of the reactant at the electrode surfaces. Conditions: current density =100 mA cm^{-2}, the surface area of electrode = 1.0 cm^2, and diffusion layer thickness of = 0.5 mm in K-phosphate (pH 7.0) of 2.6 mol kg^{-1} at 25 °C, 3.5 mol kg^{-1} at 80 °C and 4.1 mol kg^{-1} at 100 °C, and in 1.0 mol kg^{-1} OH^{-1} and 1.0 mol kg^{-1} H$^+$.

The *iR*-loss and the concentration overpotential were computed using **Equations 3-16** and **3-19**, respectively, at 100 mA cm^{-2} for electrodes in size of 1 cm^2 and shown in **Figure 3.8**. **Figure 3.8a** summarizes the calculated values of *iR* loss in K-phosphate solutions of 2.6 mol kg^{-1} at 25 °C, 3.5 mol kg^{-1} at 80 °C and 4.1 mol kg^{-1} at 100 °C, which are the saturated solution at each temperature.

The saturated solution was chosen as the model here because the smaller viscosity and in turn larger diffusion coefficient were anticipated at the higher molality. I also show the iR losses of 7.0 mol kg^{-1} KOH and 7.0 mol kg^{-1} HClO$_4$ at 80 °C for comparison as representative alkaline and acidic solutions, respectively. In the figure, the phosphate solution exhibited an iR loss as high as $>$ 150 mV at 25 °C, which substantially decreased to ca. 50 mV at elevated temperatures. However, this value was still inferior to that in the 7.0 mol kg^{-1} KOH solution at 80 °C. Likewise, the value of resistivity in the saturated K-phosphate solutions decreased with elevating temperatures and reached a value of 0.04 Ω m at 100 °C that was still larger than 0.0075 Ω m of the 7.0 mol kg^{-1} KOH solution at 80 °C. This larger resistivity and in turn the iR-losses could be regarded as the limitation of saturated K-phosphate solution compared with the extreme pH counterparts.

I remark here that the practical operation would require the use of membrane or diaphragm for separation of gases, and their resistivity adds losses to the system.[61,64] The Zirfon® diaphragm filled with 30 w% KOH solution and Nafion® membrane (also functioning as solid electrolyte) are used in conventional alkaline and PEM electrolyzers, respectively, whose corresponding resistivities were 0.06 Ω m and 0.09 Ω m.[61,65,66] Consequently, this value of 0.06 Ω m for the diaphragm filled with electrolyte becomes responsible for the iR loss in the alkaline electrolyzer, corresponding to the iR loss of 120 mV. The additional use of the diaphragm would also add a resistivity of ca. 0.06 Ω m in the K-phosphate solution, making the total resistivity amount to approximately 0.1 Ω m. Nevertheless, we argue that the use of the diaphragm could be omitted in concentrated buffer conditions due to the small solubility and diffusion coefficient of gases as well as increased viscosity of the solutions, which all lead to lessened gas crossover as demonstrated previously.[54]

Figure 3.8b compiled the calculated values of concentration overpotential. The concentration overpotential in K-phosphate solutions decreased with increasing the temperature from 25 mV at 25 °C to 21 mV at 100 °C. The figure contained the concentration overpotential in the hypothetical acidic and alkaline conditions of only 1.0 mol kg^{-1} H$^+$ and OH$^-$ at 25 °C as a reference due to the lack of available diffusion coefficient of these ions at high temperature and high molalities.[28] Comparing these values revealed that the concentration overpotential in K-phosphate was larger than 8 and 12 mV of the acidic and alkaline representatives, respectively. Importantly, I remember here that the concentration overpotential considered herein was the theoretically attainable maximum, in which the reactant (phosphate, proton, and the hydroxide ion) was completely depleted at the surface. In addition, the concentration overpotential in **Figure 3.8b** was quantitatively smaller than the iR loss in **Figure 3.8a** by one order of magnitude. Therefore, the loss in the electrolysis system using those

electrolytes would majorly originates from the migration of ions. Lastly, this quantitatively small concentration overpotential was in line with a previous study,[67] which demonstrated that optimization of the electrolyte properties to maximize the mass-transport flux would result in an improved overall performance. According to **Equation 3-9**, the diffusion coefficient was proportional to the temperature and reciprocal of the viscosity. The elevation of the temperature resulted in a decrease in the viscosity (**Figure 3.2**), which lead to an increase in diffusion coefficient. Thus, the mass-transport flux was enlarged, and in turn the concentration overpotential became smaller as demonstrated herein. All things considered, concentrated K-phosphate solution at elevated temperature is potentially an effective electrolyte for water electrolysis at the neutral pH among *M*-phosphate solutions investigated.

3.3.3. Demonstration of water electrolysis in concentrated buffer solutions at neutral pH

This study thus far indicated the concentrated K-phosphate solutions as promising electrolyte, and I now perform catalytic testing of water electrolysis in this electrolyte solution. Chronopotentiometry (CP) was conducted at 10 mA cm^{-2} and 80 °C in K-phosphate solution as well as HClO$_4$ and KOH solutions as references, using model Pt/Pt mesh and IrO$_x$/Ti mesh electrodes as the cathode and the anode, respectively (see **Figures 3.9**-**3.11** for surface morphologies). The obtained *iR*-free voltages are shown in **Figures 3.15a** and **3.15b** (see **Figure 3.12** for the performance without *iR*-correction). The CP profiles in 7.0 mol kg^{-1} HClO$_4$, KOH, and 3.5 mol kg^{-1} K-phosphate displayed in **Figure 3.3.** were averaged for the two independent experiments (see **Figure 3.S13** for raw data). The *iR*-corrected voltage increased with time in acidic and alkaline electrolyte solutions (**Figure 3.15a**), although the extent of the increment depended on the electrolyte identity and molality. In 0.1 mol kg^{-1} HClO$_4$ and KOH, the initial voltage of 1.40 V increased to 1.56 V and >2.0 V, respectively, after testing for 6 h. The more concentrated solutions shown in **Figure 3.15b** were employed to mimic the harsh environment of industrial electrolyzer, and the initial voltage was as small as 1.24 V for HClO$_4$ that rapidly increased with time to reach > 2.0 V, while that at alkaline pH was 1.30 V, which also increased with time and ended at >1.60 V. No apparent losses in the performance was observed at the cathode for these experiments, and hence the increase in the overall voltage was most likely accounted for by the degradation of IrO$_x$ as investigated recently.[11,68,69] In fact, the voltages using the IrO$_x$/Ti mesh-Pt/Pt mesh eventually matched those using bare Ti mesh-Pt/Pt mesh in KOH solutions (**Figure 3.14**), suggesting that the dissolution of iridium was responsible for the increase in the overall voltage with time. Notably, such a rapid degradation of iridium was not anticipated in the acidic medium,

given that the lifetime of PEM electrolyzer using an IrO_x anode was around 60,000 hours.[70] This shorter lifetime in the present study might have originated from the different circumstance, e.g., pure H_2O is supplied to the PEM and the evolved H^+ is transported through the solid electrolyte, while in this study, the acidic H_2O is directly in contact with the anode. Due to the loss of iridium, the current density observed in the acidic and alkaline pH solutions in **Figures 3.15a** and **3.15b** did not therefore entirely originate from the water electrolysis, indicative of a Faradaic efficiency much lower than 100%.
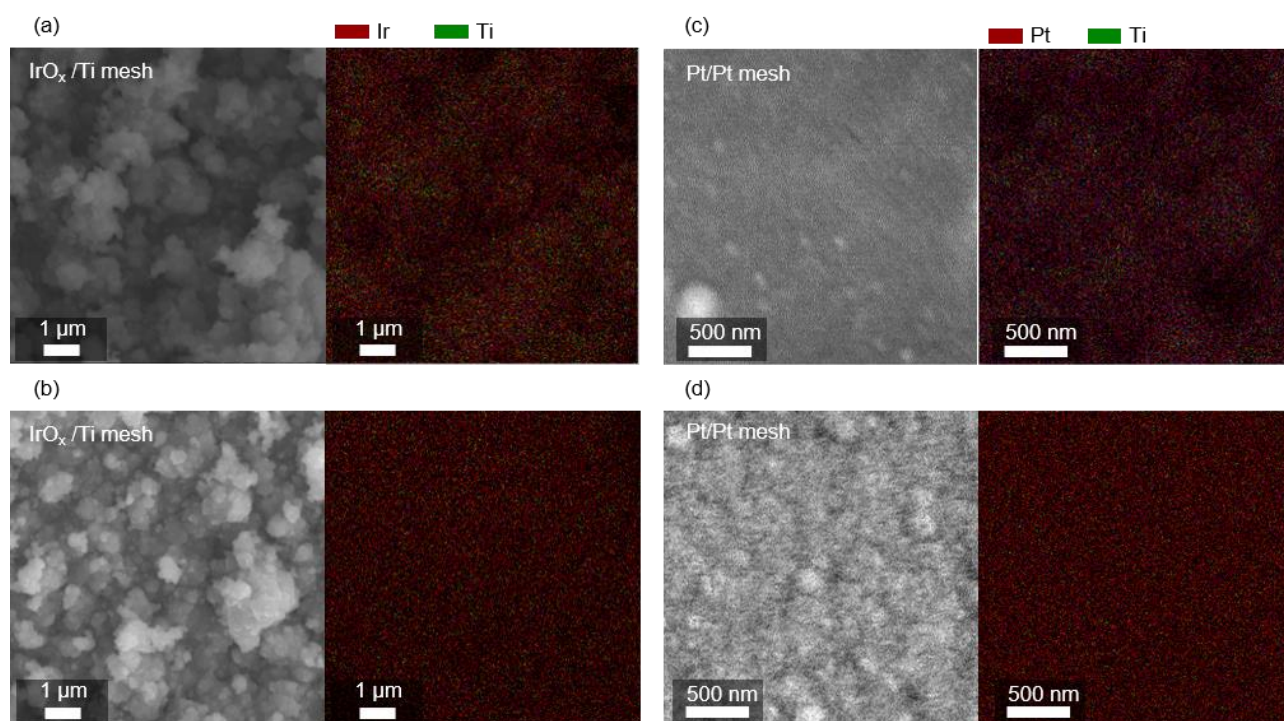
Figure 3.9. Surface morphology of model electrodes. Scanning electron microscopy (SEM) images of (a,b) IrO_x/Ti mesh and (c,d) Pt/Pt mesh. The panels (a) and (b) show the as-prepared electrodes while panels (c) and (d) show the pot-reaction ones. The corresponding energy dispersive x-ray spectroscopy (EDS) mapping is displayed next to each SEM image.

Figure 3.10. Surface morphology of IrO_x/Ti mesh. SEM images of (a) bare Ti mesh, (b) fresh IrO_x/Ti mesh, and (c) used IrO_x/Ti mesh electrodes. All figures on the left were taken in high resolution, and the corresponding images at lower magnification are shown on the right.

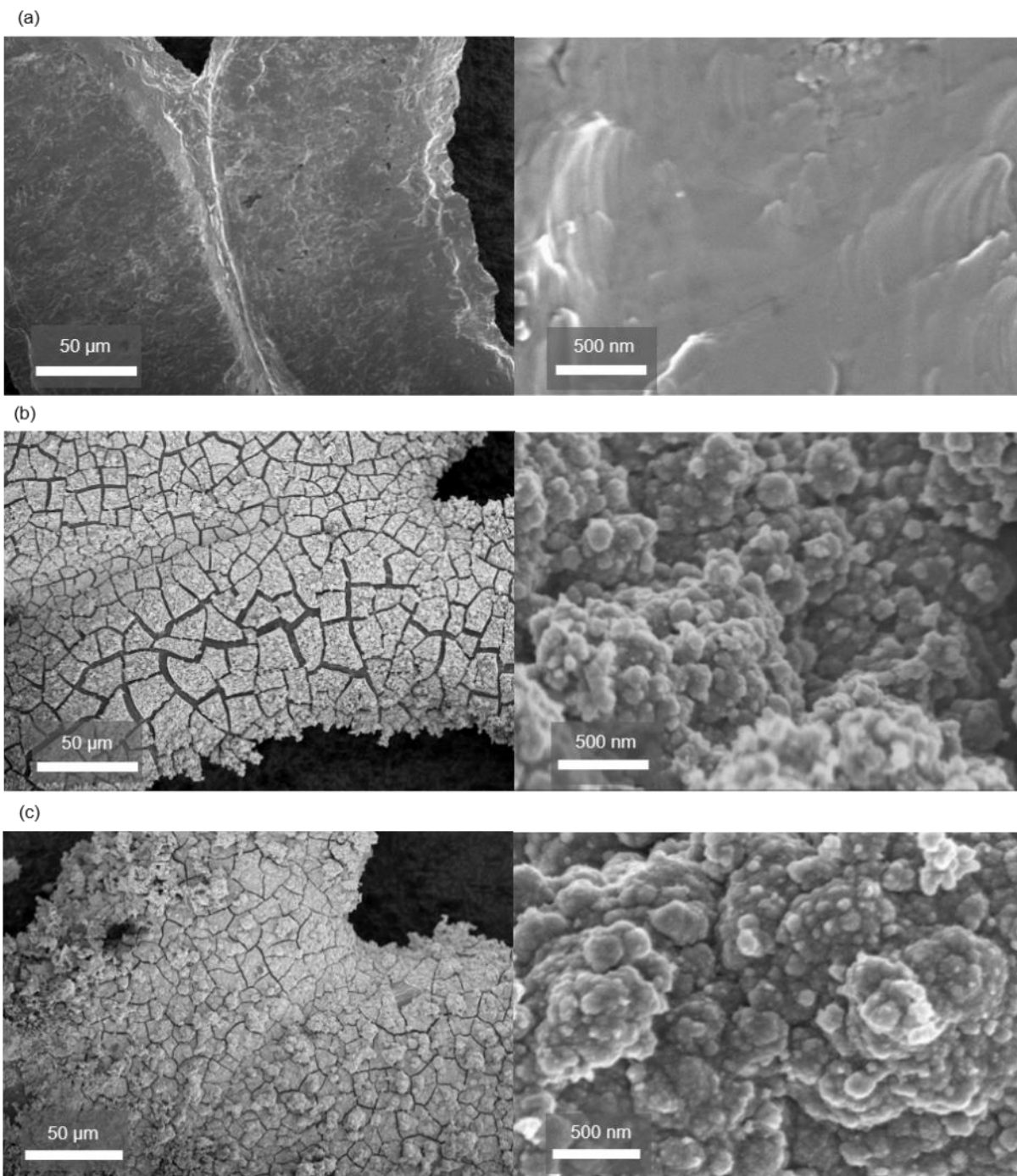**Figure 3.11.** Surface morphology of Pt/Pt mesh. SEM images of (a) bare Pt mesh, (b) fresh Pt/Pt mesh, and (c) used Pt/Pt mesh electrodes. All figures on the left were taken in high resolution, and the corresponding images at lower magnification are shown on the right.
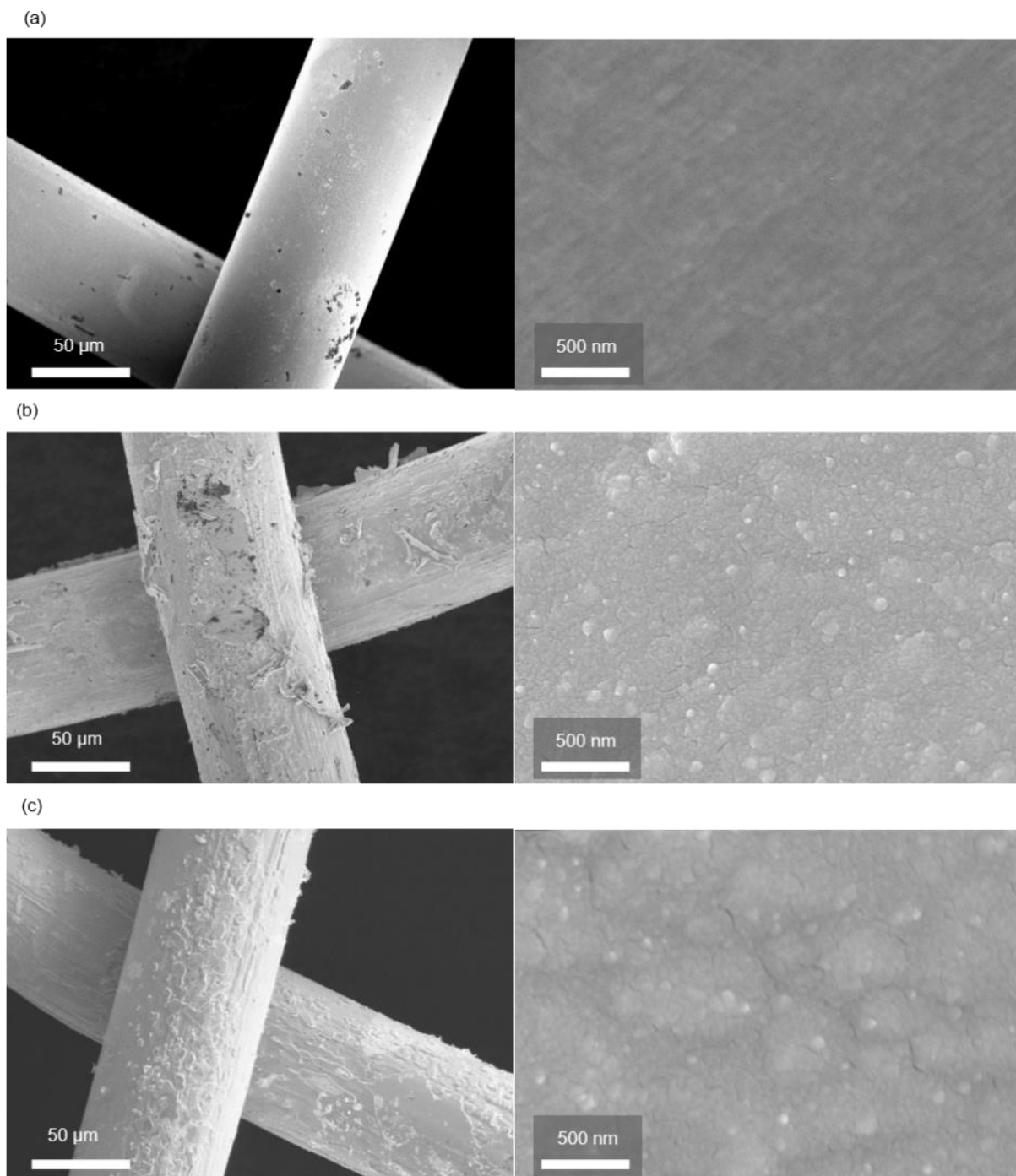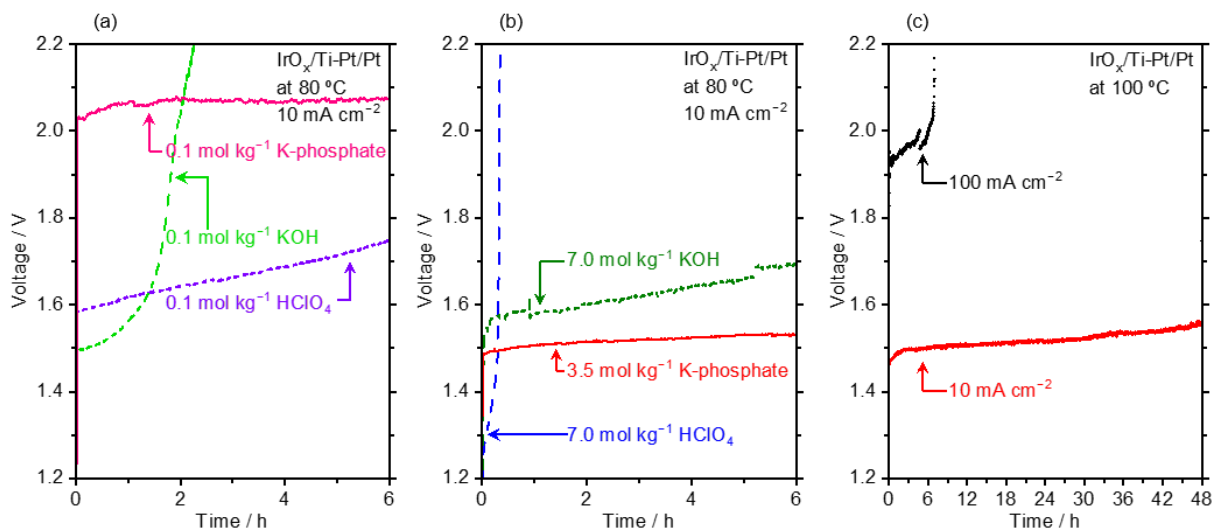
Figure 3.12. Water electrolysis performance in densely buffered solutions without *iR*-correction corresponding to **Figure 3.15**. (a) Chronopotentiometry (CP) profile performed at 10 mA cm^{-2} and 80 °C in electrolyte solutions of 0.1 mol kg^{-1} KOH, 0.1 mol kg^{-1} HClO$_4$, and 0.1 mol kg^{-1} K-phosphate. (b) CP profile performed at 10 mA cm^{-2} and 80 °C in electrolyte solutions of 7.0 mol kg^{-1} KOH, 7.0 mol kg^{-1} HClO$_4$, and 3.5 mol kg^{-1} K-phosphate. These profiles are the average of the experiments for 3.5 mol kg^{-1} K-phosphate, 7.0 mol kg^{-1} HClO$_4$, and KOH (c) Overall water electrolysis performance was accessed by CP at 10 and 100 mA cm^{-2} in 4.1 mol kg^{-1} K-phosphate solutions at 100 °C. All measurements were performed in the two-electrode configuration using IrO$_x$/Ti mesh and Pt/Pt mesh as anode and cathode with a geometric surface area of 1.0 cm^2, respectively, under Ar bubbling. The pH level of K-phosphate solutions was adjusted to 7.0 at 25 °C prior to the measurements.
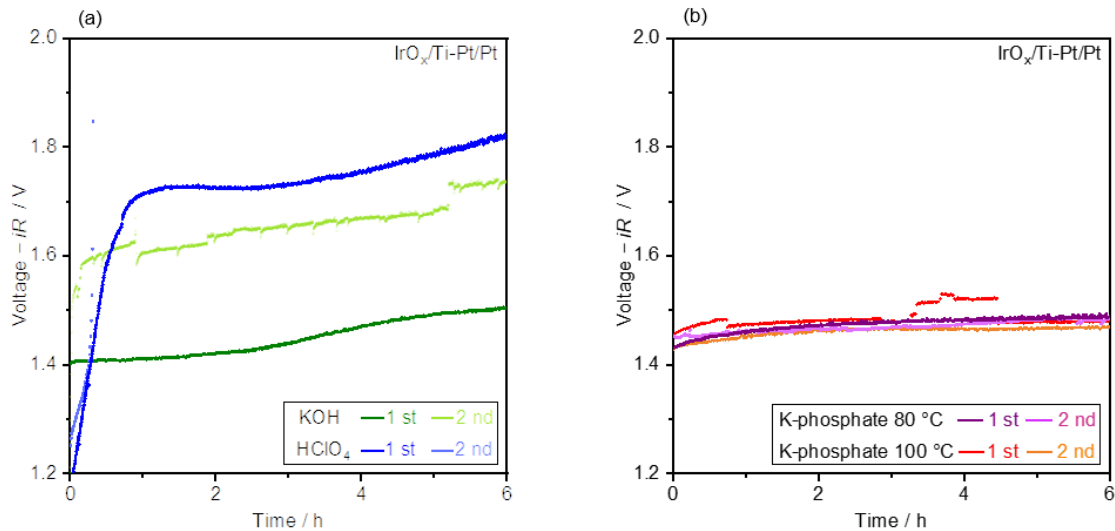
Figure 3.13. Raw data of the water electrolysis performance. Chronopotentiometry (CP) profiles at 10 mA cm^{-2} were recorded with Ar bubbling in electrolyte solutions of (a) 7.0 mol kg^{-1} HClO$_4$ and 7.0 mol kg^{-1} KOH at 80 °C as well as (b) K-phosphate of 3.5 mol kg^{-1} at 80 °C and of 4.1 mol kg^{-1} at 100 °C. The voltage displayed in the figure has been *iR*-corrected with measured impedance value. The raw data shown herein were used to prepare the figure displayed in **Figure 3.15a**. Each measurement was performed twice with newly prepared electrodes. The pH level of K-phosphate solutions was adjusted to 7.0 at 25 °C prior to the measurements.
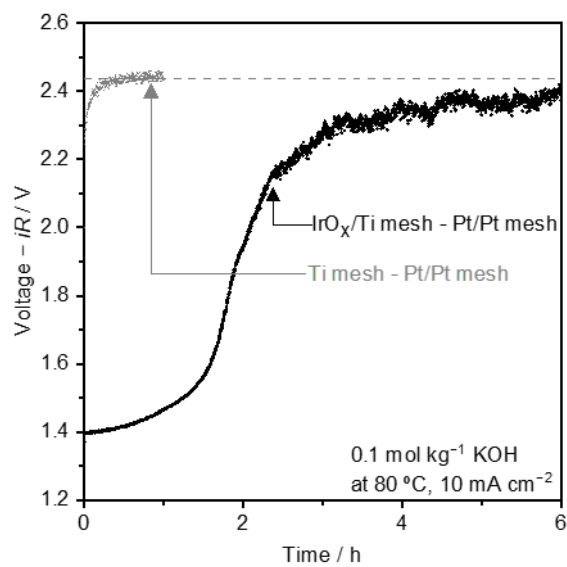
Figure 3.14. Water electrolysis performance in KOH. CP profiles at 10 mA cm^{-2} were obtained in the two-electrode configuration using IrO$_x$/Ti mesh anode and Pt/Pt mesh cathode as well as Ti mesh anode and Pt/Pt mesh cathode. These measurements were conducted in 0.1 mol kg^{-1} KOH solution at 80 °C. The voltage displayed in the figure has been *iR*-corrected with measured impedance value.
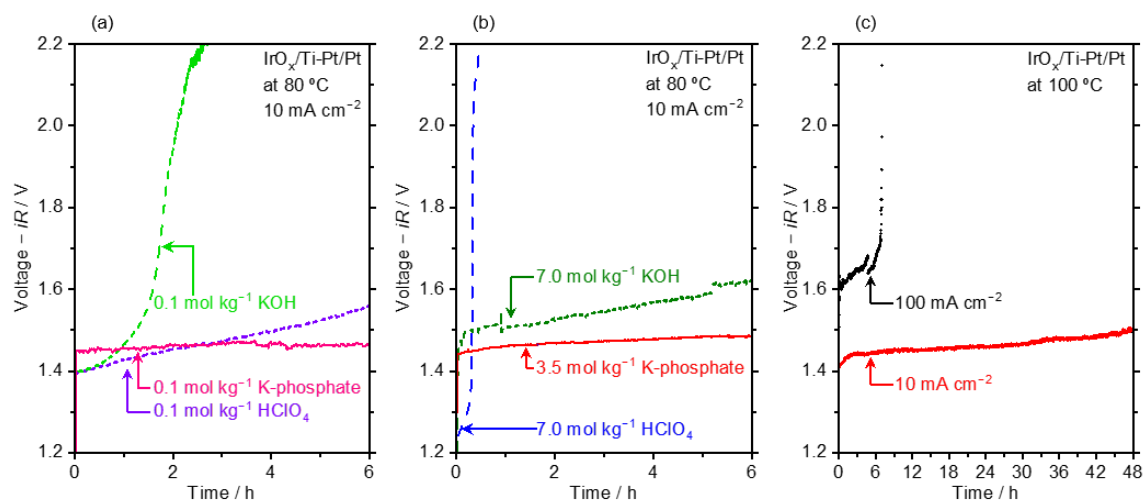
Figure 3.15. Water electrolysis performance in concentrated buffer solutions. (a) Chronopotentiometry (CP) profile performed at 10 mA cm^{-2} and 80 °C in electrolyte solutions of 0.1 mol kg^{-1} KOH, 0.1 mol kg^{-1} HClO$_4$, and 0.1 mol kg^{-1} K-phosphate. (b) CP profile performed at 10 mA cm^{-2} and 80 °C in electrolyte solutions of 7.0 mol kg^{-1} KOH, 7.0 mol kg^{-1} HClO$_4$, and 3.5 mol kg^{-1} K-phosphate. These profiles are the average of the experiments for 3.5 mol kg^{-1} K-phosphate, 7.0 mol kg^{-1} HClO$_4$, and KOH (see **Figure 3.13** for raw data. (c) Overall water electrolysis performance was accessed by CP at 10 and 100 mA cm^{-2} in 4.1 mol kg^{-1} K-phosphate solutions at 100 °C. All measurements were performed in the two-electrode configuration using IrO$_x$/Ti mesh and Pt/Pt mesh as anode and cathode with a geometric surface area of 1.0 cm^2, respectively, under Ar bubbling. The voltage displayed in the figure has been *iR*-corrected with measured impedance value unless otherwise noted. The pH level of K-phosphate solutions was adjusted to 7.0 at 25 °C prior to the measurements.

In stark contrast, in 0.1 and 3.5 mol kg^{-1} K-phosphate solutions (**Figures 3.15a** and **b**, respectively), an overall voltage of 1.45 and 1.44 V in the beginning increased only by 0.02 and 0.04 V after 6 h of testing at almost 100% of Faradaic efficiency toward the HER and OER (see **Figure 3.16** for gas quantification). The stability during not only the prolonged operation but also the startup-shutdown cycling was regarded as a key to the practical implementation.[71,72] **Figure 3.17** shows the voltage profile obtained by periodically performing CP at 10 mA cm^{-2} with an interval of 1 h in 7.0 mol kg^{-1} KOH and the 3.5 mol kg^{-1} K-phosphate solutions at 80 °C. While in the KOH solution, the initial voltage increased with on-off cycling, the initial voltage in the K-phosphate solution was

unchanged during the testing. These results demonstrated the stable operation made possible by the buffered solution at elevated temperatures, contrasting to the extreme pH counterparts. Hence, the concentrated K-phosphate solution not only exhibits the fast mass-transport but also achieves catalytic performance comparable to the extreme pH conditions as well as more stable operation.
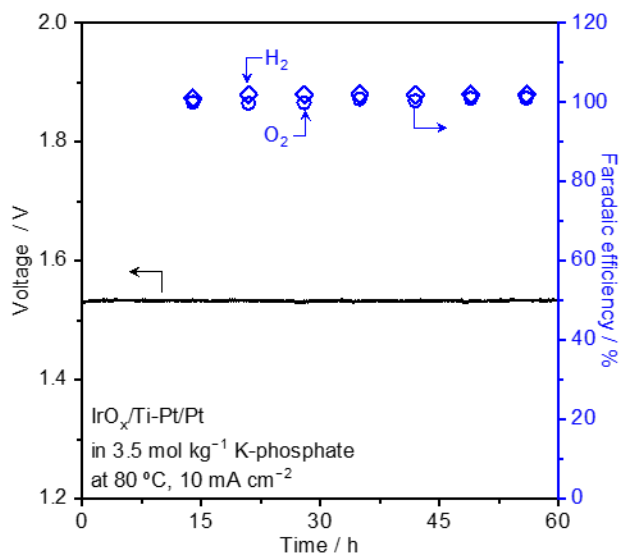
Figure 3.16. Demonstration of water electrolysis in densely buffered solutions at neutral pH. Overall water electrolysis performance was accessed by CP at 10 mA cm^{-2} in K-phosphate solutions of 3.5 mol kg^{-1} at 80 °C in the two-electrode configuration using a IrO$_x$/Ti mesh anode and a Pt/Pt mesh cathode with Ar bubbling. The evolved gases were detected by on-line gas chromatograph equipped with thermal conductivity detector. The pH level of K-phosphate solutions was adjusted to 7.0 at 25 °C prior to the measurements.
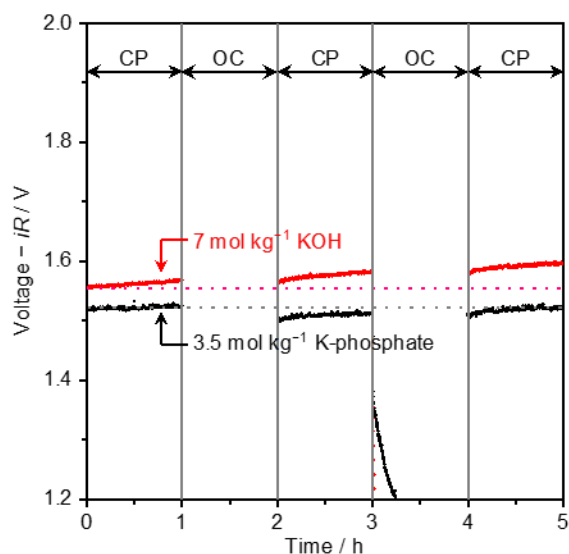
Figure 3.17. On-off cycling of water electrolysis in densely buffered solutions. On-off testing results were obtained by periodic CP at 10 mA cm^{-2} for 1 h with an interval of 1 h at open-circuit (OC) condition in 7.0 mol kg^{-1} KOH and 3.5 mol kg^{-1} K-phosphate (pH 7.0) at 80 °C. The measurement was performed after CP for 6 h shown in **Figure 3.15b**. The voltage displayed in the figure has been *iR*-corrected with measured impedance value. The pH level of K-phosphate solutions was adjusted to 7.0 at 25 °C prior to the measurements

At this stage, the origin of the improved stability in the buffered condition with respect to the extreme pH counterparts remains unclear. Nonetheless, provided that the loss of performance in the extreme pH condition originated from the dissolution of iridium, as well as superior stability observed in the K-phosphate solution (**Figures 3.15a, 3.15b**), I postulate that the phosphate species would prevent its dissolution in the buffered solutions in a manner similar to the self-healing mechanism claimed previously.[73,74] In the case of reported Co-phosphate during the OER catalysis, Co species undergo oxidation from +II to +III and eventually to +IV, which upon the release of O_2 returns back to the original +II state.[75,76] This Co (+II) state readily dissolves in the solution, which in the presence of phosphate species forms cobalt-phosphate complex upon dissolution and precipitates on the electrode surface.[75-77] The re-deposited Co (+II) species on the electrode surface reacts with Co (+IV) species on the electrode forming +III via disproportionation reaction and hence participate again in

the catalytic cycle.[76] In the case of iridium, its oxidation state is considered to change from +III to +IV and then to +V that eventually back to +III state upon release of O_2 according to the literature.[69,78] Similarly to the case of Co, the lowest valence state of +III is known to dissolve,[69] which can be one route of iridium dissolution leading to performance loss. To the best of my knowledge, the solubility product (K_{sp}) of iridium (+III) and phosphate has not been determined in any literature. I anticipate similarly low K_{sp} for Ir-phosphate to Co-phosphate, given that they both fall in the same group in the periodic table and therefore have similar character of d-electrons. Once the Ir (+III) state is redeposited on the electrode surface, this species can be anodically oxidized to deposit on the surface[29] and can again take part in the catalytic cycle.

For targeting practical applications, additional catalytic testing was conducted for longer periods of time at 100 °C using model Pt/Pt mesh and IrO_x/Ti mesh electrodes. **Figure 3.15c** presents the CP profile at 10 mA cm^{-2} for 48 h, in which the initial *iR*-free voltage of 1.44 V remained reasonably stable during the operation and ended at 1.50 V. However, the profile largely differed when performed at a higher current density. At 100 mA cm^{-2}, the voltage was initially ca. 1.6 V that rapidly increased over several hours, reaching >6 V after 6 h. This voltage of >6 V agreed with that using bare Ti mesh anode (**Figure 3.18**), indicative of the loss of iridium species. I consider two possible origins of the loss of iridium at higher current densities in the buffered solutions: First, the higher anodic potential of > 1.6 V vs. reversible hydrogen electrode (RHE) was reported to drive the overoxidation of iridium into the +VI state at acidic pH levels, which dissolves into the solution as a form of IrO_4^{2-}, resulting in the loss in the performance.[69] This scenario pointed to the use of other anionic species that achieve smaller K_{SP} with iridium as well as increasing the number of iridium sites to improve stability. Second, the stripping of the catalyst layer could be induced by the physical force of the bubbles, which would be manifested at higher reaction rates.[79]
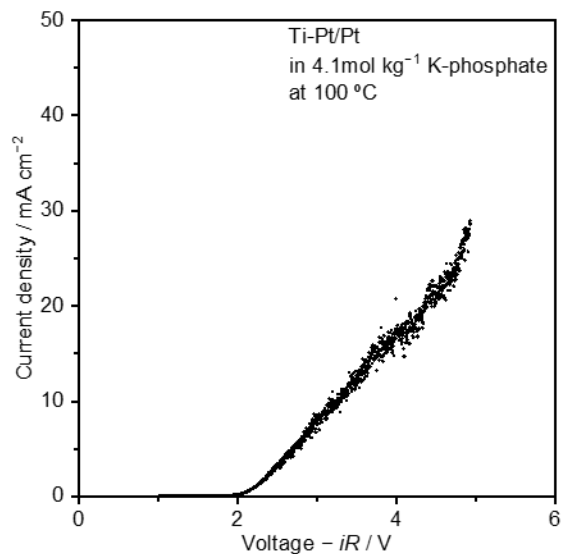
Figure 3.18. Water electrolysis performance using Ti mesh anode at the neutral pH. CV profiles at a scan rate of 10 mV s^{-1} were recorded in K-phosphate solutions of 4.1 mol kg^{-1} at 100 °C in the two-electrode configuration using a Ti mesh anode and a Pt/Pt mesh cathode with Ar bubbling. The pH level of K-phosphate solutions was adjusted to 7.0 at 25 °C prior to the measurements. The voltage displayed in the figure has been *iR*-corrected with the measured impedance value.
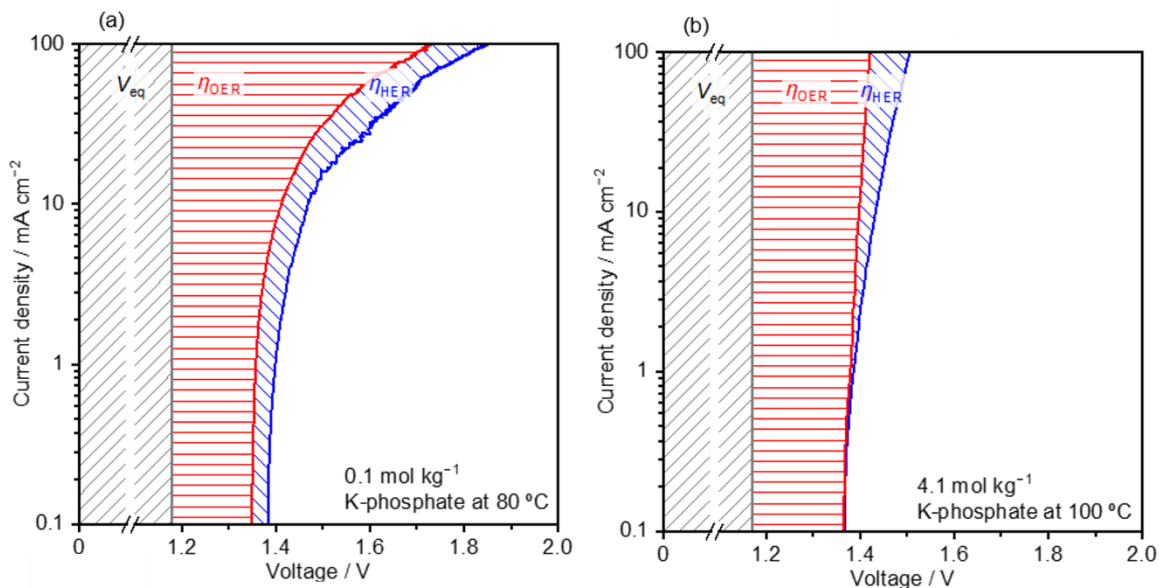
Figure 3.19. Voltage breakdown of water electrolysis in buffered solutions at neutral pH. (a) Voltage breakdown for the water electrolysis at a scan in K-phosphate of 0.1 mol kg^{-1} 80 °C, and (b) in K-phosphate of 4.1 mol kg^{-1} 100 °C determined by electrocatalytic testing for the half-cell reactions. η_i indicates the overpotential for process i. All measurements were performed in the three-electrode configuration using IrO$_x$/Ti mesh, Pt/Pt mesh, and Hg/Hg$_2$Cl$_2$ as anode, cathode, and reference electrode, respectively, under Ar bubbling at a scan rate of 10 mV s^{-1}. The voltage displayed in the figure has been *iR*-corrected with measured impedance value. The pH levels of K-phosphate solutions were adjusted to 7.0 at 25 °C prior to the measurements.

Cyclic voltammetry (CV) was performed in the two- and three-electrode configurations to describe the breakdown of the initial voltage of water electrolysis under neutral pH (see **Figure 3.20** for the Tafel plots of half-reactions). **Figure 3.19** presents the breakdown in 0.1 mol kg^{-1} K-phosphate solution at 80 °C and in 4.2 mol kg^{-1} K-phosphate solution at 100 °C. In both cases, the anodic half-reaction required substantial overpotentials, e.g., 240 mV and 230 mV at 10 mA cm^{-2} in 0.1 and 4.5 mol kg^{-1} K-phosphate solutions, respectively, even using the IrO$_x$ electrode. Remarkably, the anodic overpotential in the dilute K-phosphate solution became substantially larger than that in 4.5 mol kg^{-1} K-phosphate solutions at higher reaction rates reaching 100 mA cm^{-2}, presumably because the buffering capacity was insufficient to mitigate the local pH alteration. This observation further emphasizes the value of using the concentrated buffer solution to sustain a higher reaction rate. The

voltage during water electrolysis in the highly acidic and alkaline solutions could not be broken-down because their pH values are below 0 and above 14, which exceeds the range of the pH meter.
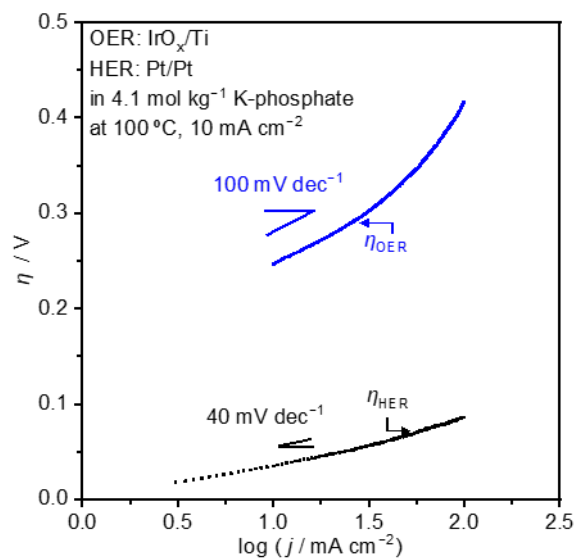
Figure 3.20. Tafel plots of the hydrogen evolution reaction (HER) and oxygen evolution reaction (OER) over Pt/Pt mesh and IrO$_x$/Ti mesh, respectively. All measurements were recorded by CP measurement at a scan rate of 10 mV s^{-1} in 4.1 mol kg^{-1} K-phosphate at 100 °C in the three-electrode configuration with Hg/Hg$_2$Cl$_2$ (saturated KCl) reference electrode. The pH of the K-phosphate solutions was adjusted to 7.0 at 25 °C prior to the measurements.

Figure 3.21. Cyclic voltammograms recorded at a scan rate of 10 mV s^{-1} in K-phosphate of 4.1 mol kg^{-1} 100 °C in the two-electrode configuration. V_{eq} denotes equilibrium voltage for water electrolysis. The current-voltage relationship over the NiFeO$_x$/Ni foam anode and NiMo/Ni foam cathode in 30 wt% KOH at 73 °C is also presented in the figure, which was adopted from a previous study.[80] All measurements were performed in the two-electrode configuration using IrO$_x$/Ti mesh and Pt/Pt mesh as anode and cathode, respectively, under Ar bubbling. The voltage displayed in the figure has been *iR*-corrected with measured impedance value. The pH level of K-phosphate solutions was adjusted to 7.0 at 25 °C prior to the measurements.

The poor stability of IrO$_x$ during the water electrolysis in both acidic and alkaline conditions hampered fair comparison at the steady-state. To fairly judge the electrolysis performance in the concentrated phosphate, I compare it with those of industrially relevant current-potential relationship obtained with NiFeO$_x$ anode and NiMo cathode in KOH solutions. **Figure 3.21** shows the cathodic scan of the CV profile obtained in the saturated K-phosphate solutions of 4.1 mol kg^{-1} at 100 °C using the Pt cathode and IrO$_x$ anode, as well as that in 30 wt% KOH solution at 73 °C using NiMo cathode and NiFeO$_x$ anode (see **Figure 3.22** for comparison between the CVs in the saturated K-phosphate solution at 80 °C and 30 wt% KOH solution at 73 °C). The latter was adopted from a previous study, whose performance was almost identical to the best performing electrolyzer in a variety of industrial alkaline electrolyzer with temperature ranging from 70 °C to 90 °C.[80] In neutral pH condition, the voltage at 10 mA cm^{-2} was 1.44 V, which agreed with the initial value of 1.44 V of the water

electrolysis performance (**Figure 3.15c**). A current density of 100 mA cm^{-2} was achieved at a voltage of 1.49 V at 100 °C, which is comparable to the performance of 1.50 V attained in the alkaline condition at 73 °C.

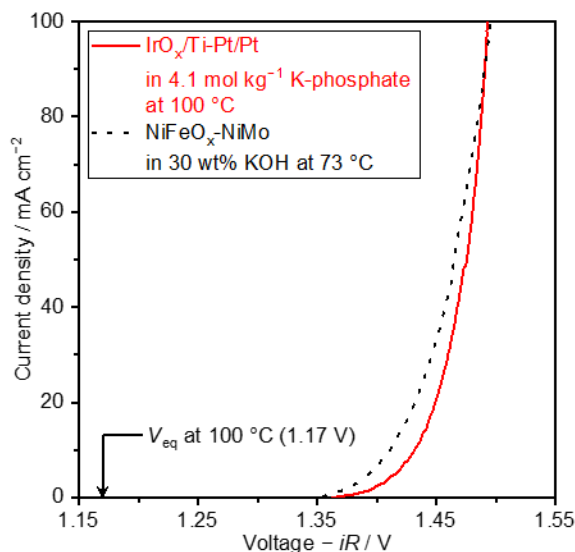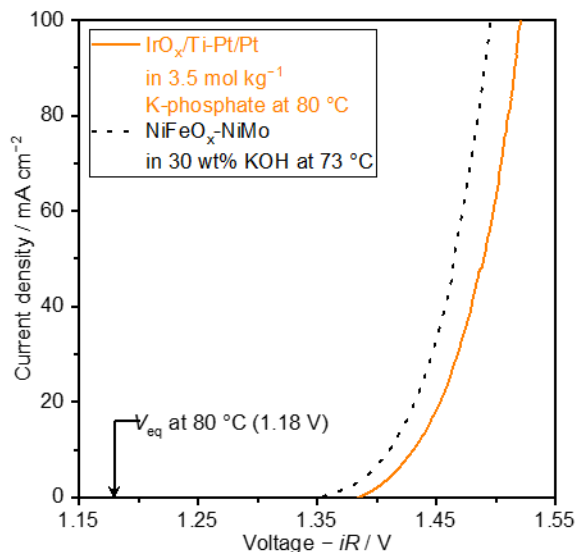**Figure 3.22.** Cyclic voltammograms recorded at a scan rate of 10 mV s^{-1} in K-phosphate of 3.5 mol kg^{-1} 80 °C in the two-electrode configuration. V_{eq} denotes equilibrium voltage for water electrolysis. The current-voltage relationship over the NiFeO$_x$/Ni foam anode and NiMo/Ni foam cathode in 30 wt% KOH at 73 °C is also presented in the figure, which was adopted from a previous study.[80] All measurements were performed in the two-electrode configuration using IrO$_x$/Ti mesh and Pt/Pt mesh as anode and cathode, respectively, under Ar bubbling. The voltage displayed in the figure has been *iR*-corrected with measured impedance value. The pH level of K-phosphate solutions was adjusted to 7.0 at 25 °C prior to the measurements.

Seeking for cost-effective alternative catalysts, I employed NiFeO$_x$ as the anode in 4.1 mol kg^{-1} K-phosphate solution, but found that the overall voltage at the neutral pH was as large as 1.76 V at 20 mA cm^{-2}, which was larger by 200 mV than those at alkaline conditions (**Figure 3.23**). Interestingly, its performance at steady-state was identical with the pristine NiO$_x$ electrode, indicative of loss of NiFeO$_x$ during the OER at the neutral pH. Another previous study consistently reported the dissolution of nickel and iron species from NiFeO$_x$ anode during OER in 0.1 M K-phosphate solution at pH 7.[81] The lack of active and stable electrodes composed of cost-effective and earth-abundant

elements that catalyze the OER at the near-neutral pH urge us to develop such electrocatalysts for the production of CO_2-free hydrogen on a large scale.
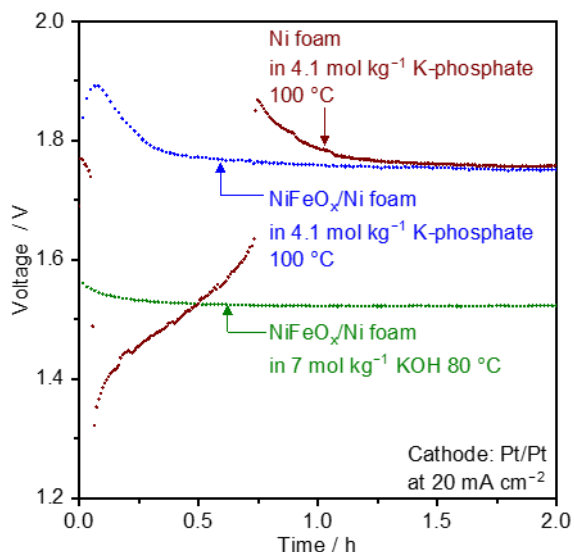
Figure 3.23. Water electrolysis performance using Ni-based materials as anode. CP profile at 20 mA cm^{-2} were recorded in 4.1 mol kg^{-1} K-phosphate solution at 100 °C in the two-electrode configuration using NiFeO$_x$/Ni foam anode or Ni foam anode, together with the Pt/Pt cathode under Ar bubbling. As a control experiment, a CP profile was obtained in 7.0 mol kg^{-1} KOH solution at 80 °C using the NiFeO$_x$/Ni foam anode and the Pt/Pt cathode. The pH level of the K-phosphate solutions was adjusted to 7.0 at 25 °C prior to the measurements.

All in all, this section demonstrated that model iridium and platinum electrodes have stable operation of water electrolysis in buffered conditions at neutral pH. The performance was found to be comparable with the extreme pH counterparts. The system however was subject to gradual loss in the performance with time at higher reaction rates, e.g., 100 mA cm^{-2}, presumably due to the dissolution of iridium anode. Such poor stability can be mitigated by the further electrolyte engineering as well as development of active catalyst at higher dispersion, calling for reserach activity in this direction.

3.4.   Conclusion

The physicochemical properties of concentrated phosphate solutions (> 0.1 mol kg^{-1}) at neutral pH were investigated for their potential use as an electrolyte for the water electrolysis. The measured solubility of M-phosphate solutions (M=Li, Na, K, Cs) revealed that Na-, K- and Cs-phosphate solutions achieved higher molality at elevated temperatures likely due to the affinity of these alkali metal cation with the phosphate anions present in the solution, namely $H_2PO_4^-$ and HPO_4^{2-}. Their viscosity and conductivity were then determined at a variety of temperatures and molalities. At a given molality, the K-phosphate solution exhibited a smaller viscosity as well as larger conductivity presumably due to its smaller hydrated ion size. Notably, these experimentally determined physicochemical properties were successfully rationalized by the extrapolation of the existing model dealing with the dilute solution. These findings help to rationally select K-phosphate as the optimal electrolyte at the neutral pH, which can achieve the highest mass-transport fluxes during the water electrolysis among M-phosphate solutions. By focusing on this K-phosphate, the mass-transport flux during water electrolysis was computed, revealing that the losses due to the mass-transport in the saturated K-phosphate solutions, i.e., 3.5 mol kg^{-1} at 80 °C and 4.1 mol kg^{-1} at 100 °C, could be potentially comparable with those of existing electrolyzers. Subsequently, using an IrO_x anode and a Pt cathode, the water electrolysis was demonstrated at 10 mA cm^{-2} in the K-phosphate solutions at elevated temperatures. It was observed that the overall voltage was reasonably comparable with the extreme pH counterparts, and remained stable during the hours of operation, contrasting to the acidic and alkaline pH conditions that experienced a rapid deactivation of the anodes. However, the voltage at a higher rection rate of 100 mA cm^{-2} experienced a rapid increase with time in the buffered condition likely because of the deactivation of the IrO_x anode. In addition, voltage breakdown analysis pointed to the largest losses in the performance due to the kinetic overpotentials at the anode. These observations call for the development of electrocatalyst-electrolyte system to improve the activity and stability at the anode at the neutral pH. Overall, my findings presented in this study demonstrated that the concentrated buffer solutions are a potential electrolyte for water electrolysis at neutral pH. Further developments in anode material functional in such a condition was pointed to as a prerequisite for practical applications.

3.5.   References

[1]   S. Satyapal, J. Petrovic, C. Read, G. Thomas, G. Ordaz, *Catal. Today* **2007**, *120*, 246-256.

[2] Z. W. She, J. Kibsgaard, C. F. Dickens, I. Chorkendorff, J. K. Nørskov, T. F. Jaramillo, *Science* **2017**, *355*, eaad4998.

[3] J. Yang, A. Sudik, C. Wolverton, D. J. Siegel, *Chem. Soc. Rev*. **2010**, *39*, 656-675.

[4] L. Bartuccioli, A. Chan, D. Hart, F. Lehner, B. Madden, E. Standen, *"Development of water electrolysis in the European Union"*, Fuel Cells and Hydrogen Joint Undertaking, **2014**.

[5] D. G. Nocera, *Inorg. Chem.* **2009**, *48*, 10001-10017.

[6] T. Shinagawa, K. Takanabe, *ChemSusChem* **2017**, *10*, 1318-1336.

[7] A. Bergmann, I. Zaharieva, H. Dau, P. Strasser, *Energy Environ. Sci*. **2013**, *6*, 2745-2755.

[8] P. Zhang, M. Wang, H. Chen, Y. Liang, J. Sun, L. Sun, *Adv. Energy Mater*. **2016**, *6*, 1502319.

[9] S. Anantharaj, V. Aravindan, *Adv. Energy Mater.* **2020**, *10*, 1902666.

[10] S. Trasatti, *J. Electroanal. Chem.* **1972**, *39*, 163-184.

[11] C. C. L. McCrory, S. Jung, I. M. Ferrer, S. M. Chatman, J. C. Peters, T. F. Jaramillo, *J. Am. Chem. Soc*. **2015**, *137*, 4347-4357.

[12] Y. Lee, J. Suntivich, K. J. May, Erin E. Perry, and Yang Shao-Horn, *J. Phys Chem Lett.* **2012**, *3*, 399-404.

[13] B. E. Conway, L. Bai, *Int. J. Hydrogen Energy* **1986**, *11*, 533-540.

[14] C. C. L. McCrory, S. Jung, J. C. Peters, T. F. Jaramillo, *J. Am. Chem. Soc*. **2013**, *135*, 16977-16987.

[15] J. R. McKone, B. F. Sadtler, C. A. Werlang, N. S. Lewis, H. B. Gray, *ACS Catal*. **2013**, *3*, 166-169.

[16] S. Anantharaj, V. Aravindan, *Adv. Energy Mater.* **2020**, *10*, 190266.

[17] D. Strmcnik, M. Uchimura, C. Wang, R. Subbaraman, N. Danilovic, D. van der Vliet, A. P. Paulikas, V. R. Stamenkovic, N. M. Markovic, *Nat. Chem.* **2013**, *5*, 300-306.

[18] T. Shinagawa, A. T. Garcia-Esparza, K. Takanabe, *ChemElectroChem* **2014**, *1*, 1497-1507.

[19] T. Takashima, K. Ishikawa, H. Irie, *ACS Catal*. **2019**, *9*, 9212-9215.

[20] W. Sheng, Z. Zhuang, M. Gao, J. Zheng, G. Chen, Y. Yan, *Nat. Commun.* **2015**, *6*, 5848.

[21] T. Shinagawa, M. T-K. Ng, K. Takanabe, *ChemSusChem* **2017**, *10*, 4155-4162.

[22] T. Shinagawa, K. Takanabe, *J. Phys. Chem. C* **2015**, *119*, 20453-20458.

[23] I. Katsounaros, J. C. Meier, S. O. Kemm, A. A. Topalov, P. U. Biedermann, M. Auinger, K. J. J. Mayrhofer, *Electrochem. Commun.* **2011**, *13*, 634-637.

[24] M. Auinger, I. Katsounaros, J. C. Meier, S. O. Klemm, P. U. Biedermann, A. A. Topalov, M. Rohwerder, K. J. J. Mayrhofer, *Phys. Chem. Chem. Phys.* **2011**, *13*, 16384-16394.

[25] L. D. S. Muñoz, A. Bergel, D. Féron, R. Basséguy, *Int. J. Hydrogen Energy* **2010**, *35*, 8561-8568.

[26] K. Obata, L. Stegenburga, K. Takanabe, *J. Phys. Chem. C* **2019**, *123*, 21554-21563.

[27] T. Shinagawa, K. Obata, K. Takanabe, *ChemCatChem* **2019**, *11*, 5961-5968.

[28] W.M. Haynes, D.R. Lide, *Handbook of Chemistry and Physics, 92nd ed.*, CRC Press, Boca Raton, FL, **2011**.

[29] M. A. Petit, V. Plichon, *J. Electroanal. Chem.* **1998***, 444,* 247-252.

[30] A. M. Feltham, M. Spiro, *Chem. Rev.* **1971**, *71*, 177-193.

[31] I. Lee, K-Y Chan, D. L. Phillips, *Appl. Surf. Sci.* **1998**, *136*, 321-330.

[32] Z. Lu, W. Xu, W. Zhu, Q. Yang, X. Lei, J. Liu, Y. Li, X. Sun, X. Duan, *Chem. Commun.* **2014**, *50*, 6479-6482.

[33] M. Suermann, T. J. Schmidt, F. N. Büchi, *Electrochim. Acta* **2018**, *281*, 466-471.

[34] P. Atkins, J. D. Paula, *Atkins' Physical Chemistry*, *eighth ed.*, W. H. Freeman and Company, New York, NY, **2006**.

[35] S. Da Silva, R. Basséguy, A. Bergel, *Electrochim. Acta* **2004**, *49*, 4553-4561.

[36] Y. Dong, S. Komarneni, N. Wang, W. Hu, W. Huang, *J. Mater. Chem. A* **2019**, *7*, 6995-7005.

[37] J. Wang, S. Zuo, G. Wei, Y. Niu, L. Guo, Z. Chen, *J. Phys. Chem. C* **2019**, *123*, 12313-12320.

[38] K. Schrödter, G. Bettermann, T. Staffel, F. Wahl, T. Klein, T. Hofmann, *Ullmann's Encyclopedia of Industrial Chemistry: Phosphoric Acid and Phosphates*, Willey, New York, NY, **2008**.

[39] W. Kunz, *Specific Ion Effects*, World Scientific Publishing Co. Pte. Ltd., Singapore, **2010.**

[40] P. Ball, J. E. Hallsworth, *Phys. Chem. Chme. Phys*. **2015**, *17*, 8297.

[41] W. Kunz, J. Henle, B. W. Ninham, *Curr. Opin. Colloid Interface Sci*. **2004**, *9*, 19-37.

[42] K. D. Collins, G. W. Neilson, J. E. Enderby *Biophys. Chem.* **2007**, *128*, 95-104.

[43] R. G. Pearson, *J. Am. Chem. Soc.* **1963**, *85*, 3533-3539.

[44] R. G. Pearson, *J. Chem. Educ*. **1987**, *64*, 561-567.

[45] E. N. Bastrakov, S. Jaireth, T. P. Mernagh, *Solubility of Uranium in Hydrothermal Fluids at 25 °C to 300 °C. Implications for the Formation of Uranium Deposits*, Geoscience Australia, Canberra, **2010**.

[46] D. Feakins, W. E. Waghorne, K. G. Lawrence, *J. Chem. Soc., Faraday Trans. 1* **1986**, *82*, 563-568.

[47] A. J. Bard, L. R. Faulkner, *Electrochemical Method: Fundamentals and Applications*, Willey, New York, NY, **2010**.

[48] R. H. Ewell, *J. Appl. Phys.* **1938**, *9*, 252.

[49] R. S. Patil, V. R. Shaikh, P. D. Patil, A. U. Borse, K. J. Patil, *J. Mol. Liq.* **2014**, *200*, 416-424.

[50] B. S. Krumgalz, *J. Chem. Soc., Faraday Trans. 1* **1980**, *76*, 1275-1286.

[51] H. Falkenhagen, E. L. Vernon, *Phil. Mag.* **1932**, *14*, 537-565.

[52] E. R. Nightingale Jr., *J. Phys. Chem.* **1959**, *63*, 1381-1387.

[53] D. M. See, R. E. White, *J. Chem. Eng. Data* **1997**, *42*, 1266-1268.

[54] T. Shinagawa, K. Takanabe, *J. Phys. Chem. C* **2016***, 120,* 1785-1794.

[55] H. Du, J. C. Rasaiah, J. D. Miller*, J. Phys. Chem. B* **2007**, *111,* 209-217.

[56] M. Y. Kiriukhin, K. D. Collins, *Biophys. Chem.* **2002**, *99*, 155-168.

[57] O. Y. Samoilov, *Discuss. Faraday Soc*. **1957**, *24*, 141-146.

[58] G. Jones, M. Dole, *J. Am. Chem. Soc.* **1929**, *51*, 2950-2964.

[59] S. Marini, P. Salvi, P. Nelli, R. Pesenti, M. Villa, M. Berrettoni, G. Zangari, Y. Kiros, *Electrochimica Acta* **2012**, *82*, 384-391.

[60] R. Phillips, C. W. Dunnill, *RSC Adv.*, **2016**, *6*, 100643-100651.

[61] R. E. White, J. O'M. Bockris, B. E. Conway, *Modern Aspects of Electrochemistry No. 15*, Prenum Press, New York, **1983**.

[62] Y. Kageshima, T. Shinagawa, T. Kuwata, J. Nakata, T. Minegishi, K. Takanabe, K. Domen, *Scientific report* **2016**, *6*, 24633.

[63] M. R. Singh, E. L. Clark, A. T. Bell, *Phys. Chem. Chem. Phys.* **2015**, *17*, 18924-18936.

[64] U. Babic, M. Suermann, F. N. Büchi, L. Gubler, T. J. Schmidt, *J. Electrochem. Soc.* **2017**, *164*, F387-F399.

[65] J. Rodríguez, S. Palmas, M. S.-Molina, E. Amores, L. Mais, R. Campana, *Membranes* **2019**, *9*, 129.

[66] H. Ito, T. Maeda, A. Nakano, A. Kato, T. Yoshida, *Electrochimica Acta* **2013**, *100*, 242-248.

[67] K. Obata, L. Stegenburga, Y. Zhou, K. Takanabe, *ACS Sustainable Chem. Eng.* **2019**, 7, 7241-7251.

[68] P. Jovanovič, N. Hodnik, F. Ruiz-Zepeda, I. Arčon, B. Jozinović, M. Zorko, M. Bele, M. Šala, V. S. Šelih, S. Hočevar, M. Gaberšček, *J. Am. Chem. Soc.* **2017**, *139*, 12837-12846.

[69] O. Kasian, J.-P. Grote, S. Geiger, S. Cherevko, K. J. J. Mayrhofer, *Angew. Chem. Int. Ed.* **2018**, *57*, 1-5.

[70] A. Buttler, H. Spliethoff, *Renew. Sustain. Energy Rev.* **2018**, *82*, 2440-2454.

[71] X. Wang, W. Li, Z. Chen, M. Waje, Y. Yan, *J. Power Sources* **2006**, *158*, 154-159.

[72] S. Zhang, X. Yuan, H. Wang, W. Mérida, H. Zhu, J. Shen, S. Wu, J. Zhang, *Int. J. Hydrogen Energy* **2009**, *34*, 388-404.

[73] M. W. Kanan, D. G. Nocera, *Science* **2008**, *321*, 1072-1075.

[74] M. Huynh, D. K. Bediako, D. G. Nocera, *J. Am. Chem. Soc.* **2014**, *136*, 6002-6010.

[75] C. Costentin, D. G. Nocera, *Proc. Natl. Acad. Sci*. 2017, 114, 13380-13384.

[76] M. W. Kanan, Y. Surendranath, D. G. Nocera, *Chem. Soc. Rev.* **2009**, *38*, 109-114.

[77] Y. Surendranath, D. A. Lutterman, Y. Liu, D. G. Nocera, *J. Am. Chem. Soc.* **2012**, *134*, 6326-6336.

[78] N. Danilovic, R. Subbaraman, K.-C. Chang, S. H. Chang, Y. J. Kang, J. Snyder, A. P. Paulikas, D. Strmcnik, Y.-T. Kim, D. Myers, V. R. Stamenkovic, N. M. Markovic, *J. Phys. Chem. Lett*. **2014**, *5*, 2474-2478.

[79] A. Angulo, P. van der Linde, H. Gardeniers, M. Modestino, D. F. Rivas, *Joule* **2020**, *4*, 555-579.

[80] T. Shinagawa, M. T.-K. Ng, K. Takanabe, *Angew. Chem. Int. Ed.* **2017***, 56,* 5061-5065.

[81] M. Görlin, M. Gliech, J. F. de Araújo, S. Dresp, A. Bergmann, P. Strasser, *Catal. Today* **2016**, *262*, 65-73.

4. Producing pure hydrogen by near-neutral pH water electrolysis at high rates and elevated temperatures

Near-neutral pH water electrolysis driven by renewable electricity can reduce the costs of clean hydrogen generation, but its low efficiency and gas crossover in industrially relevant conditions remains a challenge. I show here that electrolyte engineering can suppress the crossover of dissolved gases such as O_2 by regulating their diffusion flux. In addition, a hydrophilized mechanically stable glass sheet was found to block the permeation of gas bubbles further enhancing the purity of evolved gas from water electrolysis. This sheet had a lower resistance than conventional diaphragms such as Zirfon due to its high porosity and small thickness. A saturated K-phosphate solution at pH 7.2 was used as an electrolyte together with the hydrophilized glass sheet as a gas-separator. This led to a near-neutral pH water electrolysis with 100 mA cm^{-2} at a total cell voltage of 1.56 V with 99.9% purity of produced H_2.[c]

4.1. Introduction

Renewable energy is critical for sustainability, but its large-scale implementation is hampered by the low energy density and spatiotemporal fluctuations of renewable energy sources. In this context, electrocatalytic processes have worldwide interest because they can convert renewably-generated electric power into chemical energy. Using ubiquitous water as a reactant, water electrolysis produces green hydrogen—a core chemical substance in industry. However, the penetration of hydrogen in the current market remains low because it has higher production costs than fossil-fuel-based counterparts.[1] Given that the cost of electricity generated from renewable energy such as solar photovoltaics (PV) and wind has rapidly decreased,[2] a reduction in the system costs is likely critical to the widespread use of green hydrogen in the future.

Nevertheless, further system cost reduction of conventional electrolyzers that are operational at extremely acidic or alkaline pH conditions remains a huge challenge.[3,4] Such pH conditions are critical to maximizing the overall cell efficiency by minimizing the kinetic overpotential and ohmic losses in polymer electrolyte membrane (PEM) or alkaline water electrolyzers.[5] One effort in this direction is to develop a electrolysis cell employing bipolar membrane (BPM) comprising a cation exchange membrane (CEM) and an anion exchange membrane (AEM). The BPM can set acidic and alkaline environments for the hydrogen evolution reaction (HER) and the oxygen evolution reaction (OER), respectively, thus further decreasing the kinetic losses.[6] An efficient BPM requires catalysts that facilitate H_2O dissociation at the interface between the AEM and CEM such as IrO_2[6] for the efficiency improvement. Another effort pressurizes the electrolysis cell whereby the produced gas is already pressurized, and the subsequent compression processes can be skipped.[4,7,8] However, the associated cost reduction is accompanied by a decrease in gas purity; e.g., the impurity of H_2 generated by water electrolysis at 100 mA cm^{-2} increased from 0.1% at 1 bar to 0.6% at 20 bar when using Zirfon—a porous diaphragm for the most prevalent water electrolyzer.[9] Furthermore, electrolyzers employing extreme pH conditions suffer from highly corrosive environments making it necessary to use expensive corrosion-tolerant materials and increasing the system cost. These drawbacks underscore the need for electrolyzers that are operational in milder conditions compatible with the deployment of renewable energy generation on a large scale.

As a non-corrosive reaction medium, near-neutral pH aqueous solution has recently emerged as a next-generation electrolyte. The last decade has witnessed tremendous progress in understanding and improving near-neutral pH water electrolysis. Initially, both half-reactions of the HER and OER were found to suffer from a build-up of local pH gradients under unbuffered near-neutral pH conditions.

This leads to an increased concentration overpotential.[10-14] Introducing buffer substances into electrolytes at near-neutral pH thus improved electrocatalytic performance[15,16] plausibly by preventing the local pH shifts.[13,17-19]

Another role of the added substance was suggested in previous studies. A combined experimental and theoretical investigation showed that the electrocatalytic HER rate was largely determined by the mass-transport of the buffer substance functioning as a proton carrier.[17] This finding was corroborated in another study, which reported that enlarging the mass-transport flux of the buffer substance via optimization of electrolyte properties improved electrocatalytic performance.[20] For instance, a highly concentrated aqueous phosphate buffer at near-neutral pH and elevated temperatures was used to minimize the losses associated with mass-transport.[20] In fact, electrocatalytic performance of near-neutral pH in such electrolytes was demonstrated to be comparable to those in an alkaline pH environment using a model Pt cathode and a IrO$_x$ anode at 10 mA cm^{-2}.[20] Efficiently achieving higher reaction rates remains a main challenge of such devices. This calls for further research efforts in this direction.

In addition to the development of electrolyte and electrode for improved performance, industrial deployment of the near-neutral pH water electrolysis requires research efforts in direction of efficient separation of produced gasses compatible with such conditions. Without these separators, the resulting gases can crossover and reach the counter electrode, thus causing back reactions, i.e., the oxygen reduction reaction (ORR) or the hydrogen oxidation reaction (HOR). The ORR is a particularly important issue because active catalysts for the HER such as Pt[21-24] and other metals[25-30] also show good ORR performances. Conventional alkaline water electrolyzers use Zirfon as a gas-separator, which consists of ZrO$_2$ on a polymeric basis.[31] Electrolyzers in a membrane electrode assembly (MEA) configuration employ solid polymer electrolyte (SPE) as a separator. For example, a Nafion membrane made of a perfluorosulfonic acid polymer for PEM water electrolyzer[32] and various types of membranes are made of polyethersulfone polymers with quaternary ammonium groups for AEM water electrolyzers.[33] These separators are the most prevalent for electrolyzers because of their high chemical stability, mechanical strength, thermal stability, and conductivity. However, they cannot simply be employed at near-neutral pH because of the substantially large *iR*-loss under such conditions. Indeed, the resistance of 0.10 Ω in 7.0 mol kg^{-1} KOH increased by nearly 5-fold in a representative K-phosphate solution (**Table 4.1**) due to the lower conductivity of K-phosphate solutions than the 7.0 mol kg^{-1} KOH.

Table 4.1. Measured resistivities and resistances of Zirfon in 4.1 mol kg^{-1} (saturated K-phosphate solution) or 7 mol kg^{-1} KOH solution at 100 °C under Ar bubbling. The resistivities were measured by PEIS (see **Figure 4.1** for more detail). The pH of the K-phosphate solutions was adjusted to 7.2 at 25 °C prior to each experiment.

Electrolyte	Resistivity / Ω m	Resistance / Ω
7.0 mol kg^{-1} KOH	0.02	0.10
4.1 mol kg^{-1} K-phosphate	0.09	0.48

(a)

(b)
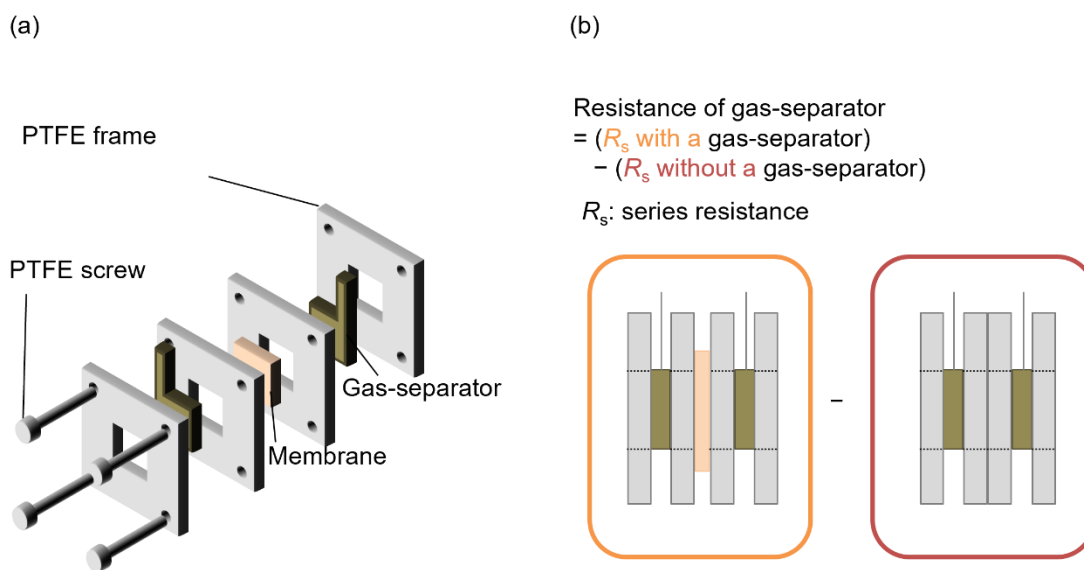
Figure 4.1. Cell configuration to determine the resistivity of gas-separators. (a) An aerial view of the cell. (b) Schematic description of measurement method for the resistivity.

There have been various strategies reported for gas separation of near-neutral pH water electrolyzers. One pillar of these strategies is a membrane-free configuration.[34-36] The membrane-less electrolyzers rely on the separation of product gases via a flow of electrolytes.[34,36] More specifically, the configuration of flow-by electrodes requires the electrode surfaces to be placed in parallel, and the electrolyte flows between the electrodes. This design prevents transport of generated H$_2$ and O$_2$ to the opposite electrodes, thus achieving less gas crossover.[34-36] However, this concept

has trade-offs in terms of efficiency, current density, purity of generated gases, and electrode size, e.g., a wide gap between electrodes would increase gas purity but decrease the efficiency.[34] For instance, the cell total voltage reached ca. 2.3 V at a mere current density of 71.5 mA cm^{-2} when achieving > 99% purity of evolved H_2 gas in such a system.[37]

Another strategy employs the concept of electrolyte engineering. In general, the mass-transport flux of dissolved gases is governed by their solubility and diffusion coefficients according to the Fick's law of diffusion.[38] This strategy uses an observation that these properties concurrently decreased with increasing molality of the electrolyte solutions.[5] By employing a concentrated electrolyte (> 1.0 mol kg^{-1}), a previous study demonstrated selective HER in the presence of O_2 at 298 K using a model Pt electrode.[39] Existing theory predicts that—while the diffusion coefficient of generated gases increases at elevating temperatures—the solubility of generated gases decreases.[40,41] This expected trade-off relationship casts a question as to whether this strategy is applicable to the electrolysis system at industrially relevant temperatures of 80 °C or above. In addition, this strategy cannot avoid the crossover of evolved gas bubbles necessitating the use of an additional gas-separator.

Collectively, the industrial deployment of near-neutral pH water electrolysis thus requires the development of a product separation system for both dissolved gases and gas-bubbles while efficiently achieving an industrially relevant reaction rate of 100 mA cm^{-2} or above. Here, I report a near-neutral pH water electrolysis system that employs (1) electrolyte engineering strategy to suppress the crossover of dissolved gases and (2) thin porous glass-fiber diaphragm that avoids the crossover of produced gas bubbles. Obviously, the glass cannot be utilized for alkaline electrolyzer whose applications are distinctively realized at neutral pH conditions. Quantification of diffusion fluxes of molecules in the rotating disk electrode (RDE) configuration demonstrated the successful regulation of crossover of dissolved gases via electrolyte engineering at increased temperature. The porosity and thickness of the diaphragm was analyzed suggesting the gas-separation function of the glass sheet with a concurrent lower iR drop. Lastly, near-neutral pH water electrolysis was demonstrated achieving 100 mA cm^{-2} at a total cell voltage of 1.56 V and 100 °C with H_2 purity of 99.9% corresponding to the cell efficiency of 94% with respect to the thermoneutral voltage of 1.47 V.

4.2. Experimental method

Chemicals. The following chemicals were used: $H_2Cl_6Pt_6 \cdot H_2O$ (99.9%, FUJIFILM Wako Pure Chemical Corporation), KOH (ACS reagent, Sigma Aldrich), H_3PO_4 (ACS reagent, Sigma-Aldrich),

HClO$_4$ (assay 70%, Sigma-Aldrich), Na$_3$IrCl$_6$·xH$_2$O, H$_2$C$_2$O$_4$ (≥ 99%, Sigma-Aldrich), Na$_2$CO$_3$·H$_2$O (≥ 99.5%, Sigma-Aldrich), H$_2$SO$_4$(ACS reagent, Sigma Aldrich), H$_2$O$_2$ (for atomic absorption spectrochemical analysis, FUJIFILM Wako Pure Chemical Corporation), HCl (ACS reagent, Sigma-Aldrich), HNO$_3$ (SAJ first grade, Sigma-Aldrich), KCl (99.999%, Sigma-Aldrich), Ni(NO$_3$)$_2$·6H$_2$O (97.0%, FUJIFILM Wako Pure Chemical Corporation), Fe(NO$_3$)$_3$·9H$_2$O (99.0%, FUJIFILM Wako Pure Chemical Corporation), urea (ACS reagent, Sigma-Aldrich), as well as GS/A, GS/C, and GS/F (denoted as GS-16, GS-12, GS-07, respectively) microfiber glass sheets (Cytiva), Zirfon pearl UTP 500 (Agfa).

Electrolyte preparations. K-phosphate solutions were employed as an electrolyte. Concentrated KOH solutions were mixed into concentrated H$_3$PO$_4$ aqueous solution to obtain targeted concentration of K-phosphate solutions at pH 7.2. The molality in this study represents that of phosphate ions (the sum of H$_2$PO$_4^-$ and HPO$_4^{2-}$). The detailed protocol is the same as that described in my previous study.[20]

Determination of gas-separator electrolyte properties. The resistivity of electrolyte solution was assessed by potentiostatic electrochemical impedance spectroscopy (PEIS) using a 16-channel research-grade potentiostat system (VMP3, BioLogic Science Instruments). The measurement was performed in a two-electrode system with two Pt wires separated by 2.0 cm using an electrochemical cell with cell constant K$_{cell}$ of 0.6 cm^{-1} that was determined using 1.0 mol kg^{-1} KCl solution as a reference. The viscosity of K-phosphate solutions was measured with a viscometer (SVM3001, Anton Paar) at varying concentrations and temperatures. The resistance of the gas-separators was determined by measuring the resistance of electrode assembly with and without gas-separators, using a cell configuration illustrated in **Figure 4.1**. First, the series resistance R_s of electrode gas-separator assembly was measured by PEIS at an open-circuit voltage. The distance between electrodes in the assembly equaled the thickness of separator L_s. Second, the R_s electrodes separated by L_s was measured by potentiostatic electrochemical impedance spectroscopy (PEIS) at an open-circuit voltage. Finally, the resistance of separator, R_{GS}, was determined based on the following equation:

$$R_{GS} = \left(R_s \text{ with a gas-separator}\right) - \left(R_s \text{ without a gas-separator}\right) \qquad (4\text{-}1)$$

The resistivity of gas-separator was calculated by dividing R_{GS} by its thickness.

Hydrophilization of glass sheets. Hydrophilization of glass sheet was conducted by immersing sheets in piranha solutions for 30 min.[42] The piranha solutions were prepared by mixing 12 mL of 75% H$_2$SO$_4$ solution and 4 mL 30% H$_2$O$_2$ solution. After immersion, the sheets were cleaned with

ultrapure water several times and then dried in air. The series resistances before and after this hydrophilization on GS-16 are shown in **Figure 4.11**.

Electrode preparation. The IrO_x electrodes were fabricated by electrochemical deposition following a reported protocol[43] on a titanium felt substrate. The pH level of the deposition bath containing 0.4 mM of $Na_3IrCl_6 \cdot xH_2O$ and 2 mM of $H_2C_2O_4$ was adjusted to 10 by adding $Na_2CO_3 \cdot H_2O$ and held at 35 °C for four days prior to the deposition. A Ti felt (ST/Ti/20/150/67m NIKKO TECHNO) with a geometric size of 1×1 cm^2 was immersed in 35% HCl aqueous solutions for 30 min to remove surface oxides. This was then washed by ultrapure water several times and immediately used. The electrochemical deposition was conducted using a three-electrode configuration with Pt mesh (Nilaco) and Hg/Hg_2Cl_2 (saturated with KCl) as the counter and reference electrodes, respectively. IrO_x was deposited onto the felt as a working electrode by immersing the felt in the prepared deposition bath and applying a constant current density of 140 μA cm^{-2} for 70 ks. Cyclic voltammogram (CV) using each fabricated electrode was recorded in 0.1 mol kg^{-1} $HClO_4$ to ensure identical properties. A platinized platinum (Pt/Pt mesh) electrode was fabricated by electrochemical deposition following a reported recipe[44,45] with a Pt mesh (Nilaco) as the substrate. Prior to electrochemical deposition, the Pt mesh was immersed in aqua regia for 1 min. (The aqua regia was prepared by mixing HCl and HNO_3 at a volume ratio of 3:1). The mesh was then washed with copious amount of ultrapure water. Subsequently, the electrochemical deposition was conducted using a three-electrode configuration with Pt mesh (Nilaco) and Hg/Hg_2Cl_2 (saturated with KCl) as the counter and reference electrodes, respectively. Platinum was deposited onto the platinum mesh as a working electrode by immersing the mesh in a deposition bath and applying a constant potential of -0.1 V vs. Hg/Hg_2Cl_2 for 15 min. CV used each fabricated electrode and was recorded at 0.1 mol kg^{-1} $HClO_4$ to ensure identical properties. A $NiFeO_x$ electrode was next prepared by the hydrothermal synthesis following the literature.[46] Prior to the synthesis, the Ni foam was washed by immersing the foam in 0.1 mol kg^{-1} HCl, ultrapure water and ethanol sequentially for 5 min each. The Ni foam was then transferred to a 100-mL Teflon-lined stainless-steel autoclave together with 80 mL of solution containing 1 mmol of $Ni(NO_3)_2 \cdot 6H_2O$, 1 mmol of $Fe(NO_3)_3 \cdot 9H_2O$, and 5 mmol of urea. These were heat-treated at 120 °C for 12 h. The autoclave was then naturally cooled to room temperature.

Electrochemical determination of dissolved gas diffusion fluxes. A diffusion-limited current density j_{lim} was experimentally determined using a rotating disk-electrode (RDE) configuration in three electrode system. Prior to testing, a polycrystalline Pt disk with a 3.0 mm diameter (BAS, Inc) was first polished with a 1-μm diamond and then with 0.05-μm alumina (both purchased from BAS,

Inc.). The surface was further electrochemically treated by cyclic voltammetry in 1.0 mol L^{-1} $HClO_4$. A Hg/Hg_2Cl_2 (saturated with KCl) and a Pt wire were used as the reference and counter electrodes, respectively. Before and during all measurements, Ar (99.9999%), H_2 (99.9999%), or O_2 (99.9995%) gas was continuously supplied to the cell. The cyclic voltammetry (CV) was conducted at disk-rotation speeds of 3600 rpm and at a scan rate of 1 mV s^{-1}. The current-potential relationship described in this study was iR-corrected using a resistance value determined by the PEIS at 1 kHz with 10 mV amplitude. The cell was equipped with a jacket (Water-Jacketed glass cell; BAS Inc.), and its temperature was controlled by an external equipment (NCB-1210, Eyela). All current densities are expressed in terms of the geometric electrode surface area. The j_{lim} of the oxygen reduction reaction (ORR) was determined by taking the difference of current densities between in O_2 and Ar atmospheres at 0.4 V vs. reversible hydrogen electrode (RHE). Likewise, the j_{lim} of the hydrogen oxidation reaction (HOR) was determined by comparing the CVs in H_2 and Ar atmosphere.

Determination of gas purity at the cell outlet. Purity of evolved gases via water electrolysis was determined by measuring the gas composition at the cell outlet. Electrolysis was conducted in two-electrode systems, and the home-made polytetrafluoroethylene (PTFE) cell is shown in **Figure 4.12a**. The cell separates the anodic and cathodic chambers with gas-separators sandwiched in between. Both chambers were filled with ca. 4 mL of electrolyte solutions. The fabricated IrO_x/Ti felt and Pt/Pt mesh with the geometric surface area of 10 mm × 10 mm were used as the anode and cathode, respectively. A glass sheet was placed between the chambers with a geometric surface area of 0.79 cm^2 in a circular shape with a diameter of 1 cm. Ar (99.9999%) was used as a carrier gas, which was supplied to the cell headspace at a flow rate of 0.5 mL min^{-1}. The composition of gas outlet was determined using on-line gas chromatography (GC; Shimadzu Cooperation, GC-2014) with Shincarbon-ST column (SHINWA CHEMICAL INDUSTORIES LTD.) equipped with thermal conductivity detector (TCD). The system temperature was controlled by using silicone rubber heating belt. All current densities are expressed in terms of the geometric electrode surface area.

Half-cell electrocatalytic testing. Electrocatalytic measurements for the half-cell reactions, namely the hydrogen evolution reaction (HER) and the oxygen evolution reaction (OER), were conducted in a three-electrode system. The Pt/Pt mesh or fabricated IrO_x/Ti felt with the geometric surface area of 10 mm × 10 mm were used as the working electrode for the HER or OER testing, respectively, with a Hg/Hg_2Cl_2 (saturated with KCl) reference electrode and a Pt wire counter electrode. Before and during all measurements, H_2 (99.9999%) or O_2 (99.9995%) gas was continuously supplied to the cell for the HER or OER testing. The CV was performed at 1 mV s^{-1}. The current-potential relationship

described in this study was *iR*-corrected using a resistance value determined by the PEIS at 1 kHz with 10 mV amplitude. The employed cell is shown in **Figure 4.13**, and its temperature was controlled by placing the cell in an oil bath. All current densities are expressed in terms of the geometric electrode surface area.

Electrolysis testing. Water electrolysis testing was conducted in a zero-gap configuration as illustrated in **Figure 4.13**. The configuration employed the IrO_x/Ti felt anode (10×10 mm^2) and Pt/Pt mesh cathode (10×10 mm^2) sandwiching the gas separator (12×12 mm^2). These were fixed using a PTFE frame and screw. The electrode-separator assembly was placed in a glass cell, and its temperature was controlled by an oil bath. Chronopotentiometry (CP) was performed, and the outlet gas composition was determined by GC-TCD using Ar (99.9999%) carrier gas at a flow rate of 100 mL min^{-1}. All current densities were expressed in terms of the geometric electrode surface area.

Characterizations. Surface chemical states of the IrO_x/Ti felt anode and the Pt/Pt mesh cathode were characterized by X-ray photoelectron spectroscopy (XPS; JPS-9010MC, JEOL) using Mg Kα radiation as shown in **Figure 4.19**. The binding energy scale was calibrated using the C 1s peak at 285.0 eV. The morphologies of the glass fiber sheets were characterized by scanning electron microscopy (SEM; JSM-IT800, JEOL) as shown in **Figure 4.8**.

4.3. Results and discussion

Successful water electrolysis suppresses back reactions, HOR and ORR. These back reactions during water electrolysis can be triggered by supply of the reactant H_2 and O_2 to the anode and cathode, respectively, as either dissolved gas or gas bubbles. This study aims (1) to suppress the crossover of evolved H_2 and O_2 molecules dissolved in the solution by an electrolyte engineering approach and (2) to circumvent the transport of evolved gas bubbles to the counter electrode via a porous glass diaphragm that could not be employed in the corrosive alkaline electrolyzers. Subsequently, a near-neutral pH aqueous water electrolysis was demonstrated at elevated temperatures as well as industrially-relevant current densities for pure H_2 production with comparable efficiency to a conventional water electrolyzer.

4.3.1. Regulation of dissolved gas crossover via electrolyte engineering at elevated temperatures

The concentration gradient of evolved gas molecules drives its crossover during water electrolysis, and Fick's law of diffusion determines its flux[38]:

$$J = -D\frac{C^*}{x},\qquad(4\text{-}2)$$

Where D is the diffusion coefficient, C^* is the concentration of an evolved gas, and x is the thickness of the diffusion layer. Rigorous quantification of the flux requires the determination of a diffusion-layer thickness. Thus, RDE was adopted in which the mass-transport flux of forced convection is obtained via the following Levich equation:[47]

$$j_{\text{lim}} = 0.62\text{nF}\varpi^{1/2}v^{-1/6}D^{2/3}\Delta C,\qquad(4\text{-}3)$$

where n defines the number of involved electrons, F is Faraday's constant, ω defines the disk rotation speed, v is the solution kinematic viscosity, and ΔC represents the difference in the reactant concentrations between the surface and bulk. With these equations, the diffusion layer thickness in the RDE configuration is dictated by:

$$\delta x = 1.62D^{1/3}v^{1/6}\varpi^{-1/2}.\qquad(4\text{-}4)$$

By employing the RDE configuration, below the diffusion-limited current density j_{lim}, or Levich current density, was assessed at various temperatures and molalities of electrolyte solutions. Potassium phosphate (K-phosphate) solutions at pH 7.2 (at 25 °C) were adopted as a model electrolyte in which a model Pt cathode and IrO_x anode previously achieved efficiency of water electrolysis comparable to commercialized water electrolyzers though at a low rate of 10 mA cm^{-2}.[20]

Analyzing cyclic voltammograms (CVs) over a polycrystalline Pt disk electrode under Ar, H_2, or O_2 bubbling allowed for experimental determination of diffusion fluxes. **Figure 4.2a** shows representative CVs at 25 °C recorded at 0.5, 1.0, and 1.5 mol kg^{-1}, and saturated (2.5 mol kg^{-1}) K-phosphate solutions under those gas atmospheres. A CV consistent with the literature was obtained in a solution of 0.5 mol kg^{-1} K-phosphate with Ar bubbling. Specifically, a cathodic event was observed at ca. 0.0-0.3 V vs. reversible hydrogen electrode (RHE) due to Pt-H formation followed by its desorption during the anodic scan in the same potential window.[48,49]
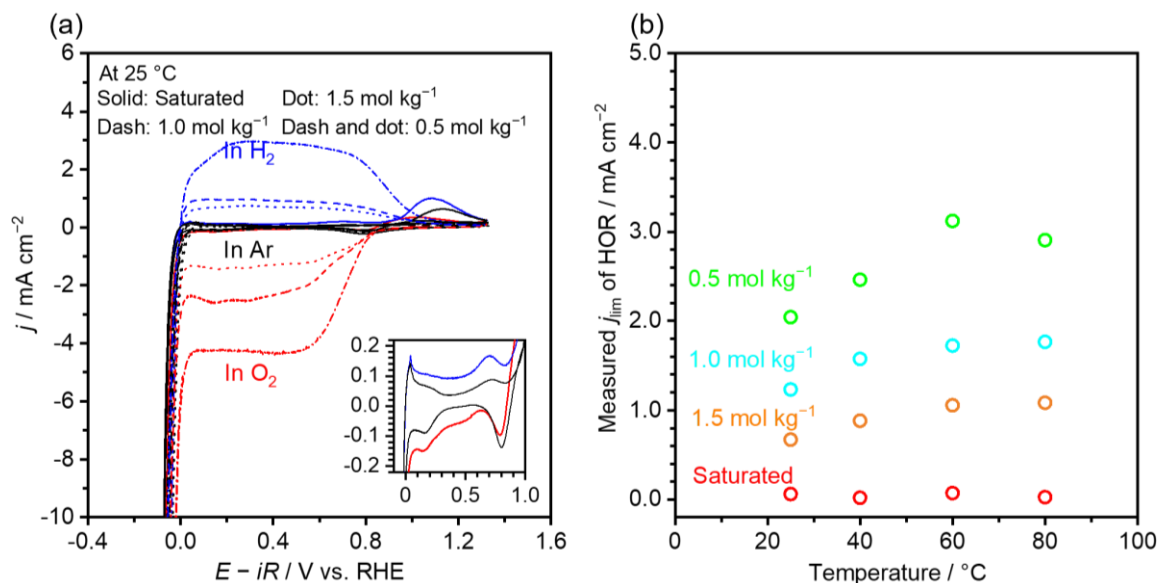
Figure 4.2. Determination of gas molecule cross-over as oxygen reduction reaction (ORR) and hydrogen oxidation reaction (HOR). (a) Representative cyclic voltammetry (CV) using a polycrystalline Pt disk electrode under different gas atmospheres (Ar, H_2 or O_2) in 0.5, 1.0, 1.5 mol kg^{-1} and saturated (2.5 mol kg^{-1}) K-phosphate solutions at a scan rate of 50 mV s^{-1} and 3600 rpm at 25 °C. The insets show the magnified views. (b) Measured diffusion-limited current density j_{lim} of HOR at various solution molality of 0.5, 1.0, 1.5 mol kg^{-1}, and saturated as a function of temperature. The j_{lim} values were adopted at 400 mV vs. reversible hydrogen electrode (RHE) of the CVs for both the HOR and ORR. The pH of the K-phosphate solutions was adjusted to 7.2 at 25 °C prior to each experiment.
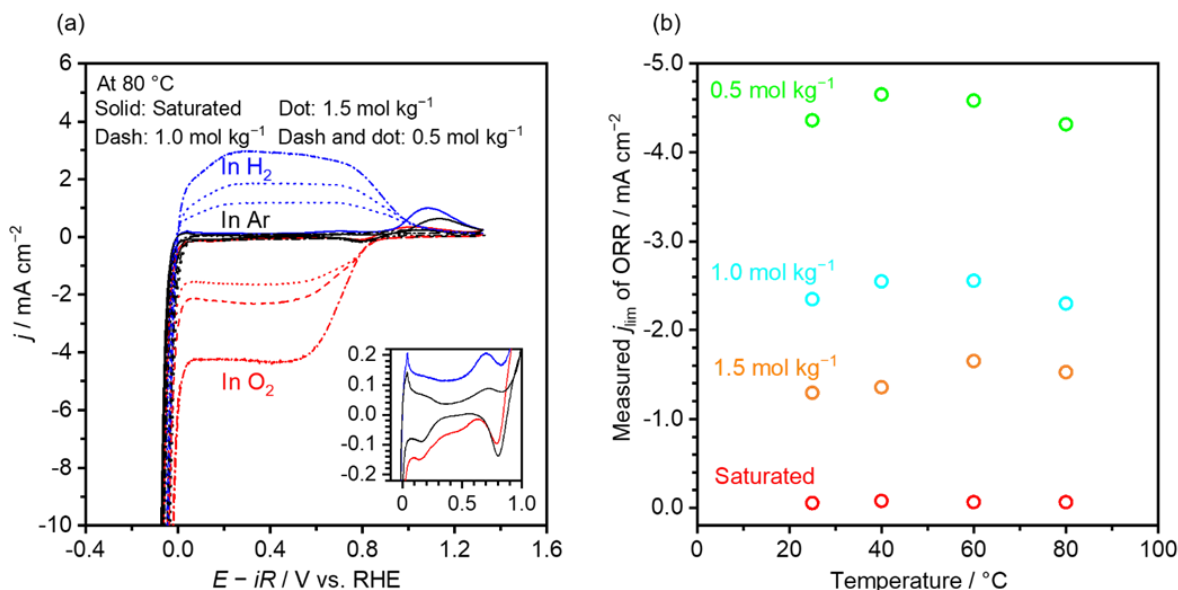
Figure 4.3. Determination of gas molecule crossover as oxygen reduction reaction (ORR) and hydrogen oxidation reaction (HOR) (a) Representative cyclic voltammetry (CV) using a polycrystalline Pt disk electrode under different gas atmospheres (Ar, H_2 or O_2) in 0.5, 1.0, 1.5 mol kg^{-1} and saturated (3.6 mol kg^{-1}) K-phosphate solutions at a scan rate of 50 mV s^{-1} and 3600 rpm at 80 °C. The insets show the magnified views. (b) Measured diffusion-limited current density j_{lim} of ORR at various solution molality of 0.5, 1.0, 1.5 mol kg^{-1}, and saturated as a function of temperature. The j_{lim} values were adopted at 400 mV vs. reversible hydrogen electrode (RHE) of the CVs for both the HOR and ORR. pH value of the K-phosphate solutions was adjusted to 7.2 at 25 °C prior to each experiment.

At potentials more positive than ca. 0.9 V vs. RHE, oxidation currents appeared that originated from Pt-OH or Pt-O formation. These were subsequently reduced during the cathodic scan below 1.2 V vs. RHE.[48,49] The substantial increase in the current density below 0 V vs. RHE was due to the HER. In a H_2 atmosphere, anodic current densities sharply increased above 0 V vs. RHE, thus originating from HOR.[10] In the O_2 atmosphere, cathodic current densities were apparent below ca. 0.9 V vs. RHE, and were assigned to the ORR.[25] The redox events were apparent in a saturated electrolyte as shown in the **Figure 4.2a** inset although at smaller current densities. Critically, the current densities of both HOR and ORR decreased with increasing molality, consistent with a previous study.[39]

Taking current densities at 0.4 V vs. RHE as a representative, the j_{lim} of the ORR was found to be -4.4 mA cm^{-2} in 0.5 mol kg^{-1} K-phosphate solutions, which decreased to -0.08 mA cm^{-2} in saturated K-phosphate solutions. Likewise, the j_{lim} for the HOR was 2.0 and 0.06 mA cm^{-2} in 0.5 mol kg^{-1} and saturated K-phosphate solutions, respectively. The j_{lim} of HOR was smaller than the j_{lim} of ORR because the former requires transfer of 2 electrons while the latter involves a 4-electron transfer.

Theoretically, the diffusion flux follows **Equations 4-2** and **4-3**,[47] which is thus governed by the diffusion coefficient and solubility of gas molecules. In the framework of the Stokes-Einstein model, the diffusion coefficient is determined by the following equation:

$$D = \frac{kT}{3\pi d\mu} . \qquad\qquad (4\text{-}5)$$

The gas solubility was reported to follow the empirical law at 25 °C;[40,41]

$$\log\left(\frac{c_{G,0}}{c_G}\right) = \sum (h_i + h_G)c_i , \qquad\qquad (4\text{-}6)$$

in which $C_{G,0}$ is the solubility of gas in pure water, C_G is the solubility of gas in solution, and h is the constant for ion(h_i) and gas(h_G), respectively; C_i is the ion concentration. The latter equation was extended to values below 90 °C:

$$h_G = h_{G,0} + h_T(T - 298.15) , \qquad\qquad (4\text{-}7)$$

in which $h_{G,0}$ is the h_G value at 25 °C, and h_T is the gas-specific parameter for the compensation of temperature change. Theoretical j_{lim} was computed using these equations (see **Table 4.2** for experimentally determined viscosity, **Figure 4.4** for calculated diffusion coefficient and gas solubility). This was compared with experimentally obtained values. Remarkably, the parity plot in **Figure 4.5** shows that the computational and experimental values agree at 25 °C, thus validating the applicability of these equations for HOR and ORR consistent with the literature.[10] These equations suggest that the diffusion coefficient increases as the temperature increases while the gas solubility decreases. This finding suggests a trade-off relationship between these parameters.

Table 4.2. Viscosity of K-phosphate solutions at pH 7.2. Viscosity of K-phosphate solutions was measured at various temperatures using a viscometer, and pH levels of K-phosphate solutions were adjusted to 7.2 at 25 °C prior to the measurements.

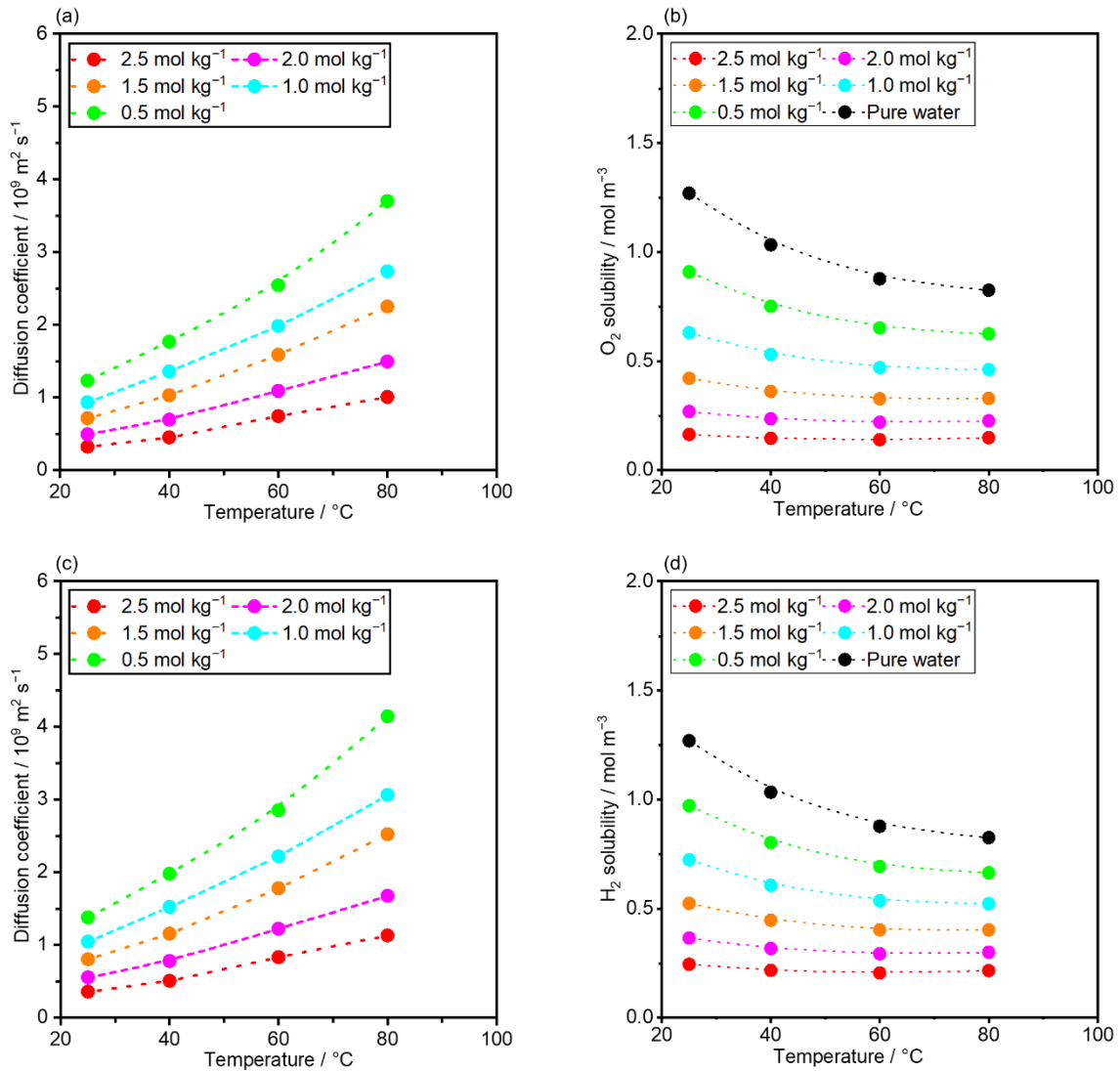| Molality / mol kg^{-1}	Viscosity / mPa s				
	25 °C	40 °C	60 °C	80 °C	100 °C
0.5	0.95	0.69	0.49		
1.0	1.27	0.94	0.67		
1.5	1.87	1.37	0.98		
2.0	2.52	1.89	1.28	0.99	0.80
2.5	3.18	2.85	2.31	1.88	1.58

Figure 4.4. Calculated diffusion coefficient and solubility of O_2 and H_2. (a,c) Diffusion coefficient of (a) O_2 and (c) H_2 calculated using **Equation 4-5** with measured viscosity values in **Table 4.2**. (b,d) Solubility of (b) O_2 and (d) H_2 using **Equations 4-6** and **4-7**.
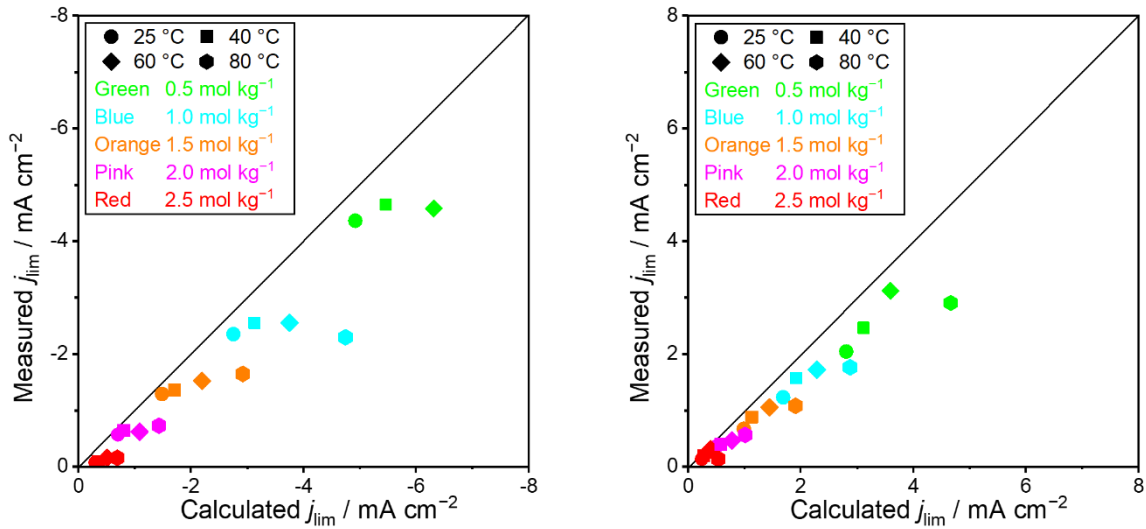
Figure 4.5. Comparison of experimentally and theoretically determined diffusion-limited current density (j_{lim}). The measured j_{lim} of (a) oxygen reduction reaction (ORR) and (b) hydrogen oxidation reaction (HOR) is plotted as a function of calculated j_{lim}. Experimental j_{lim} values were determined by cyclic voltammetry (CV) in a three-electrode system using a polycrystalline Pt rotating disk electrode (RDE) in 0.5, 1.0, 2.0, 2.5 mol kg^{-1}, or saturated K-phosphate at varying temperatures of 25, 40, 60, 80, and 100 °C under (a) O$_2$ or (b) H$_2$ bubbling. The calculated j_{lim} was obtained by using Levich equation (**Equation 4-3**). The pH values of K-phosphate solutions were adjusted to 7.2 at 25 °C prior to the measurements.

My experimental investigation was then extended to elevated temperatures. **Figure 4.3a** shows CVs recorded in the same gas composition as **Figure 4.2a** but at 80 °C as a representative. Similar to the CVs at 25 °C, redox events ascribable to Pt-H formation and desorption as well as Pt oxidation into Pt-O(H) and its reduction were apparent at 80 °C. The j_{lim} for the ORR and HOR was assessed at 0.4 V vs. RHE. Together with j_{lim} values obtained at different temperatures (see **Figure 4.6** for raw CVs), j_{lim} values of the ORR and HOR are now summarized as a function of temperatures in **Figure 4.2b** and **4.3b**, respectively. **Figure 4.2b** and **4.3b** show that the $|j_{lim}|$ of both ORR and HOR initially increased below ca. 40-60 °C with an increase of temperature, which subsequently decreased afterwards regardless of the molalities investigated in the present study. Notably, the experimentally obtained j_{lim} values were found to be substantially smaller than the calculated values above 25 °C for ORR and above 60 °C for HOR (**Figure 4.5**) pointing to overestimation of the diffusion coefficient in the conventional model that does not consider the solute-solute interactions.
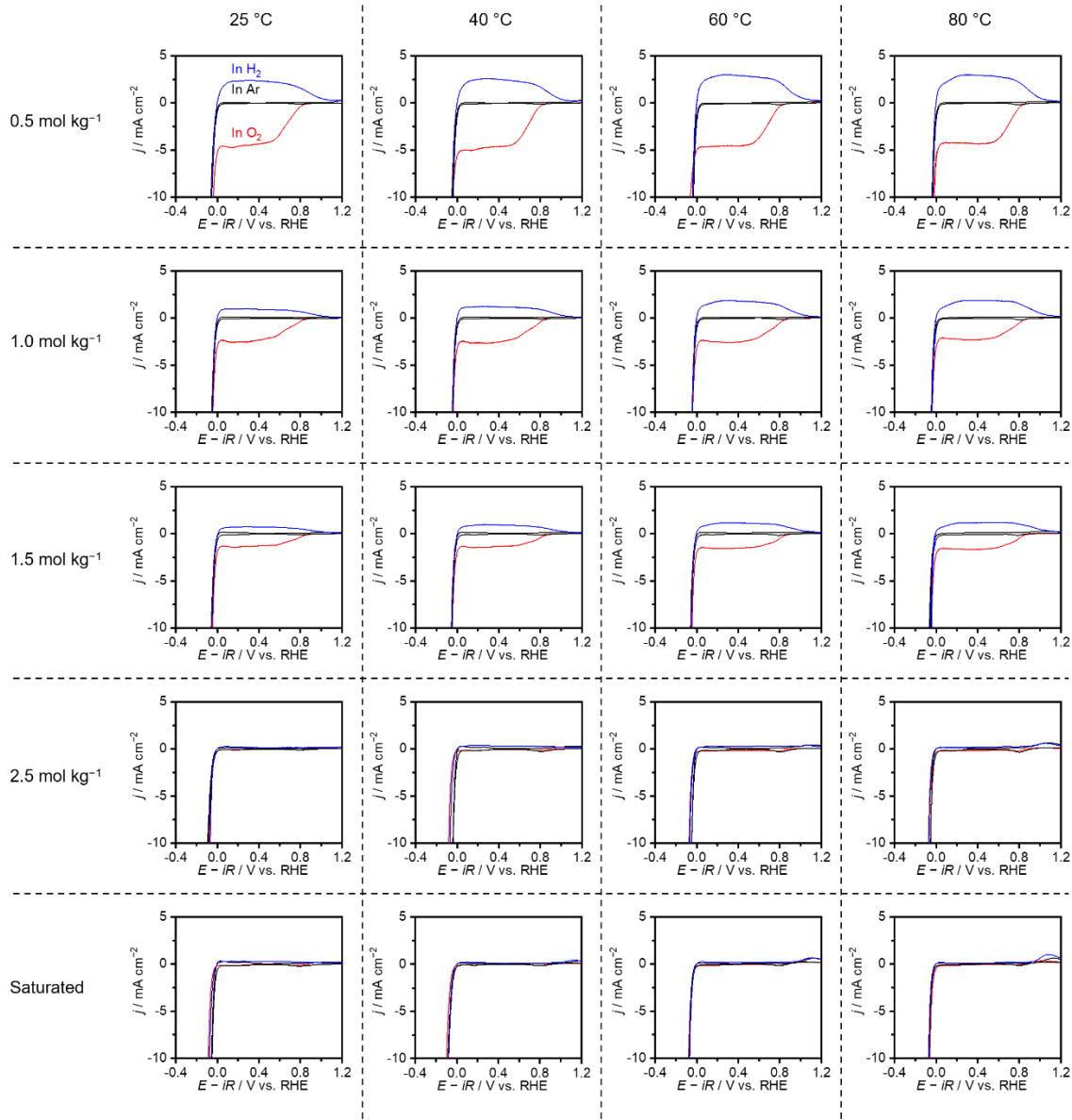
Figure 4.6. Raw linear sweep voltammograms. The measurements were conducted using two polycrystalline Pt RDE at 3600 rpm in 0.5, 1.0, 1.5, 2.5, or saturated K-phosphate at 25, 40, 60, and 80 °C under Ar (black), O_2 (red), or H_2 (blue) atmosphere. The pH levels of solutions were adjusted to 7.2 at 25 °C prior to the measurements.

Critically, the j_{lim} values determined here (**Figure 4.2a** and **4.3a**) show that the crossover fluxes of dissolved gas molecules were largely insensitive to the temperature, e.g., falling in a range of 0.05 to 0.08 mA cm^{-2} for ORR and of 0.02 to 0.07 mA cm^{-2} for HOR in saturated K-phosphate solutions.

This quantity is substantially smaller than the industrially-targeted reaction rate, e.g., 100 mA cm^{-2} and above. Thus, the regulation of molecule crossover via electrolyte engineering would produce high-purity H_2 via near-neutral pH water electrolysis if the crossover of gas bubbles is circumvented.

4.3.2.   Regulation of gas bubble crossover by thin, porous sheet

Regulating the transport of gas bubbles requires additional measures including the use of fluid mechanic forces in membrane-less configuration,[34,36] and the use of physical separator[31-33] as detailed in the **Introduction**. The attainable efficiency at a high rate is limited in the membrane-less configuration,[50] and thus I used a separator in near-neutral pH cells for gas separation. The ideal approach to use the sheet in the near-neutral pH water electrolysis cell would be the zero-gap configuration,[50] in which the anode and cathode sandwich the separator. This configuration requires the separator to be non-conductive.

Table 4.3. Properties of gas-separator. Values of pore size and thickness were obtained from manufacturing companies.[54,55] The porosity for the Zirfon was also obtained from the company,[54] and that for the glass fiber sheets was calculated using the density of the fiber and weight per unit area of the product.[54,56] Costs were obtained from manufacturing companies.[54,55]

Name	Pore radius / μm[54,55]	Thickness / μm[54,55]	Porosity / μm[54-56]	Cost USD m^{-2}
GS-16	1.6	260	93.6	
GS-12	1.2	260	93.6	70
GS-07	0.7	420	94.4	
Zirfon	0.1	500±50	55±10	385

The benign near-neutral pH conditions broaden the option of materials for the separator, which are otherwise impossible in conventional electrolysis cells due to their corrosive nature. Among a variety of candidates, silicon-based materials are an ideal candidate with good earth-abundance and cost-efficiency.[51,52] Hence, SiO_2 was selected as the raw material of the separator. It is

thermodynamically stable at near-neutral pH regions but easily dissolves under the harsh alkaline pH conditions of conventional alkaline water electrolyzers.[53]

Three representative borosilicate glass-fiber sheets (GS) were purchased from Cytiva: GS-07, GS-12, and GS-16 with varying pore radii of 0.7, 1.2, and 1.6, respectively. **Figure 4.7a** shows a photograph and corresponding scanning electron microscopy (SEM) images of GS-16 (see **Figure 4.8** for SEM images of other glass fibers). The glass fiber sheets were woven with glass fibers of several micrometers in diameter (**Figure 4.7a**). **Table 4.3** summarizes the properties of these sheets together with a Zirfon diaphragm[54,55] employed in the alkaline electrolyzers. GS-16 and GS-12 have the same thickness of 260 μm; GS-07 is thicker by 160 μm. Due to the relatively large pore size and smaller thickness, these GSs all have a porosity as high as ca. 94%. This feature contrasts themselves from Zirfon that has a pore radius of 0.1 μm and a porosity of ca. 55%.
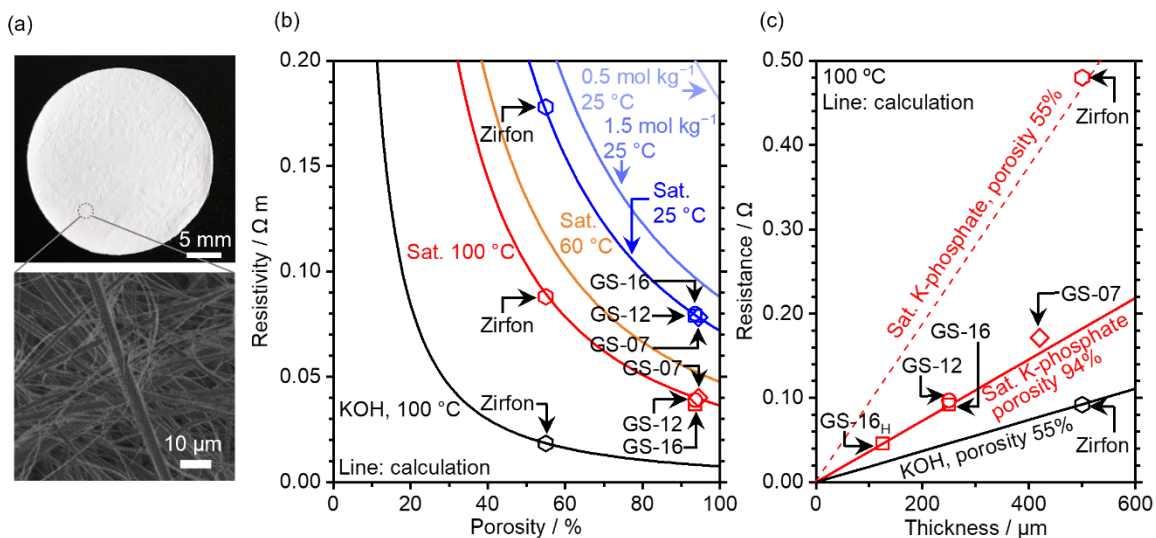
Figure 4.7. Resistivity and resistance of gas-separators in representative electrolyte solutions. (a) A photograph and scanning electron microscopy (SEM) image of GS-16. (b) Resistivity in 0.5, 1.5, and 2.5 (saturated) mol kg^{-1} K-phosphate solutions or 7.0 mol kg^{-1} KOH solutions at 25, 60, or 100 °C. (c) Resistance of glass fiber sheets (GS-16, GS-12, and GS-07) and Zirfon at 100 °C in 4.1 mol kg^{-1} (saturated) K-phosphate solutions or 7.0 mol kg^{-1} KOH solutions. The open symbols denote the values measured by impedance spectroscopy (see **Figure 4.1** for the cell configuration), and lines represent the calculated values. The pH value of the K-phosphate solutions was adjusted to 7.2 at 25 °C prior to each experiment. The GS-16$_H$ with a thickness of 130 μm in the panel (c) was obtained by splitting GS-16 into two pieces (see Experimental for details), and the obtained sheet was subjected to hydrophilization treatment (see the text) and thus labeled with subscript H.
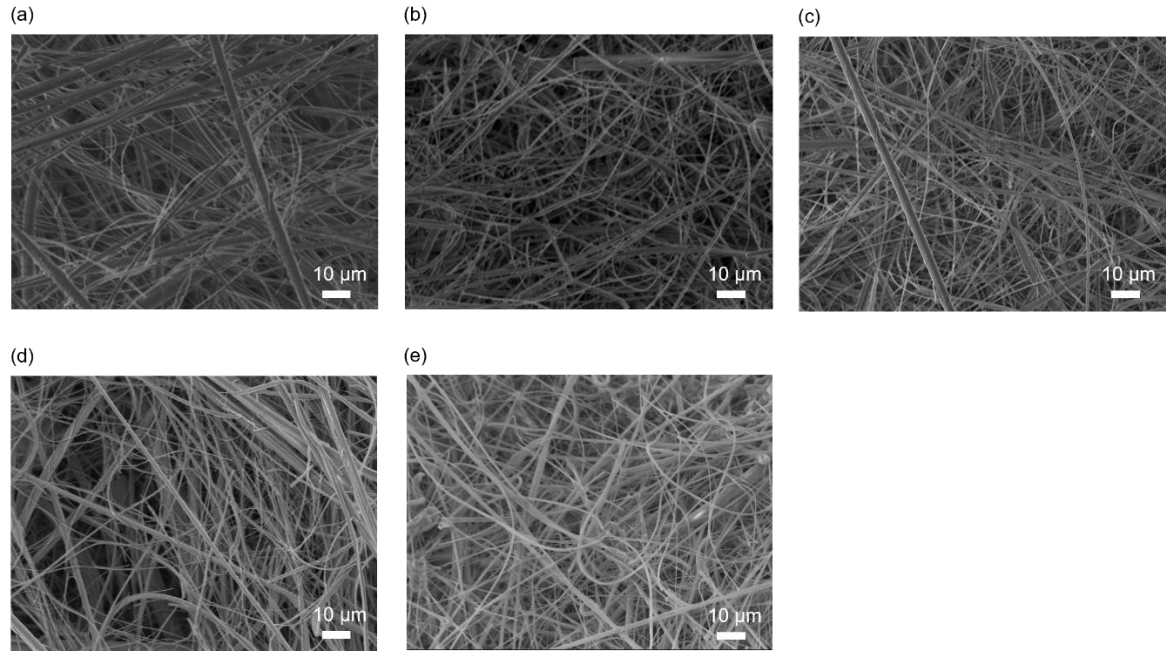
Figure 4.8. Surface morphology of glass fiber sheets. Scanning electron microscopy (SEM) images of (a) GS-16, (b) GS-12, (c) GS-07, and (d) GS-16$_H$ before testing and € GS-16$_H$ after CP testing at 100 mA cm^{-2} for 24 h.

The non-conductive nature of these sheets increases the resistivity, and thus their structure needs to be optimized for lessened *iR* loss and in turn higher cell efficiency. The resistance, *R*, is a function of resistivity and cell constant from a fundamental viewpoint;

$$R = \rho K_{cell}. \qquad (4\text{-}8)$$

The resistivity of a porous medium consisting of spheres is expressed by the following empirical equation:[57-59]

$$\rho = \rho_0 \frac{\tau^2}{\varepsilon}, \qquad (4\text{-}9)$$

in which ρ is the resistivity of the porous medium, ρ_0 is the resistivity of the electrolyte, τ is the tortuosity factor, and ε is the porosity of the medium. In the case of a porous medium consisting of spheres such as Zirfon, τ^2 value is reported as $\varepsilon^{-0.5}$.[59] Therefore, the **Equation 4-9** can be expressed as follows:

$$\rho = \rho_0 \frac{1}{\varepsilon^{1.5}} \,, \tag{10}$$

The cell constant is determined by the following equation:[60]

$$K_{cell} = \frac{l}{A} \,, \tag{11}$$

where l and A are the specific length and cross-sectional area of the electrochemical cell, respectively.[60] Taken together, the resistance is anticipated to be lower for a thinner sheet with larger porosity at a given geometric area.

   With this theoretical background in mind, a subsequent study experimentally assessed the resistivity and the sheet thickness. **Figure 4.7b** plots the resistivity as a function of porosity. The resistivities of K-phosphate solutions decreased with increasing molality and temperatures consistent with a previous report (see **Table 4.4** for the measured values of resistivity for the K-phosphate solutions).[20] At 25 °C, the resistivity of K-phosphate at 0.5 mol kg^{-1} was 0.18 Ω m, which decreased to 0.07 Ω m at 2.5 mol kg^{-1} (saturated) and further to 0.04 Ω m at 4.1 mol kg^{-1} (saturated) at 100 °C. With gas-separators, the resistivity was determined to be ca. 0.04 and 0.09 Ω m for the GS sheets and Zirfon in saturated (4.1 mol kg^{-1}) K-phosphate, respectively. A slight variation of the resistivity among GSs might originate from the distinct tortuosity of sheets[61] (see **Figure 4.8** for the morphology of sheets). These values agreed nicely with the calculations from **Equation 4-10**, thus validating the model for GSs.

Table 4.4. Measured resistivity for various K-phosphate solutions. The measured solutions were 0.5, 1.5 mol kg^{-1} and saturated K-phosphate solutions at 25 °C, and saturated K-phosphate solutions at 60 and 100 °C.

Molality / mol kg^{-1}	Resistivity ρ_0 / Ω m		
	25 °C	60 °C	100 °C
0.5	0.18	-	-
1.5	0.088	-	-
Saturated	0.072	0.048	0.036

   Equation 4-10 also indicates that the resistivity would decrease with a more conductive electrolyte. A supporting electrolyte was thus added to the 4.1 mol kg^{-1} K-phosphate solutions, which decreased

the resistivity by 25% in the case of K_2SO_4 (see **Figure 4.9** for optimization of the ratio of saturated K-phosphate to K_2SO_4) as indicated in **Figure 4.10**. Nevertheless, these quantities were still inferior to that at 7.0 mol kg^{-1} KOH at 100 °C. This picture was, however, changed when the film thickness was considered. Thinner sheets could be fabricated due to the mechanical strength of GSs. **Figure 4.7c** and **4.10b** compile resistance as a function of the sheet thickness at 100 °C. The resistance value of 0.16 Ω for GS at 420 μm was decreased to 0.09 Ω at 260 μm and then to 0.05 Ω at 130 μm. Strikingly, this value of 0.05 Ω was superior to the 0.09 Ω obtained in the industrially-relevant 7.0 mol kg^{-1} KOH solution with Zirfon. These quantitative analyses demonstrated that the near-neutral pH water electrolysis with GS achieved as small *iR* losses as the conventional alkaline water electrolyzers.
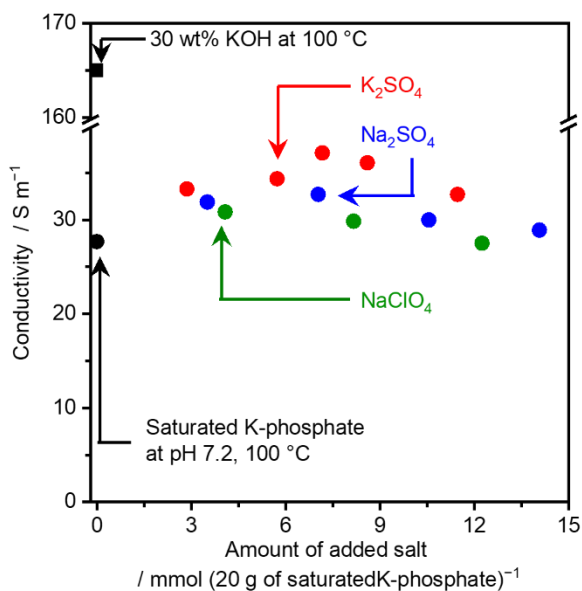

Figure 4.9. Impact of added electrolyte on the conductivity of saturated K-phosphate solutions. The conductivities were measured by potentiostatic electrochemical impedance spectroscopy (PEIS) at an open-circuit potential using Pt wires in 4.1 mol kg^{-1} saturated K-phosphate solutions at 100 °C with additional electrolyte of K_2SO_4, Na_2SO_4, and $NaClO_4$. The pH levels of K-phosphate solutions were adjusted to 7.2 at 25 °C prior to the measurements.
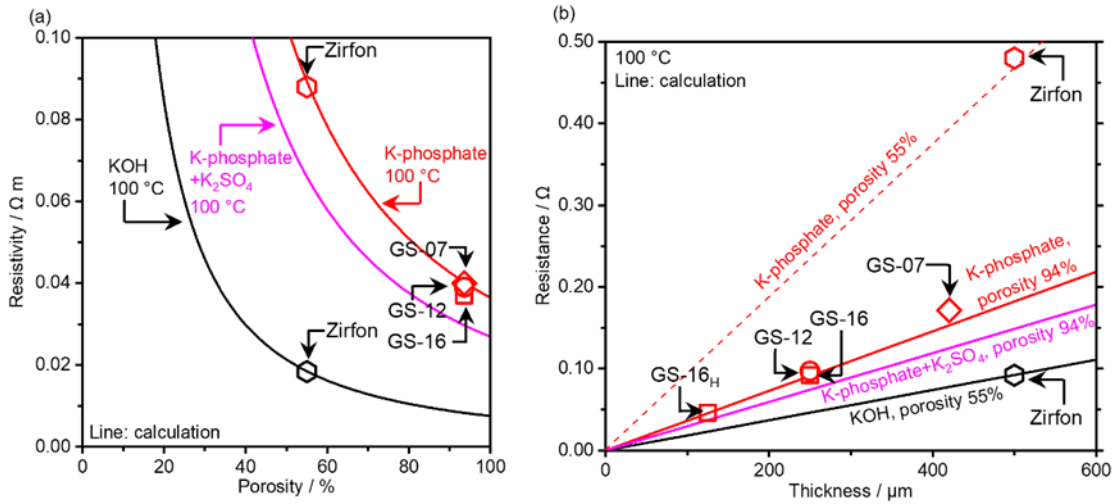
Figure 4.10. Resistivity and resistance of gas-separators in representative electrolyte solutions. (a) Resistivity and (b) resistance of glass fiber sheets (GS-16, GS-12, and GS-07) and Zirfon at 100 °C in 4.1 mol kg^{-1} (saturated) K-phosphate solutions, 4.1 mol kg^{-1} (saturated) K-phosphate solutions with added K$_2$SO$_4$ (7.2 mmol of K$_2$SO$_4$ to 20 g of the saturated K-phosphate solution), or 7 mol kg^{-1} KOH solutions. The open symbols denote the values measured by impedance spectroscopy (see **Figure 4.1** for the cell configuration), and lines represent the calculated values. The pH of the K-phosphate solutions was adjusted to 7.2 at 25 °C prior to each experiment. The GS-16$_H$ with a thickness of 130 μm in the panel (b) was obtained by splitting GS-16 into two pieces (see Experimental for details), and the obtained sheet was subjected to hydrophilization treatment (see the text) and thus labeled with subscript H.

The gas-separation capability of GSs was then examined. From a fundamental viewpoint, the permeability of gas-separator is related to a bubble point pressure expressed in the following Laplace equation:[62]

$$\Delta P = \frac{2\gamma\cos\theta}{r},\qquad(12)$$

in which ΔP is the pressure difference applied across the gas-separator, γ is the surface tension at the liquid-air interface, θ is the contact angle of the liquid with the gas-separator material, and r is the pore radius in sheets. A larger value of the ΔP indicates a higher value of threshold pressure for bubble nucleation, thus leading to less permeability of the bubbles. The contact angle and the pore radius are

127

variables that determine ΔP because the surface tension at the liquid-air interface does not vary with the identity of the separator. More specifically, smaller pore sizes and smaller contact angle are beneficial in decreasing the permeability. Given that the pore size, or the porosity, is a decisive parameter of resistance as described in **Figure 4.7**, GS-16 was herein subjected to hydrophilization treatment by soaking the GS in piranha solutions to decrease the contact angle (the hydrophilized, half-thickness GS-16 is herein denoted as GS-16$_H$). Although the porous nature of the GS did not allow for experimental determination of their contact angles, the literature reported that hydrophilized SiO$_2$ achieved contact angles as low as 2°.[42] **Figure 4.11** summarizes the impact of hydrophilization treatment on the bubble retention. The series resistance using the pristine GS-16 was 0.7 Ω that was found to become 2.2 Ω after the chronopotentiometry (CP) testing of water electorlysis at 100 mA cm^{-2} (vide infra), most likely due to the pore-blocking by the evolved gases. When hydrophilized, however, the GS-16 (denoted as GS-16$_T$) experienced almost negligible increase in the resistance after the CP. The obtained resistance value of 0.8 Ω after the CP was greatly smaller than the value obtained with Zirfon in K-phosphte solution (1.3 Ω). More tellingly, by hydrophlization treatment, GS-16 experienced lessened series resistance value by 1.4 Ω during water electrolysis, corresponding to a decrease of iR loss as much as 140 mV at 100 mA cm^{-2}.
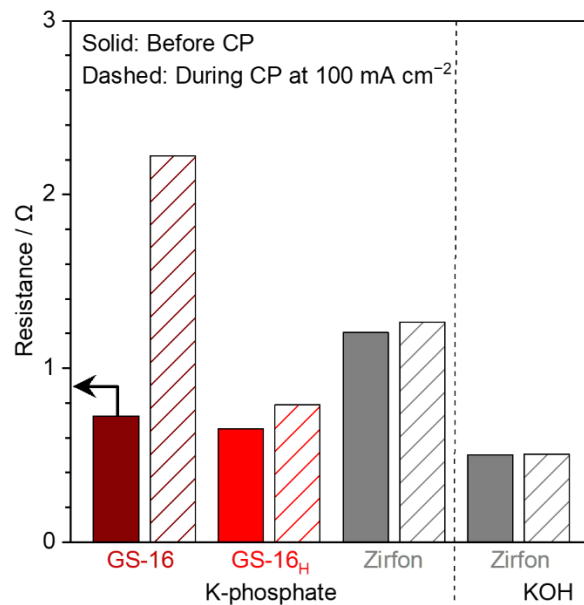
Figure 4.11. Series resistance of separators before and after the electrolysis testing. The resistances of GS-16, GS-16$_H$, or Zirfon in 4.1 mol kg^{-1} (saturated) K-phosphate solution at 100 °C were measured by PEIS before and right after the CP at 100 mA cm^{-2} for 1 h using cell configuration shown in **Figure 4.13**. For comparison, the resistance of Zirfon in 7.0 mol kg^{-1} KOH solutions was also measured and is shown in the figure. The pH levels of K-phosphate solutions were adjusted to 7.2 at 25 °C prior to the measurements.
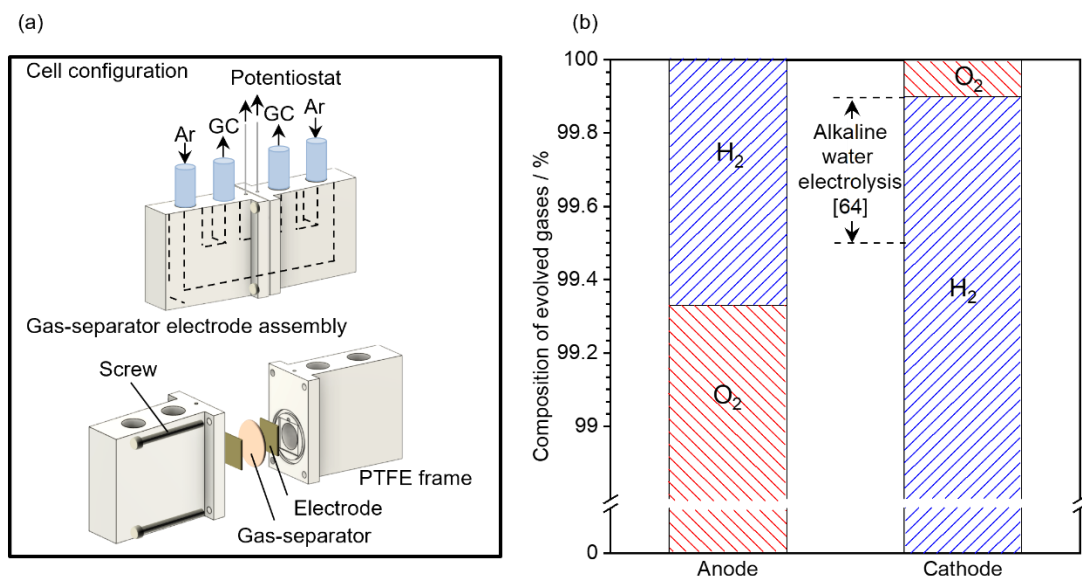
Figure 4.12. Experimental determination of evolved gas purity. (a) A cell configuration developed to measure the purity of evolved gas. The effective surface area of the electrodes was 0.79 cm^2 (a circle of 1 cm diameter). (b) Measured purity of gases evolved at an anode and cathode chambers, respectively, with flowing Ar at 0.5 ml min^{-1}. The purity was measured using the IrO$_x$/Ti felt anode, the Pt/Pt mesh cathode, and the GS-16$_H$ in the saturated K-phosphate solution at 100 °C. pH value of the K-phosphate solutions was adjusted to 7.2 at 25 °C prior to each experiment.

Experimental assessment of the gas purity directly addressed the gas-separation function of the sheet. The cell configuration shown in **Figure 4.12a** was developed for this purpose in which the anode and cathode chambers were separated by an electrode-separator assembly to collect evolved gas separately in each chamber. The purity of gas in this study was defined as the concentration of gas of interest over the sum of H$_2$ and O$_2$ concentration at the cell gas outlet. The purity at a current density of 100 mA cm^{-2} using GS-16$_H$ is summarized in **Figure 4.12b**. Strikingly, the purities of evolved H$_2$ and O$_2$ were as high as ca. 99.9% and 99.3%, respectively. This purity is comparable with the values of >99.5% reported with KOH solution and Zirfon.[63,64] The difference in purities between H$_2$ and O$_2$ may originate from their distinct mass-transport fluxes. Although the purity of this system is as high as conventional water electrolyzers, the purity was less than 100% due to crossover of the evolved gases. Particularly, considering that the reported gas-bubbles size in KOH solutions during water electrolysis, which is 4.8 μm,[65] is three times larger than the pore size of GS-16$_H$, the crossover

of dissolved gases might be caused by diffusion of dissolved gas. Therefore, further tuning electrolyte properties to decrease the diffusion flux of dissolved gases can further increase the gas purity. Overall, these results show that the GS sheets in the saturated K-phosphate solutions can simultaneously achieve low resistance and high gas purity comparable to the existing alkaline water electrolyzers.

4.3.3. Demonstration of water electrolysis using glass fiber sheets in saturated K-phosphate solutions at near-neutral pH

The previous sections disclosed that the saturated phosphate solution was demonstrated to suppress the crossover of dissolved gaseous molecules at the elevated temperatures, and the GS-16$_H$ was found to be capable of blocking the crossover of gas bubbles while concurrently achieving small iR losses. After combining these components with a model Pt/Pt mesh cathode and IrO$_x$/Ti felt anode, this section next examines the near-neutral pH water electrolysis performance. Anode- and cathode-sandwiched gas-separators were used as the zero-gap configuration,[54] which was fixed by polytetrafluoroethylene (PTFE) frame and screws (see **Figure 4.13** for the cell illustration).
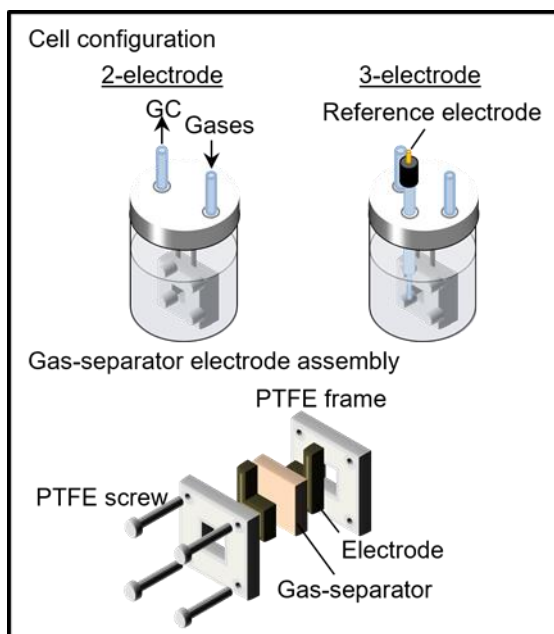

Figure 4.13. Home-made cell for near-neutral pH water electrolysis in a zero-gap configuration. This cell configuration was used for catalytic testing in **Figures 4.14, 4.16-21,** and **4.23**. The effective surface area of the electrodes was 1×1 cm^2.

Figure 4.14 shows the breakdown of total cell voltage for near-neutral pH and alkaline water electrolysis at an applied constant current density of 100 mA cm^{-2} at 100 °C (see **Figure 4.15** and **4.16** for raw data). The alkaline condition employed 7.0 mol kg^{-1} KOH as an electrolyte, and NiFeO$_x$/Ni foam as an anode instead of the IrO$_x$ catalyst because NiFeO$_x$ is known to be a highly active OER catalyst under alkaline conditions, and IrO$_x$ degrades during OER under alkaline

conditions.[20] Notably, the high alkalinity of 7.0 mol kg^{-1} KOH solution did not facilitate the determination of a half-reaction performance, and the total overpotential of both HER and OER is displayed in this figure.
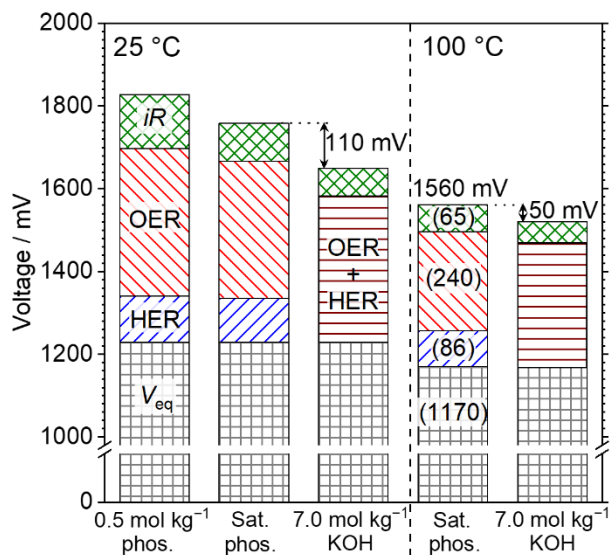

Figure 4.14. Voltage breakdown of water electrolysis at 100 mA cm^{-2} at 25 °C and 100 °C in various electrolyte solutions of 0.5, 2.5 (saturated at 25 °C), 4.1 (saturated at 100 °C) mol kg^{-1} phosphate with GS-16$_H$ and 7.0 mol kg^{-1} KOH solutions with Zirfon. V_{eq} denotes the reversible voltage. HER and OER were the overpotential for reaction the hydrogen evolution reaction (HER) and oxygen evolution reaction (OER), respectively. These overpotentials were determined by electrocatalytic testing in buffered solutions in every solution under Ar bubbling. The iR loss was determined with a measured impedance value.
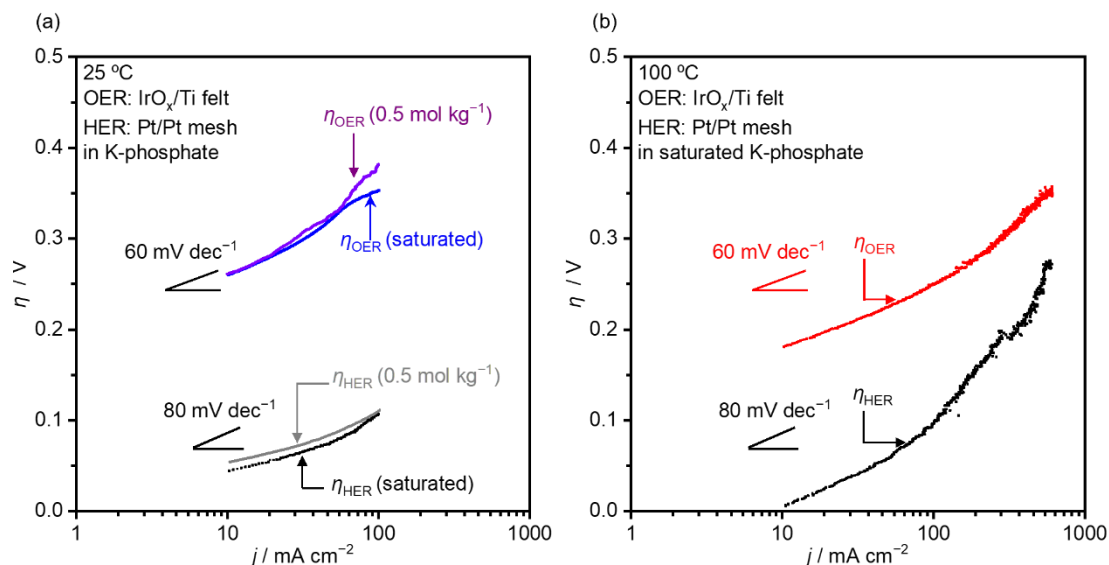
Figure 4.15. Tafel plots for the half-reactions. The current-potential relationship for the cathodic and anodic half-reactions were measured using Pt/Pt mesh and IrO$_x$/Ti felt for the hydrogen evolution reaction (HER) and oxygen evolution reaction (OER), respectively: (a) 0.5 mol kg^{-1} and saturated K-phosphate at 25 °C; (b) saturated K-phosphate at 100 °C. All measurements were conducted by CV at a scan rate of 1 mV s^{-1} in the three-electrode configuration under Ar bubbling. The pH levels of K-phosphate solutions were adjusted to 7.2 at 25 °C prior to the measurements.
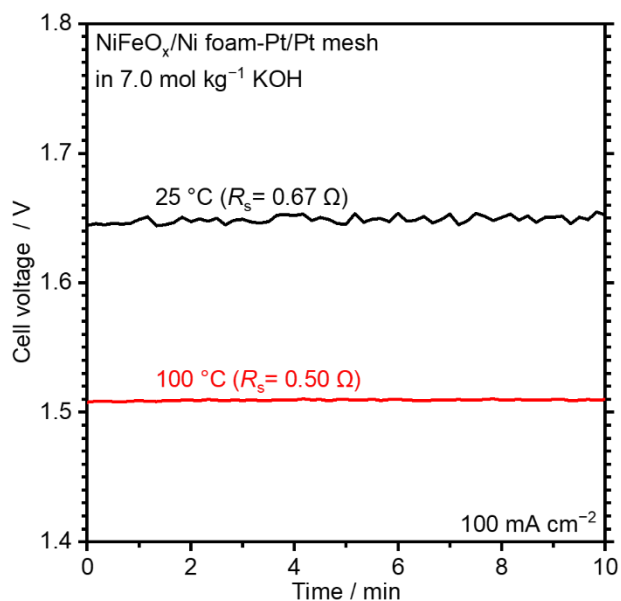
Figure 4.16. Demonstration of water electrolysis in 7.0 mol kg^{-1} KOH solutions with Zirfon at 25 and 100 °C using a Pt/Pt mesh cathode and a NiFeO$_x$/Ni foam anode.

The total cell voltage was 1.83 V at 0.5 mol kg^{-1} at 25 °C with K-phosphate electrolyte solutions, which decreased by 70 mV at 2.5 mol kg^{-1} (saturated). The improvement most likely arose from the acceleration of mass transport as I previously reported.[20] Nevertheless, even when using the concentrated solution, the total cell voltage is still inferior to alkaline conditions by 110 mV. The difference in *iR* loss value between **Figure 4.7c** and **Figure 4.14c** plausibly originated from generated bubbles during electrolysis[66] and wiring.[67]

Elevation of the reaction temperature was considered to be beneficial in improving kinetics and mass transport during water electrolysis. Herein the water electrolysis performance was assessed at 100 °C, and the voltage breakdown is detailed in **Figure 4.14**. Strikingly, a current density of 100 mA cm^{-2} was reached at a total cell voltage as small as 1.56 V in the saturated K-phosphate solutions of 4.1 mol kg^{-1} at 100 °C. This value corresponded to the cell efficiency of 94% and 75% with respect to the thermoneutral voltage of 1.47 V and reversible voltage of 1.17 V. The concurrently measured Faradaic efficiency (FE) for both H$_2$ and O$_2$ was almost 100% continuously for 1 h (**Figure 4.17**), which is consistent with the near unity purity of gases discussed in **Figure 4.12b**. In contrast, the alkaline system in 7.0 mol kg^{-1} KOH solutions required 1.51 V to reach 100 mA cm^{-2}, consistent with industrially related values.[4] Quantitatively, therefore, the near-neutral pH water electrolysis

achieved a comparable performance to the alkaline electrolyzers with a difference of merely 50 mV at 100 mA cm^{-2}. Among this 50 mV, ca. 15 mV was accounted for by the difference in series resistance, i.e., 0.65 and 0.50 Ω for the K-phosphate and KOH solutions, respectively. The remaining 35 mV is reasoned to originate from the kinetic overpotentials.
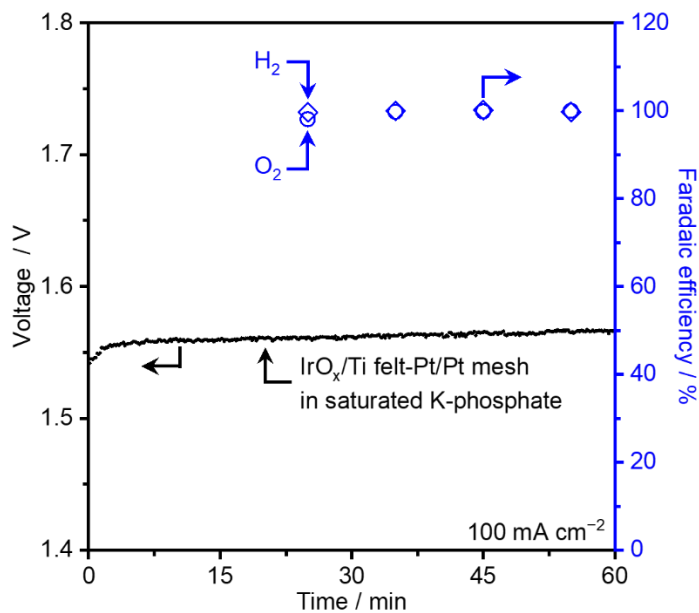

Figure 4.17. Demonstration of near-neutral pH water electrolysis. (a) Chronopotentiometry (CP) at 100 mA cm^{-2} and corresponding Faradaic efficiency of evolved O$_2$ and H$_2$ using glass fiber sheet GS-16$_H$ in 4.1 mol kg^{-1} (saturated) K-phosphate solutions at 100 °C. The Faradaic efficiency was determined by measuring gas composition at cell outlet using gas chromatography equipped with a thermal conductivity detector. The pH levels of K-phosphate solutions were adjusted to 7.2 at 25 °C prior to the measurements.
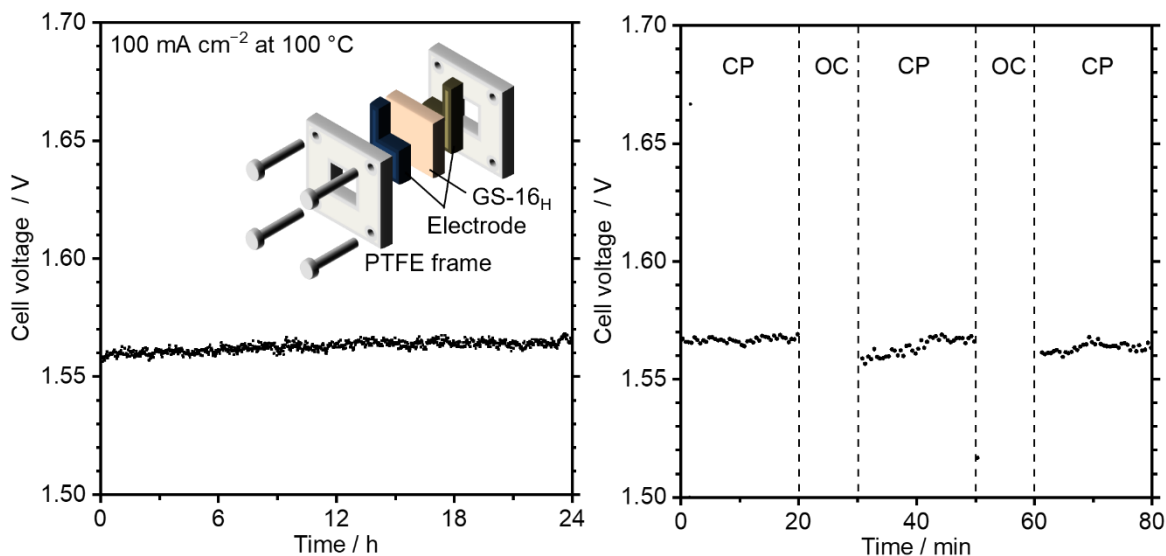
Figure 4.18. Demonstration of near-neutral pH water electrolysis. (a) Prolonged CP testing at 100 mA cm^{-2} using an IrO$_x$/Ti felt anode and a Pt/Pt mesh cathode in 4.1 mol kg^{-1} (saturated) K-phosphate with GS-16$_H$. The inset illustration is a cell configuration used in the demonstration. (b) On-off cycling of water electrolysis in densely buffered solutions at 100 °C. On-off testing results were obtained by periodic CP at 100 mA cm^{-2} for 20 min with an interval of 10 min at open-circuit (OC) condition using a Pt/Pt mesh cathode and an IrO$_x$/Ti felt anode in saturated K-phosphate with GS-16$_H$. The measurement was performed after CP for 24 h as shown in (a). pH level of K-phosphate solutions was adjusted to 7.2 at 25 °C prior to the measurements.

The longevity of the cell is another figure of merit in assessing the system performance. **Figure 4.18a** shows the chronopotentiometry (CP) at 100 mA cm^{-2} for 24 h indicating that the initial overall cell voltage of 1.56 V increased by merely 5 mV after 24 h. X-ray photoelectron spectroscopy (XPS) analysis in **Figure 4.19** showed no apparent change of surface chemical state. Subsequent on-off testing in **Figure 4.18b** suggested that the system would retain its integrity upon start-up and shut-down cycles. SEM micrographs of GS-16$_H$ before and after the 24 h CP testing in **Figure 4.18** disclosed that its diameter remained to be 3.5 μm, demonstrating the high tolerance of GSs. **Figure 4.20** plots the cell voltage in 7.0 mol kg^{-1} KOH solution with NiFeO$_x$/Ni foam anode and Pt/Pt mesh cathode for comparison (see **Figure 4.21** for the data obtained with 1.0 mol kg^{-1} KOH electrolyte solutions). This alkaline system required 1.51 V to reach 100 mA cm^{-2} consistent with industrial values;[69] this increased to a value of 1.53 V after 24 h.

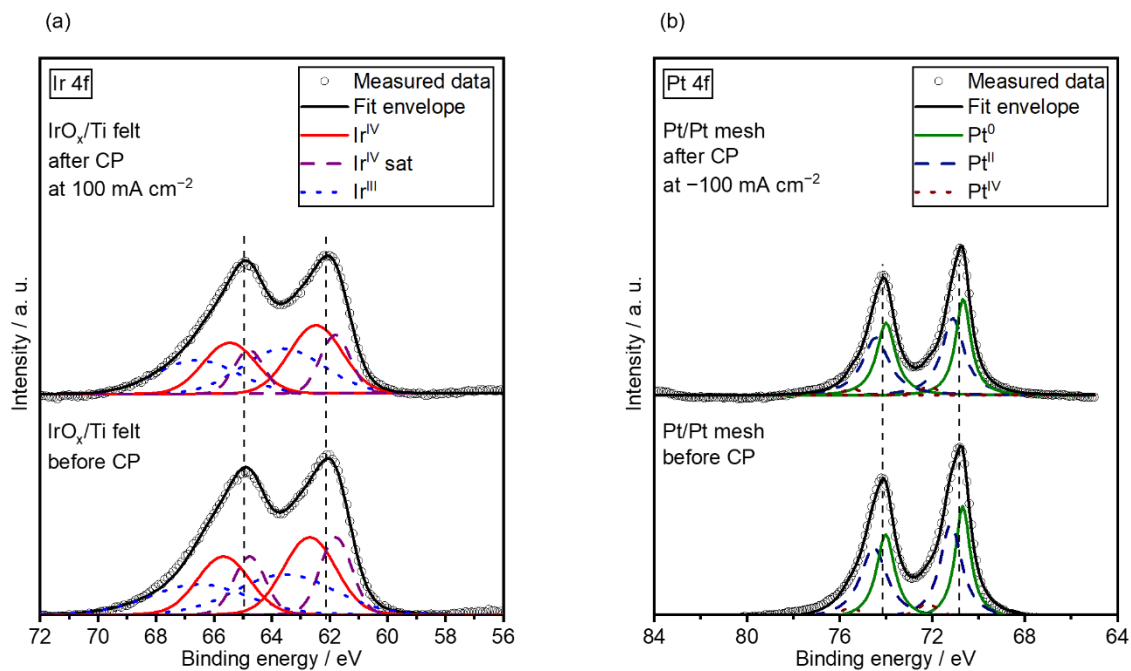**Figure 4.19.** X-ray photoelectron spectroscopy (XPS) spectra of electrodes. (a) Ir 4f spectra of IrO$_x$/Ti felt and (b) Pt 4f spectra of Pt/Pt mesh both before and after CP testing of electrolysis at 100 mA cm^{-2} for 24 h and subsequent on-off cycling testing as shown in **Figure 4.18**. The peak deconvolution was performed based on the peak positions in a National Institute of Standards and Technology (NIST) database.[68]
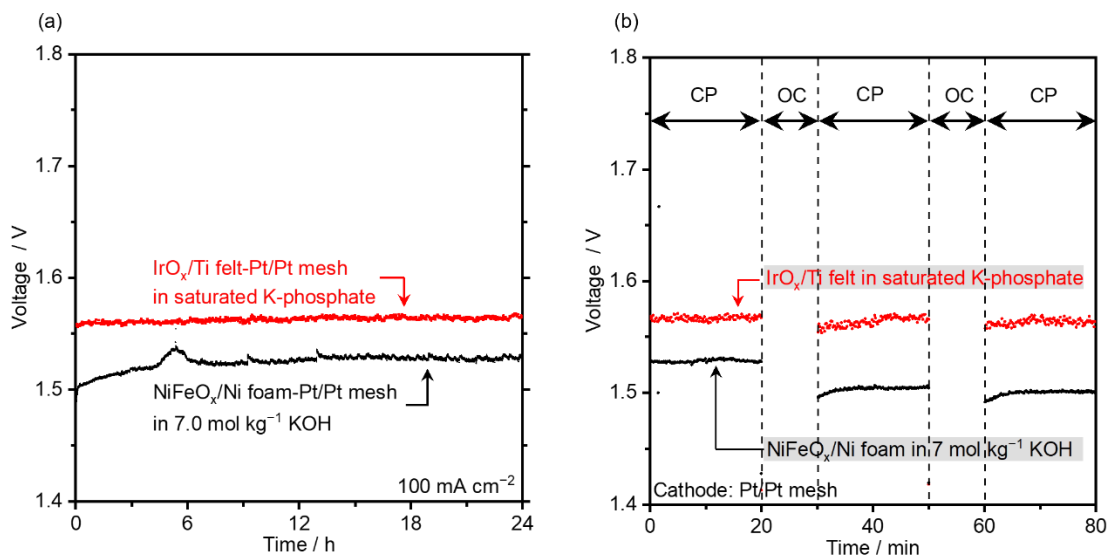
Figure 4.20. Demonstration of near-neutral pH water electrolysis at 100 °C. (a) Prolonged CP testing at 100 mA cm^{-2}. (b) On-off cycling of water electrolysis; the on-off testing results were obtained by periodic CP at 100 mA cm^{-2} for 20 min with an interval of 10 min at open-circuit (OC) condition. These measurements were performed after CP for 24 h shown in (a). A Pt/Pt mesh was used as a cathode. (Red line) An IrO$_x$/Ti felt anode in saturated K-phosphate with GS-16$_H$. (Black line) A NiFeO$_x$/Ni foam anode in 7.0 mol kg^{-1} KOH with Zirfon. The pH levels of K-phosphate solutions were adjusted to 7.2 at 25 °C prior to the measurements.

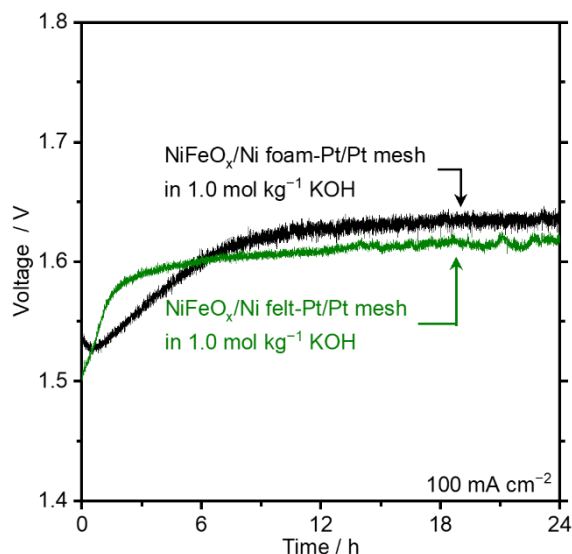**Figure 4.21.** Water electrolysis testing in diluted KOH solutions. CP was recorded at 100 mA cm^{-2} and 100 °C under Ar bubbling using a Pt/Pt mesh cathode in 1.0 mol kg^{-1} KOH with Zirfon using (black line) a NiFeO$_x$/Ni foam or (green line) NiFeO$_x$/Ni felt anode.

My study was extended to higher current densities at 400 mA cm^{-2}, and the resulting voltage breakdown is shown in **Figure 4.22**. The total cell voltage was anticipated to reach 1.91 V with almost equal contribution from the OER, HER, and the *iR* loss in saturated K-phosphate solutions using GS-16$_H$ at 100 °C: This assessment was experimentally validated by the full-cell testing at 400 mA cm^{-2} in **Figure 4.23**. This analysis points to the need for concurrent efforts on these three aspects when reaching higher rates. For instance, development of active OER and HER catalysts seems essential in enhancing the performance, but the engineering surface morphology to facilitate gas-bubble removal from catalyst surfaces is a key issue[59] and is also likely dependent on the properties of the electrolyte.[69,70] Another direction includes the development of more conductive electrolyte. Simply adding supporting electrolyte increased conductivity of the solution as discussed in **Figure 4.10**, which however was accompanied by a loss in cell performance (see **Figure 4.23**) suggesting kinetic losses due to the poisoning of the catalyst surface by the adsorption of sulfate ions.[71] These aspects call for integrated research efforts toward the entire system rather than a single component.
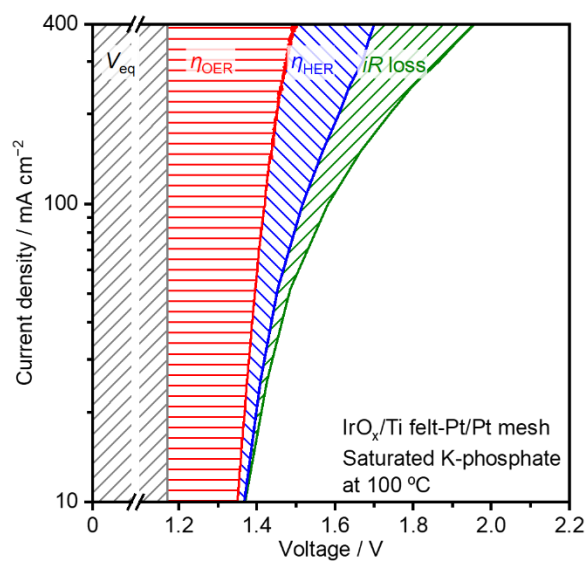
Figure 4.22. Voltage breakdown of near-neutral pH water electrolysis. V_{eq} denotes the reversible voltage. η_{OER} and η_{HER} are the overpotentials for the hydrogen evolution reaction (HER) and oxygen evolution reaction (OER), respectively. These overpotentials were determined by electrocatalytic testing in buffered solutions in 4.1 mol kg^{-1} (saturated) K-phosphate solutions at 100°C under Ar bubbling at a scan rate of 1 mV s^{-1}. The *iR* loss was determined with a measured series resistance by impedance spectroscopy when the GS-16$_H$ was used as a gas-separator.

Figure 4.23. Impacts of added electrolyte on the water electrolysis performance. CP profile was recorded at 400 mA cm^{-2} using an IrO$_x$/Ti felt anode and a Pt/Pt mesh cathode in 50 g of saturated K-phosphate solution with or without 3.1 g of added K$_2$SO$_4$ at 100 °C with GS-16$_H$.

4.4. Conclusion

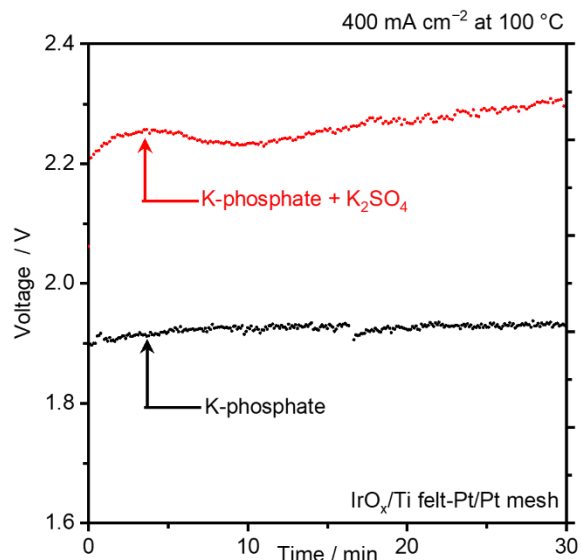This study investigated efficient near-neutral pH water electrolysis for pure H$_2$ production at reaction rates compatible with industrial applications. Low solubility and low diffusion coefficients of dissolved H$_2$ and O$_2$ gases in concentrated phosphate buffer solutions almost eliminated the diffusion-limited current densities of the H$_2$ oxidation and O$_2$ reduction reactions, which can be interpreted as minimized crossover of the dissolved gases during water electrolysis. These diffusion-limited currents were largely insensitive to temperature. The gas-bubble crossover at buffered neutral pH was successfully regulated via glass-made sheets (i.e., GS) as a gas separator, which are not usable in alkaline electrolyzers because they dissolve. Assessment of the porosity and thickness of the sheets showed that the GSs together with saturated K-phosphate solutions can achieve a small *iR*-loss comparable to or less than Zirfon with 7.0 mol kg^{-1} KOH solutions. The *iR* loss values originating from the GSs were reduced by 140 mV during water electrolysis at 100 mA cm^{-2} by a hydrophilization treatment to the GSs. Experimental testing with an electrolysis cell employing the GS-16$_H$ exhibited ca. 99.9% purity of evolved H$_2$, thus demonstrating the feasibility of GSs as the gas

separator. Current densities of 100 mA cm^{-2} were achieved at as low total cell voltage as 1.56 V with negligible performance losses after 24 h of operation corresponding to 94% of cell efficiency with respect to the thermoneutral voltage of 1.47 V (this experiment used saturated K-phosphate solution as electrolyte at 100 °C with GS-16$_H$ as the gas-separator in the catalytic testing). This performance is comparable to the established alkaline counterpart. At larger current densities, however, voltage breakdown analysis showed that HER and OER kinetic loss and *iR* loss all contribute substantially to imperfection when achieving higher rates, thus calling for concurrent research efforts to both electrodes and electrolytes in future studies. Overall, my findings demonstrate that near-neutral pH water electrolysis is an alternative to existing acidic and alkaline water electrolysis, thus paving the way for penetration of green H$_2$.

4.5. References

[1] S. E. Hosseini, M. A. Wahid, *Renew. Sustain. Energy Rev*. **2016**, *57*, 850-866.

[2] D. V. Esposito, *Joule* **2017**, *1*, 651-658.

[3] Ø. Ulleberg, *Int. J. Hydrogen Energy* **2003**, *28*, 21-33.

[4] A. Buttler, H. Spliethoff, *Renew. Sustain. Energy Rev*. **2018**, *82*, 2440-2454.

[5] M. F. Lagadec, A. Grimaud, *Nat. Mater*. **2020**, *19*, 1140-1150.

[6] B. Mayerhöfer, D. McLaughlin, T. Böhm, M. Hegelheimer, D. Seeberger, S. Thiele, *ACS Appl. Energy Mater* **2020**, *3*, 9635-9644.

[7] A. Ursúa, L. M. Gandía, P. Sanchis. *Proc. IEEE* **2011**, *99*, 1-17.

[8] G. Chisholm, L. Cronin, *Storing Energy* Elsevier, Amsterdam, **2016**, 315-343.

[9] P. Trinke, P. Haug, J. Brauns, B. Bensmann, R. Hanke-Rauschenbach, T. Turek, *J. Electrochem. Soc*. **2018**, *165*, F502-F513.

[10] D. Strmcnik, M. Uchimura, C. Wang, R. Subbaraman, N. Danilovic, D. van der Vliet, A. P. Paulikas, V. R. Stamenkovic, N. M. Markovic, *Nat. Chem*. **2013**, *5*, 300-306.

[11] T. Shinagawa, A. T. Garcia-Esparza, K. Takanabe, *ChemElectroChem* **2014**, *1*, 1497-1507.

[12] T. Takashima, K. Ishikawa, H. Irie, *ACS Catal*. **2019**, *9*, 9212-9215.

[13] I. Katsounaros, J. C. Meier, S. O. Klemm, A. A. Topalov, P. U. Biedermann, M. Auinger, K. J. J. Mayrhofer, *Electrochem. Commun*. **2011**, *13*, 634-637.

[14] M. Auinger, I. Katsounaros, J. C. Meier, S. O. Klemm, P. U. Biedermann, A. A. Topalov, M. Rohwerder, K. J. J. Mayrhofer, *Phys. Chem. Chem. Phys*. **2011**, *13*, 16384-16394.

[15] W. Sheng, Z. Zhuang, M. Gao, J. Zheng, G. Chen, Y. Yan, *Nat. Commun*. **2015**, *6*, 5848.

[16]   T. Shinagawa, M. T-K. Ng, K. Takanabe, *ChemSusChem* **2017**, *10*, 4155-4162.

[17]   T. Shinagawa, K. Takanabe, *J. Phys. Chem. C* **2015**, *119*, 20453-20458.

[18]   L. D. S. Muñoz, A. Bergel, D. Féron, R. Basséguy, *Int. J. Hydrogen Energy* **2010**, *35*, 8561-8568.

[19]   T. Shinagawa, K. Takanabe, *ChemSusChem* **2017**, *10*, 1318-1336.

[20]   T. Naito, T. Shinagawa, T. Nishimoto, K. Takanabe, *ChemSusChem* **2020**, *13*, 5921-5933.

[21]   N. M. Marković, H. A. Gasteiger, P. N. Ross Jr., *J. Phys. Chem.* **1995**, *99*, 3411-3415.

[22]   M. D. Maciá, J. M. Campiña, E. Herrero, J. M. Feliu, *J. Electroanal. Chem.* **2004**, *564*, 141-150.

[23]   E. Fabbri, S. Taylor, A. Rabis, P. Levecque, O. Conrad, R. Kötz, T. J. Schmidt, *ChemCatChem* **2014**, *6*, 1410-1418.

[24]   T. Shinagawa, K. Takanabe, *J. Power Sources* **2015**, *287*, 465-471.

[25]   S. Guo, D. Li, H. Zhu, S. Zhang, N. M. Markovic, V. R. Stamenkovic, S. Sun, *Angew. Chem. Int. Ed.* **2013**, *52*, 3465-3468.

[26]   N. M. Marković, T. J. Schmidt, V. Stamenković, P. N. Ross, *Fuel Cells* **2001**, *1*, 105-116.

[27]   B. Han, C. E. Carlton, J. Suntivich, Z. Xu, Y. Shao-Horn, *J. Phys. Chem. C* **2015**, *119*, 3971-3978.

[28]   V. R. Stamenkovic, B. Fowler, B. S. Mun, G. Wang, P. N. Ross, C. A. Lucas, N. M. Markovic, *Science* **2007**, *315*,493-497.

[29]   V. Stamenkovic, B. S. Mun, K. J. J. Mayrhofer, P. N. Ross, N. M. Marković, J. Rossmeisl, J. Greeley, J. K. Nørskov, *Angew. Chem. Int. Ed.* **2006**, *45*, 2897-2901.

[30]   X. Huang, Z. Zhao, L. Cao, Y. Chen, E. Zhu, Z. Lin, M. Li, A. Yan, A. Zettl, Y. M. Wang, X. Duan, T. Mueller, Y. Huang. *Science* **2015**, *348*, 1230-1234.

[31]   J. Brauns, J. Schönebeck, M. R. Kraglund, D. Aili, J. Hnát, J. Žitka, W. Mues, J. O. Jensen, K. Bouzek, T. Turek, *J. Electrochem. Soc.* **2021**, *168*, 014510.

[32]   H. Ito, T. Maeda, A. Nakano, H. Takenaka, *Int. J. Hydrogen Energy* **2011**, *36*, 10527-10540.

[33]   S. Miyanishi, T. Yamaguchi, *Phys. Chem. Chem. Phys.* **2016**, *18*, 12009-12023.

[34]   X. Pang, J. T. Davis, A. D. Harvey, D. V. Esposito, *Energy Environ. Sci.* **2020**, *13*, 3663-3678.

[35]   S. M. H. Hashemi, P. Karnakov, P. Hadikhani, E. Chinello, S. Litvinov, C. Moser, P. Koumoutsakos, D. Psaltis, *Energy Environ. Sci*. **2019**, *12*, 1592-1604.

[36]   J. C. Bui, J. T. Davis, D. V. Esposito, *Sustainable Energy Fuels* **2020**, *4*, 213-225.

[37] S. Mohammad, H. Hashemi, M. A. Modestino, D. Psaltis, *Energy Environ. Sci.* **2015**, *8*, 2003-2009.

[38] P. Atkins, J. D. Paula, *Atkins' Physical Chemistry, eighth ed.*, W. H. Freeman and Company, New York, **2006**.

[39] T. Shinagawa, K. Takanabe, *J. Phys. Chem. C* **2016**, *120*, 1785-1794.

[40] C. Hermann, I. Dewes, A. Schumpe, *Chem. Eng. Sci.* **1995**, *50*, 1673-1675.

[41] S. Weisenberger, A. Schumpe, *AIChE J.* **1996**, *42*, 298-300.

[42] T. Son, E. Yang, E. Yu, K. H. Oh, M.-W. Moon, H.-Y. Kim, *J. Mech. Sci. Technol.* **2017**, *31*, 5407-5414.

[43] M. A. Petit, V. Plichon, *J. Electroanal. Chem.* **1998**, *444*, 247-252.

[44] A. M. Feltham, M. Spiro, *Chem. Rev.* **1971**, *71*, 177-193.

[45] I. Lee, K-Y Chan, D. L. Phillips, *Appl. Surf. Sci.* **1998**, *136*, 321-330.

[46] Z. Lu, W. Xu, W. Zhu, Q. Yang, X. Lei, J. Liu, Y. Li, X. Sun, X. Duan, *Chem. Commun.* **2014**, *50*, 6479-6482.

[47] A. J. Bard, L. R. Faulkner, *Electrochemical Methods: Fundamentals and Applications*, Wiley, New York, **2010**.

[48] P. Daubinger, J. Kieninger, T. Unmüssig, G. A. Urban, *Phys. Chem. Chem. Phys.* **2014**, *16*, 8392-8399.

[49] A. Berná, V. Climent, J. M. Feliu, *Electrochem. Commun.* **2007**, *9*, 2789-2794.

[50] R. Phillips, C. W. Dunnill, *RSC Adv.* **2016**, *6*, 100643-100651.

[51] U.S. Department of the Interior, *MINERAL COMMODITY SUMMARIES 2020*, **2020**.

[52] U.S. Department of the Interior, *Rare Earth Elements—Critical Resources for High Technology*, **2002**.

[53] F. K. Crundwell, *ACS Omega* **2017**, *2*, 1116-1127.

[54] Cytiva, available online: https://www.cytivalifesciences.com/en/us/shop/whatman-laboratory-filtration/glass-and-quartz-microfiber-filter/binderless-glass-microfiber-filter (accessed on 20 May 2021).

[55] Technical Data Sheet ZIRFON PERL UTP 500 Separator membrane for alkaline electrolysis, AGF-16, **2020**.

[56] L. Chen, S. Ding, Z. Liang, L. Zhou, H. Zhang, C. Zhang, *Aerosol Sci. Technol.* **2017**, *51*, 1082-1092.

[57] M.J. Martínez, S. Shimpalee, J. W. Van Zee, *J. Electrochem. Soc.* **2009**, *156*, B80-B85.

[58] B. Tjaden, S. J. Cooper, D. J. Brett, D. Kramer, P. R. Shearing, *Curr. Opin. Chem. Eng*. **2016**, *12*, 44-51,

[59] M. T. de Groot, A. W. Vreman, *Electrochim. Acta* **2021**, *369*, 137684.

[60] R. Bataller, J. M. Gandia, E. Garcia-Breijo, M. Alcañiz, J. Soto, *Electrochim Acta* **2015**, *82*, 263-272.

[61] F. Yang, M. J. Kim, M. Brown, B. J. Wiley, *Adv. Energy Mater.* **2020**, *10*, 2001174.

[62] PH. Vermeiren, R. Leysen, H. Beckers, J. P. Moreels, A. Claes, *J. Porous Mater.* **2008**, *15*, 259-264.

[63] D. Pletcher, F. C. Walsh, *Industrial electrochemistry. 2nd ed.*, Blackie Academic & Professional, London, **1990**.

[64] P. Haug, M. Koj, T. Turek, *Int. J. Hydrogen Energy* **2017**, *42*, 9406-9418.

[65] A. Roy, S. Watson, D. Infield, *Int. J. Hydrogen Energy* **2006**, *31*, 1964-1979.

[66] L. J. J. Janssen, C. W. M. P. Sillen, E. Barendrecht, S. J. D. van Stralen, *Electrochim. Acta* **1984**, *29*, 633-642.

[67] M. I. Gillespie, F. van der Merwe, R. J. Kriek, *J. Power Sources* **2015**, *293*, 228-235.

[68] W. Xu, Z. Lu, X. Sun, L. Jiang, X. Duan, *Acc. Chem. Res.* **2018**, *51*, 1590-1598.

[69] XPS National institute of standards and technology (NIST), available online: https://srdata.nist.gov/xps/ (accessed on 22 September 2021).

[70] X. Zhao, H. Ren, L. Luo, *Langmuir* **2019**, *35*, 5392-5408.

[71] E. Protopopoff, P. Marcus, *J. Electrochem. Soc.* **1988**, *135*, 3073-3075.

5. General conclusions

In this dissertation, water electrolysis at near-neutral pH was investigated, aiming for the construction of the electrolysis system at near-neutral pH, which has the potential to produce inexpensive hydrogen. Particularly, the fundamental understanding regarding the influence of electrolyte properties on the efficiency of water electrolysis and the first attempt to design near-neutral pH water electrolysis using a glass sheet as a cost-effective gas separator at industrially relevant currents was investigated.

In **Chapter 2**, literatures of iridium oxide, the most active OER catalyst, were reviewed as a model catalyst to provide a fundamental understanding to establish guidelines for the development of highly active and stable OER catalysts. Specifically, in-situ or operando spectroscopic and advanced computational studies on the OER of iridium oxide for the oxidation of both water molecules and hydroxide ions were reviewed.

In **Chapter 3**, the mass transport flux during water electrolysis was quantitatively investigated with tuning properties of phosphate buffer solutions, whose pH level was adjusted to 7.0. Then saturated K-phosphate solutions at elevated temperatures (80-100 °C) were found to exhibit a comparable value of mass transport flux to extremely acidic and alkaline conditions. In the thus determined solutions, water electrolysis at an applied current density of 10 mA cm^{-2} was demonstrated, performing not only comparable cell voltage without iR losses to the existing electrolyzers but also stable operation. Then, the saturated K-phosphate solutions were considered as a potential electrolyte of water electrolysis at near-neutral pH.

In **Chapter 4**, gas crossover as dissolved gases and gas bubbles during water electrolysis was investigated. As a result, the use of concentrated K-phosphate solutions was suggested to suppress the crossover of the dissolved gases at elevated temperatures. The subsequent analysis on the crossover of the bubbles focused on using glass sheets as a gas separator, exhibiting comparable iR loss to existing water electrolyzers with successful regulation of the crossover of the bubbles. Finally, an electrochemical cell using the glass sheet in the saturated K-phosphate solutions was designed to demonstrate water electrolysis. The demonstrated total cell voltage including iR losses was comparable to the existing water electrolyzer, indicating the feasibility of near-neutral pH water electrolysis.

All in all, this dissertation presented the potential of water electrolysis at near-neutral pH. I sincerely hope that the findings in this dissertation help further the development of near-neutral pH water electrolysis system and the realization of a future sustainable society.

6. Future perspective

Based on my findings in this dissertation and my knowledge obtained through my research work, future perspectives of a near-neutral pH water electrolysis operated at industrially relevant current density ($> 100\,\text{mA}\,\text{cm}^{-2}$) are described here. In this dissertation, the most significant issues to improve the efficiency were found as (a) using noble metal catalysts such as IrO_x and Pt as model catalysts and (b) enlarged *iR* loss with increasing current density (c) designing components other than electrolyte and gas-separator. Therefore, solving these issues by using low-cost materials is required to promote the implementation of near-neutral pH water electrolysis.

In solving issue (a), the development of the electrocatalysts at higher current density will require research efforts on both improving intrinsic catalytic activity and facilitating bubble detachment from the catalyst surface. For the intrinsic catalytic activity, the difference originating from pH difference, such as different reaction mechanisms[1] and stability[2], should be taken into account. With this in mind, low-cost elements (or combinations of low-cost elements) that have not been used due to poor activity or stability under acidic or alkaline pH conditions may show high catalytic activity. In this context, revisiting theories that have already been considered for acidic or alkaline pH conditions may help develop the electrocatalysts, e.g., constructing volcano plots at near-neutral pH. For the facilitating bubble detachment, bubble behavior such as covering the active site would become an issue in the high current range used in industry.[3] In this context, because the nucleation and detachment of bubbles are influenced by the electrolyte properties,[4,5] electrolyte engineering, such as considered in this dissertation, would be essential to develop the electrocatalysts.

In solving issue (b), thinner gas-separators than the GS-16$_H$ investigated in **Chapter 4** will reduce resistances due to solution resistance. Although thinner gas-separators will exhibit lower resistances, the thinner gas-separators weaken the mechanical strength simultaneously, causing gas-separator failure and resulting in electric short-circuit. To meet the low thickness and high mechanical stability of a gas-separator at the same time, using inorganic materials such as porous ceramics,[6] solid electrolyte,[7] or composites of polymers and inorganic materials[8] might be helpful due to their high mechanical strength. In addition to the contribution of the separator to *iR* loss, increasing the conductivity of the substrate (and catalyst layer) can also play an essential role in reducing *iR* loss. In this direction, using more conductive substrates such as Cu[9] than Ti substrate,[10] which is used as the anode substrate through this dissertation, will reduce *iR* loss.

In solving issue (c), replacing materials used in conventional water electrolyzers with cheaper materials will be effective to construct highly efficient and cost-effective system. Taking the alkaline electrolyzer, which is one of the most cost-effective water electrolyzers, as an example, frame material mainly made of Ni[11] can be replaced with cheaper Cu due to the stability at near-neutral pH. The substitution results in 64% reduction in material costs according to the reported cost of each material.[12] Although detailed cost estimation is challenging because manufacturing companies of the electrolyzers have not disclosed the detailed cost breakdown of every component, a significant cost reduction in the electrolyzer can be expected when material substitution for various components is achieved due to a mild environment at near-neutral pH.

These fundamental studies will be the key to further improving the efficiency of near-neutral pH water electrolysis and constructing a system which is both less expensive and more efficient than existing electrolyzers.

References

[1]   T. Takashima, K. Hashimoto, R. Nakamura, *J. Am. Chem. Soc*. **2012**, *134*, 1519-1527.

[2]   C. C. L. McCrory, S. Jung, I. M. Ferrer, S. M. Chatman, J. C. Peters, T. F. Jaramillo, *J. Am. Chem. Soc*. **2015**, *137*, 4347-4357.

[3]   D. V. Esposito, *Joule* **2017**, *1*, 651-658.

[4]   X. Zhao, H. Ren, L. Luo, *Langmuir* **2019**, *35*, 5392-5408.

[5]   J. D. Paulsen, J. C. Burton, S. R. Nagel, *Phys. Rev. Lett.* **2011**, *106*, 114501.

[6]   L. J. Bonderer, P. W. Chen, P. Kocher, L. J. Gauckler, *J. Am. Ceram. Soc*. **2010**, *93*, 3624-3631.

[7]   G. Qing, K. Sukegawa, R. Kikuchi, A. Takagaki, S. T. Oyama, *J. Appl. Electrochem.* **2017**, *47*, 803-814.

[8]   P. H. Vermeiren, J. P. Moreels, R. Leysen, *J. Porous Mater*. **1996**, *3*, 33-44.

[9]   R. A. Matula, *J. Phys. Chem. Ref. Data* **1979**, *8*, 1147-1298.

[10] E. A. Bel'skaya, E. Y. Kulyamina, *High Temp*. **2007**, *45*, 785-796.

[11] Nouryon, *"Materials for intensified alkaline water electrolysis"*, **2019**.

[12] O. Schmidt, A. Hawkes, A. Gambhir, I. Staffell. *Nat. Energy* **2017**, *2*, 17110.

List of Publications

This thesis is based on the following publications:

[1] **T. Naito**, T. Shinagawa, T. Nishimoto, K. Takanabe, *ChemSusChem* **2020**, *13*, 5921-5933.

[2] **T. Naito**, T. Shinagawa, T. Nishimoto, K. Takanabe, *Inorg. Chem. Front.* **2021**, *8*, 2900-2917.

[3] **T. Naito**, T. Shinagawa, T. Nishimoto, K. Takanabe, *ChemSusChem* accepted. DOI: 10.1002/cssc.202102294.

In addition, the author has contributed to the following articles:

[4] T. Nishimoto, T. Shinagawa, **T. Naito**, K. Takanabe, *J. Catal.* **2020**, *391*, 435-445.

[5] T. Nishimoto, T. Shinagawa, **T. Naito**, K. Takanabe, *ChemSusChem* **2021**, *14*, 1554-1564.

Following patents are based on this thesis:

[6]   Method for water electrolysis at near-neutral pH and its system, K. Takanabe, T. Shinagawa, **T. Naito**, T. Nishimoto, Patent application number 2020-012202.
(Japanese patent, information is translated)

[7] Electrolysis cell and water electrolysis system, K. Takanabe, T. Shinagawa, **T. Naito**, T. Nishimoto, T. Ichihara, R. Kojima, Patent application number 2021-165732.
(Japanese patent, information is translated)

[8] Electrodes, water electrolysis cell, water electrolysis device, carbon dioxide reduction electrolysis cell, and carbon dioxide electrolysis device, K. Takanabe, T. Shinagawa, T. Nishimoto, **T. Naito**, T. Ichihara, R. Kojima, Patent application number 2021-195780.
(Japanese patent, information is translated)